Delft University of Technology

A Geomechanical Research on the Upper Delft Sandstone

Master Thesis Geo-Energy Engineering

Written by:
Gertjan Postema

Supervisors:
Auke Barnhoorn,
Phil Vardon,
Hemmo Abels,
Milad Naderloo

September 29, 2025

Preface

This report finalizes for me a great chapter in my life, the chapter of being a student. Almost seven years ago started this time for me. I have learned a great deal and developed myself through the numerous engaging and challenging courses at the university and in the field. This study has opened the doors for me to the world of engineering in the subsurface, a challenging and beautiful field of study.

I would not have thought to enjoy this project as much as I did. I would like to thank my supervisors Auke Barnhoorn, Hemmo Abels, Phil Vardon and Milad Naderloo for their insightful ideas and pleasant way of working together. This laboratory research would not have been possible without the help of all the lab technicians who I greatly thank. I would like to thank my roommates, friends and family for their support and motivation. In particular, I am thankful to my brother and father who were especially helpful in discussing ideas related to this project.

Summary

Geothermal energy is expected to play a major role in decarbonizing heat supply in the Netherlands. Knowing the geomechanical behavior of a reservoir and seal can be crucial when engineering in the subsurface[5]. That is why this thesis focuses on characterizing the geomechanical behavior of the upper Delft Sandstone. Due to limited prior research and known lithological heterogeneity, this study seeks to quantify the constitutive behavior of the upper Delft Sandstone Member. Another goal is to measure the static moduli of the upper Delft Sandstone Member and to try to predict these moduli in parts of the reservoir where no cores are available.

From 87 m of core from well DEL-GT-01, 39 suitable samples were tested. Petro-physical measurements and classification into sandstones and shales were followed by UCS (15 samples), triaxial (13 samples), and Brazilian Disc Tests (11 samples). These provided strength, yield stress, Young's modulus, Poisson's ratio, and tensile strength.

Results show weak correlations between porosity and strength, but stronger samples had higher Young's modulus and yielded later. Coarse, organic-rich sands were weaker, while P- and S-wave velocities correlated with strength parameters. Triaxial tests confirmed increasing yield point with confining pressure and lower friction angles in shales.

A linear model predicted static Young's modulus in parts of the reservoir where no cores have been taken from dynamic moduli with an average absolute error of 2.6 GPa. Uncertainty remains due to limited sample data and high reservoir heterogeneity (REV larger than sample scale). The results in this study were compared to a geomechanical research of the IJsselmonde formation, which is a very similar formation. The data was not found to be very comparable, due to slightly different formations and different test techniques. Nevertheless, this data was the most comparable data out there.

Answering the main research question is and will remain difficult, because one can never know the geomechanical behavior of the complete reservoir. This study however did make a good start. It is now known that the upper Delft Sandstone member is moderately weak to strong. A correlation within the sands was also found with the grain size, or the amount of organic grains. It is not certain which of the two had the greatest effect. The ranges of dynamic moduli are known and we know what we need to test if we want to reduce the uncertainty within certain correlations.

This study shows the importance of extensive geomechanical data collection since the geomechanical behavior is not that easily explained.

Contents

1 Introduction

The goal of the Dutch government is to decrease its greenhouse gas emissions with 49 % by 2030, and to reduce it with 95 % by 2050, compared to the 1990's levels [18]. In 2018 around 40 % of the Dutch energy usage was in the form of heating which resulted in around 40 % of the greenhouse gas emissions of the Netherlands. 20 % of the heat used in the Netherlands could be provided by geothermal energy according to Energie Beheer Nederland (EBN) [15]. That is why companies, universities and research institutes are looking increasingly at the possibilities of geothermal energy in the Netherlands [18].
The TU Delft campus geothermal project (GTD), has joint objectives of research and commercial sustainable thermal energy production on the campus of the TU Delft. As part of the project, from June to December 2023, two wells were drilled on the campus of the TU Delft, of which 86 meters of core was taken. 15 meters of this was cap rock, which is the Rodenrijs Claystone Member and 71 meters of this was the reservoir, consisting of the Delft Sandstone. [9]

Knowing the geomechanical behavior of a reservoir and seal can be crucial when engineering in the subsurface, to prevent for example well bore instability, induced seismicity, and to preserve reservoir integrity [5]. Injection of fluid in a porous reservoir will increase the pore pressure, cause a poroeleastic and/or a thermoelastic effect. These three effects all can lead to a change in stress, which could influence the influence mechanical behavior of geological features, like faults. The spatial and temporal contributions of these stress effects depend on the thermomechanical and geological properties of the reservoir rock [4]. Of these geological and thermomechanical properties, the elastic moduli: Young's modulus, Poisson's ratio and the bulk modulus are required to be properly assessed to be able to quantify stress changes in the subsurface [20].

The objective of this research therefore, is to i) quantify the geomechanical behavior of the upper Delft Sandstone member and ii) to see how heterogeneous the constitutive behavior of this formations is.

State of the art

Until now, not much is known on the geomechanical behavior of the Delft Sandstone. One other geomechanical study ([20]) was done, where they tested two samples on what they reported to be the Delft Sandstone, while it is reported in other sources as the IJsselmonde sandstone. Nevertheless, these are comparable formations. The authors found that the Young's Modulus was higher for the higher porosity (28%) sample compared to the lower porosity (25%) sample, which was not expected, since the general trend is that the Young's modulus decreases with higher porosities [13]. The authors also found that the sample with a lower porosity had a higher Poisson ratio than the one with a higher porosity. From this they concluded that other factors like microstructures and mineralogy must have a greater effect on the Young's modulus than the porosity. With these partially surprising results and the known lithological variablity, it seems appropriate to test more samples to evaluate these results. Due to of the lack of previous geomechanical research on the Delft Sandstone, and because of the increasing demand of geothermal energy in the West Netherlands Basin will this geomechanical research be done.

Research questions

The main research question of this study is the following:

For the purpose of geothermal energy extraction: what is the constitutive behavior and what are the static moduli of the upper Delft Sandstone?

Sub-questions:

1. What correlations exist between the petrophysical and geomechanical properties of the Upper Delft Sandstone Member?
2. Are there sedimentological features that contribute to the heterogeneity in the constitutive behavior of the upper Delft Sandstone Member and how?
3. To what extent can predictions of the static elastic moduli be made in the well logs?

Hypothesis

The strength of a sedimentary rock sample can be affected by multiple factors. Higher porosity means more void space and less possibilities for grains to interlock, creating a weaker bond. Consistent empirical relationships show that the unconfined compression strength (UCS) decreases exponentially with increasing porosity. Most studies suggest that the UCS of sandstone decreases with increasing grain size [19]. The grain size does not have an effect on the crack initiation threshold, which is more dependent on the constituent minerals, but on the crack propagation. The larger grain boundaries are believed to provide more flaws and thus possibilities for cracks to propagate and nucleate, degrading the strength of the material [8],
Increasing water content in the samples can decrease the strength of the samples. Water can have an effect on the intrinsic strength parameters on the samples, for example on the friction coefficient [14]. However, there is not such a clear relationship with porosity and the Poisson ratio. The Poisson ratio can increase, decrease, or stay equal; it depends a lot on the shape of the pores and on the Poisson ratio of the matrix itself [13]. Depending on the type of heterogeneities, the sample's strength can increase or decrease. For example of there is a soft organic lamination present, it is expected to weaken the sample. However, if there is a concentration of cement present, it might increase the strength.

Since the results from Vincent Soustelle et al. [20] from a two sample test on the Delft / IJsselmonde sandstone are a bit contradicting, it is expected that porosity might not be the main factor controlling the geomechanical behavior. Since the Delft Sandstone is such a heterogeneous system [3], it is expected that the constitutive behavior is also very heterogeneous.

Appoach

In order to answer the aforementioned research questions, unconfined compressive strength (USC) tests, triaxial tests and Brazilian Disc tests will be conducted on the samples. From the UCS tests the elastic moduli Young's modulus and Poisson's ratio will be attained. As well as the yield point and unconfined compression strength. The triaxial test will give the Young's modulus and yield point per stress step and also the peak stress for the last stress step. The Brazilian disc test will give the tensile strength of the samples. The data generated by the geomechanical tests will be linked and may be correlated to the other data available (well logs, p- and s- wave velocity, etc.). Before the samples are destructively tested, they will be scanned with a CT-scanner, they will also be scanned after the tests. If unexpected / interesting results come from the geomechanical tests, some thin sections might be taken to study the samples and their cracks at microscale.

Characterizing mechanical properties of rocks can be done in a static and dynamic way, both techniques will be applied. Measuring the wave velocities in the samples during compression gives insight in how the compression of the samples changes the mechanical properties of the rocks. Therefore, this will be done in the UCS and Triaxial tests. Many factors controlling the strength of a sedimentary rock also affect other physical properties like velocity, elastic moduli and porosity [5]. Since these are measurable with geophysical well logs, it is possible to find empirical relationships to relate the rock strength to these parameters. A second objective of this research is to try to link the rock strength to these parameters to potentially predict the geomechanical behavior of similar formations at other places where only well log data are available, thereby facilitating the development of geothermal projects where only well log data are available.

2 Materials & Methods

This chapter describes the methods and materials used in this research. The subchapter Materials, gives a small overview of the geology behind the Delft sandstone and the Rodenrijs claystone. After that the samples which are used in this study are discussed. Then in the subchapter Methods the laboratory setup which was used will also be discussed.

2.1 Materials

2.1.1 Geological setting

The target formation for the TU Delft campus geothermal project is primarily the Delft sandstone member, and secondary the Alblasserdam Member. The cap rock is the Rodenrijs claystone Member. These members are part of the Nieuwekerk formation, the Nieuwekerk formation has been deposited in the West Netherlands Basin. A schematic cross-section, together with the well trajectories are shown in Figure 1. The samples which are used in this study come from the cores taken in the the producing well, the red colored trajectory in Figure 1.

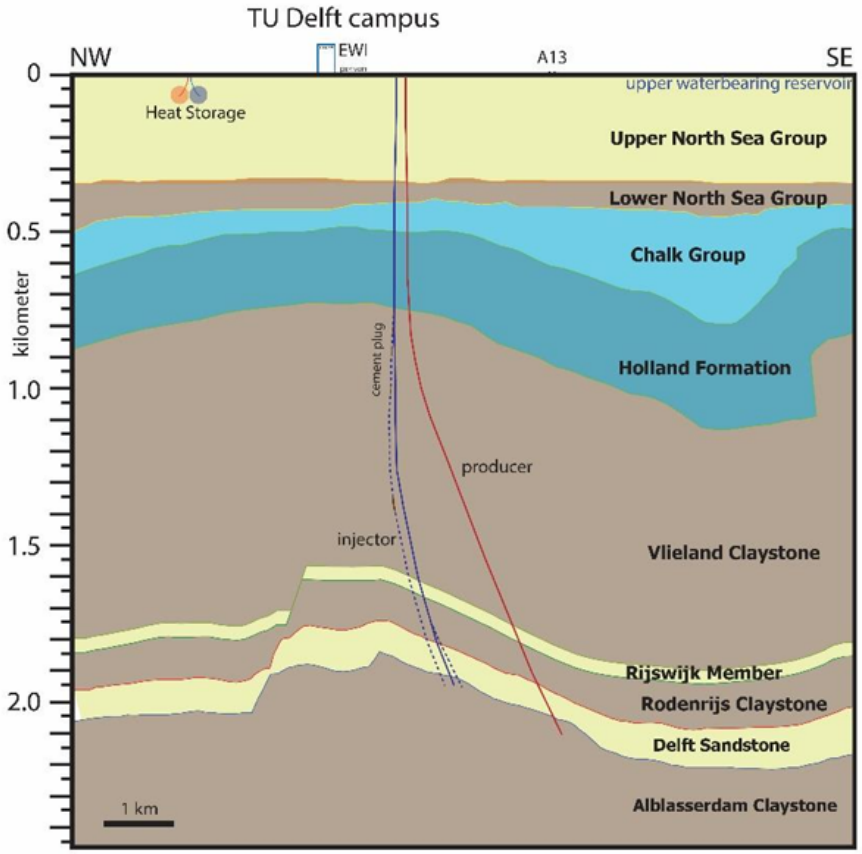

Figure 1: A schematic overview of the subsurface below Delft. The samples used in this research come from the producing well, indicated by the red line. [9]

West Netherlands Basin

The West Netherlands Basin (WNB) formed during several rift phases from the Kimmeridgian in the late Jurassic (157 Ma) to the Barremian in the lower Cretaceous (131 Ma) [24]. The basin opened up in several series of NW - SE rifts. While these rifts were formed, they were filled with fluvial sediments. In Hauterivian times, the rifting stopped and subsidence started to take place which made transgression possible, thereby overlaying the fluvial sediments with shallow marine sediments [7].

The Rodenrijs claystone, Delft Sandstone and the Alblasserdam formation are deposited during the late Jurassic to the early Cretaceous. Together they form the Nieuwekerk formation. This study focuses on the Delft Sandstone Member since the samples that are available are from this formation.

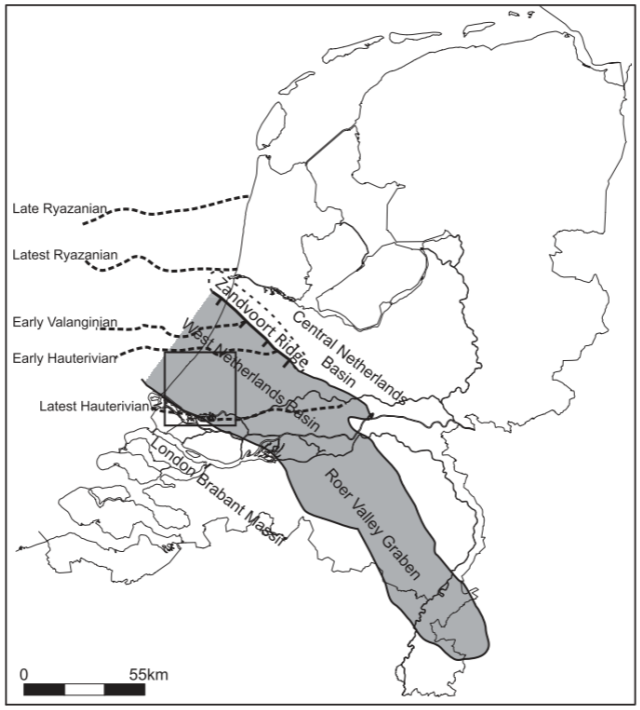

Figure 2: Geological setting of the WNB during the cretaceous. [24]

Delft Sandstone

The Delft sandstone member conformably overlies the Alblasserdam Member. The Delft Sandstone Member was characterized as deposits from a fluvial-deltaic system in an upper to lower delta plain. The Delft Sandstone Member is stated to consist of: "fluvial to distributary channel deposits, crevasse splay to levee deposits, overbank fine deposits, and paleosols" [3]. Since the Delft Sandstone is characterized as a heterogeneous system with different types of deposits, it is expected that the geomechanical behavior is also quite heterogeneous.

2.1.2 The Samples

88 meters of core has been taken from the producing well, named: DEL-GT-01. Due to technical difficulties, this was not a continuous section. In the upper Delft sandstone were the following intervals cored:

1. 2576 m - 2591 m: 15.5 m
2. 2594 m - 2651 m: 57 m

From every other section of core, two samples are taken, one at the top and one at the bottom. This made it possible to keep every other core closed. After the samples were taken, they dried for several months before this research started. Before any destructive research started was the following measured on the samples:

1. Dimensions and weight
2. Porosity
3. P- and S-wave velocity
4. Thermal properties
5. Sedimentological description

Because of the differences in samples, the samples were categorized based on gamma ray and porosity to make sure for each test there was a similar variety of samples. Figure 4 shows four pictures of a sample of each category. The samples were divided in different categories based on their gamma ray. 4 categories were made:

1. Cat. 1: low gamma ray: sand
2. Cat. 2: Slow increase in base line of gamma ray, still sand
3. Cat. 3: More shaley sandstones
4. Cat. 4: High gamma rays, shales, both Rodenrijs and Delft Sandstone

The samples were also categorized based on their sedimentological features. The grain size of each sample was checked, this ranged from silt/clay to medium lower sandstone. the amount of organic material was visually inspected and subdivided between no organic material, some organic material and substantially more organic material. With organic matter, pieces of lignite are meant, not the small organic grains within the samples. That will be later discussed. A good example of a piece of lignite is visable in Figure 4a. The samples were also checked if they had lamintaions or not.

The samples were then grouped, the first group was based on grain size:

1. group 1: silt/clay
2. group 2: very fine lower, very fine upper, fine lower, fine upper
3. group 3: medium lower and courser

The first sub-group is based on the amount of organic material:

1. sub-group A: no organics
2. sub-group B: some organics
3. sub-group C: more organics

The second sub-group is based on laminations:

1. 1: no laminations
2. 2: laminations.

This gave each samples a code, for example, a medium lower sandstone with some organic material and laminations would be: 3A2

In the rest of this report, group 1 will be referred to as shales and groups 2 and 3 as sands.

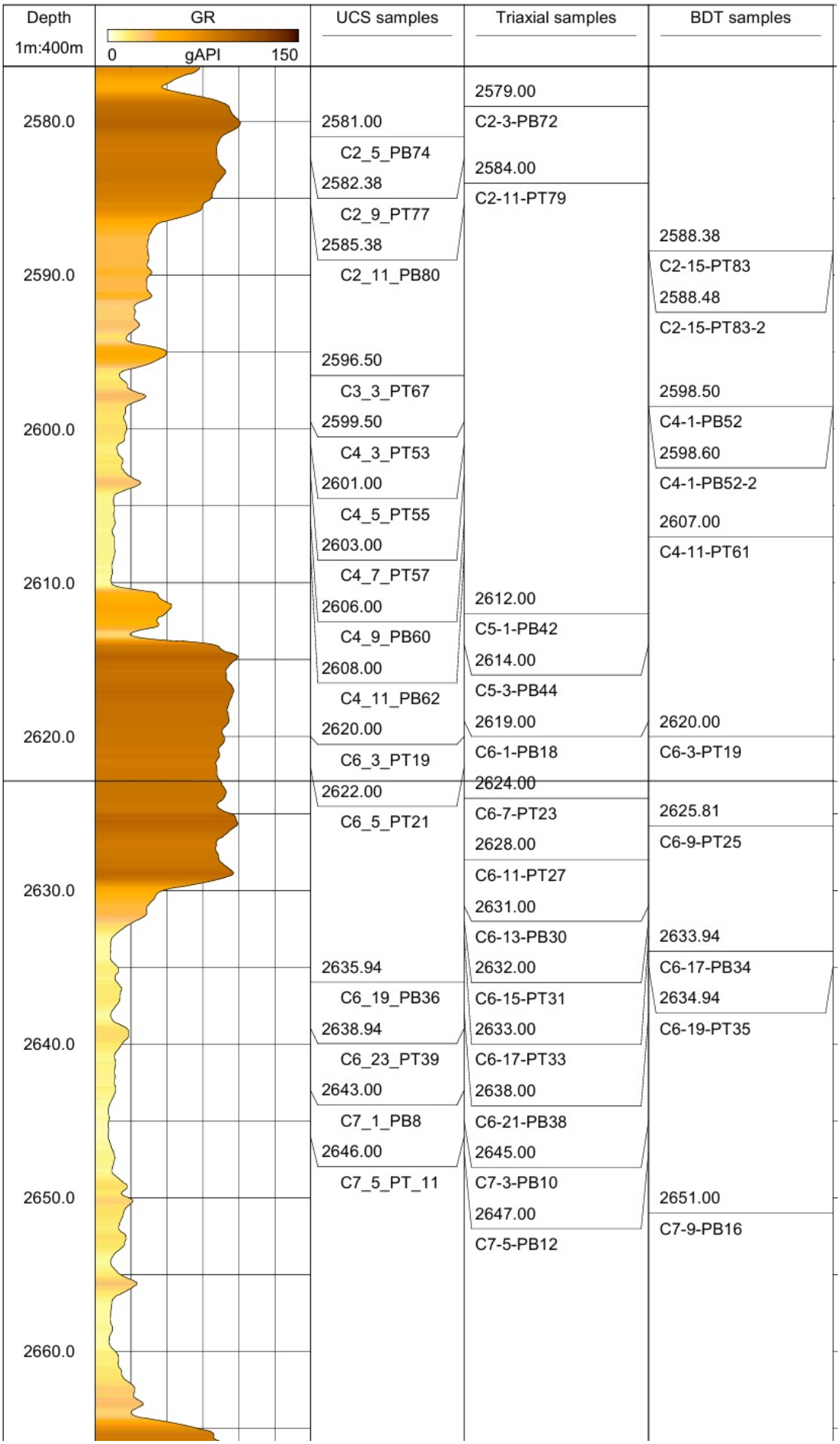

Figure 3: Gamma ray log of the DEL-GT-01, with the samples which were tested on each test.

(a) Sample $C7 - 5 - PT11$, an example of a category 1 sample

(b) Sample $C3 - 3 - PT67$, an example of a category 2 sample

(c) Sample $C6 - 17 - PT33$, an example of a category 3 sample

(d) Sample $C2 - 5 - PB74$, an example of a category 4 sample

Figure 4: Examples of samples from each category.

Samples for UCS test

For both the UCS and the Traxial tests, samples were needed that had a minimum length of twice their diameter. Since these samples were limited, a careful division was made to see which sample would be tested on which test.

Since it was assumed that the gamma ray, porosity and sedimentological heterogeneities had a great influence on the strength of the sample, the division was made based on these variables. The strategy was for each test to have a similar set of samples. Thus a couple of heterogeneous samples and a couple of homogeneous samples.

The first UCS tests were performed on category 1 and 4 samples. Half of the long samples of category 1 and 4 were assigned to the UCS test, the other half to the triaxial test.

The samples of category 2 were also tested on the UCS test, this category was not divided between the UCS and Triaxial test because there were not enough samples.

The samples that were tested on the UCS test with their properties are shown in the appendix in Table 5.

Samples for triaxial test

The long enough samples of category 1 and 4 which were not tested on the UCS test, were tested on the triaxial test. Also the samples of category 3 were tested on this way, these samples were not divided between the two tests because there wouldn't have been enough for each test to generate a good amount of data from which conclusions could have been drawn. The sand samples were saturated in brine for at least 8 hours at -1 bar. One shale sample was saturated to see how it would react to the brine. It deteriorated quickly, and fell apart when it was taken out. Therefore, it was chosen to not saturate the shale samples.

The samples that were tested on the triaxial test with their properties are shown in the appendix in Table 6.

Samples for Brazilian Disc test

There were quite some samples in the set of cores present which were not suitable to test in the UCS or triaxial test, because they were too short. These samples were tested on the Brazilian disc test. Again, the sandstones were saturated with brine, the shales were left unsaturated to preserve their integrity.

A table with the samples tested on the BDT is present in the appendix in Table 7

Sample preparation

In order to complete a correct UCS or triaxial test, the top and bottom of the samples must be parallel. The samples which were not parallel were sanded down such that they were.
Also to have a complete top and bottom surface of the samples, some samples of which a little piece has broken, were fixed with gypsum, such that the stress could be evenly exerted on the sample. Figure 5 shows an example of a sample that was fixed with gypsum. In the tables 5 and 6 "Gypsum" means that this sample had been fixed with gypsum prior to testing.

The sand samples which were tested on the triaxial test and the Brazilian disc test were saturated, the other samples were tested dry.

Figure 5: An example of a sample that has been repaired with gypsum in order to create two even surfaces on which pressure can be applied during the tests.

2.2 Methods

2.2.1 UCS test

To determine the unconfined compression strength (UCS) of a rock, a uniaxial compression test can be performed. A uniaxial compression test measures the uniaxial strength of a rock, thus without confining pressure ($\sigma_2 = \sigma_3 = 0, \sigma_1 > 0$). The samples will be pressed together by two parallel plates. There is a chain sensor around the sample that measures the radial strain, and there are two linear variable differential transistors (LVDT) that measure the axial strain, see figure 6. This will be done while actively measuring the acoustics in the sample which are also visible in the figure. A detailed explanation on the active acoustics will be given in chapter 2.2.5. The UCS tests will be done on unsaturated samples.

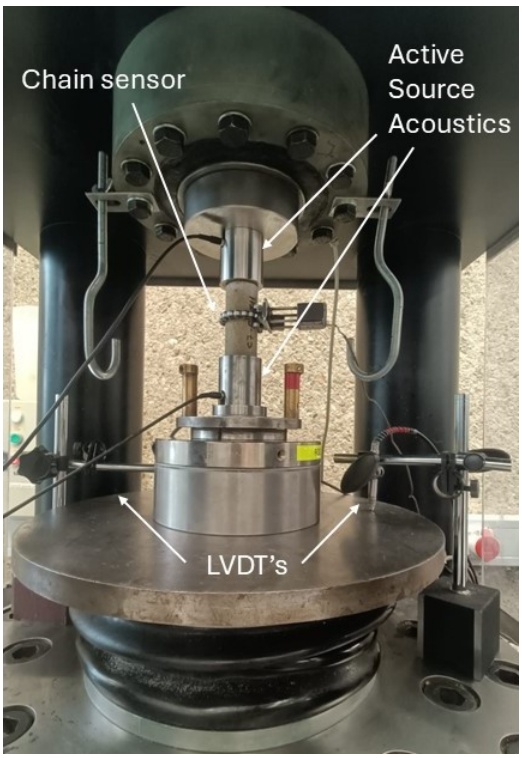

Figure 6: The set up of a UCS test.

The axial strain of the sample is the relative axial deformation, given by the following formula:

$$\varepsilon = \frac{\Delta L}{L} = \frac{L - L_{\text{new}}}{L}[-] \tag{1}$$

For the axial strain L is the initial length of the sample, Lnew being the length of the sample while it is being compressed. This will be measured by two LVDT's, see Figure 6. The radial strain is the relative radial deformation, given by the following formula:

$$\varepsilon = \frac{\Delta r}{r} = \frac{r - r_{\text{new}}}{r}[-] \tag{2}$$

In this case r is the original radius of the sample and r_{new} is the radius during compression, which is measuring using the chain sensor, indicated in Figure 6.

In Figure 7 an example is shown of the results of a UCS test. The axial stress is plotted on the y axis, the axial strain is plotted on the positive x axis, the radial strain is plotted on the negative x axis. In the linear elastic part of the axial stress strain curve is the Young's modulus calculated as shown in the figure.

$$E = \frac{\sigma}{\epsilon}[Pa]. \tag{3}$$

[10]

The Poisson ratio (Equation 4) is ideally calculated in the same interval as the Young's modulus, however when the radial stress strain curve in this interval investigated it often is the case that there is no linearity. That is why usually the Poisson ratio is calculated using the radial and axial strain is a lower interval, like shown in Figure 7.

$$\nu = -\frac{\epsilon_r}{\epsilon_{axial}}[-] \tag{4}$$

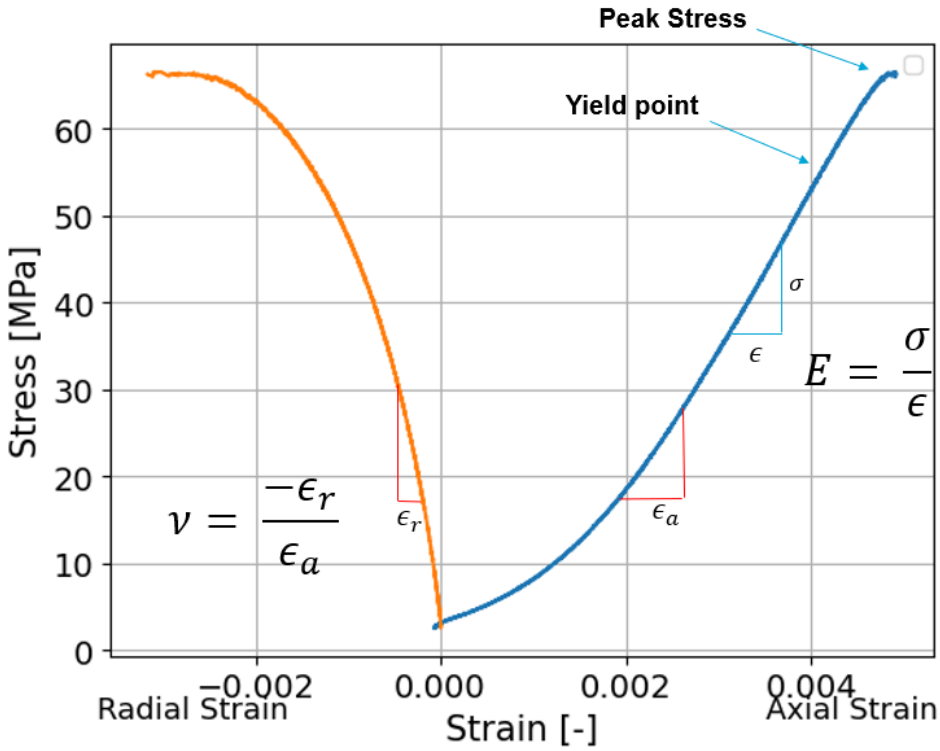

Figure 7: Example of UCS test results, including the formula's for the Young's modulus and POisson ratio.

The next figure shows how for each sample the yield point was measured. The axial stress was plotted versus time in blue, the derivative of stress with respect to strain was plotted in red. When the sample behaves linearly, the derivative should give a constant value, which can be seen in Figure 8. Once the derivative is not constant anymore, the behavior is not linear anymore, which means the sample has yielded, this is called the yield point.

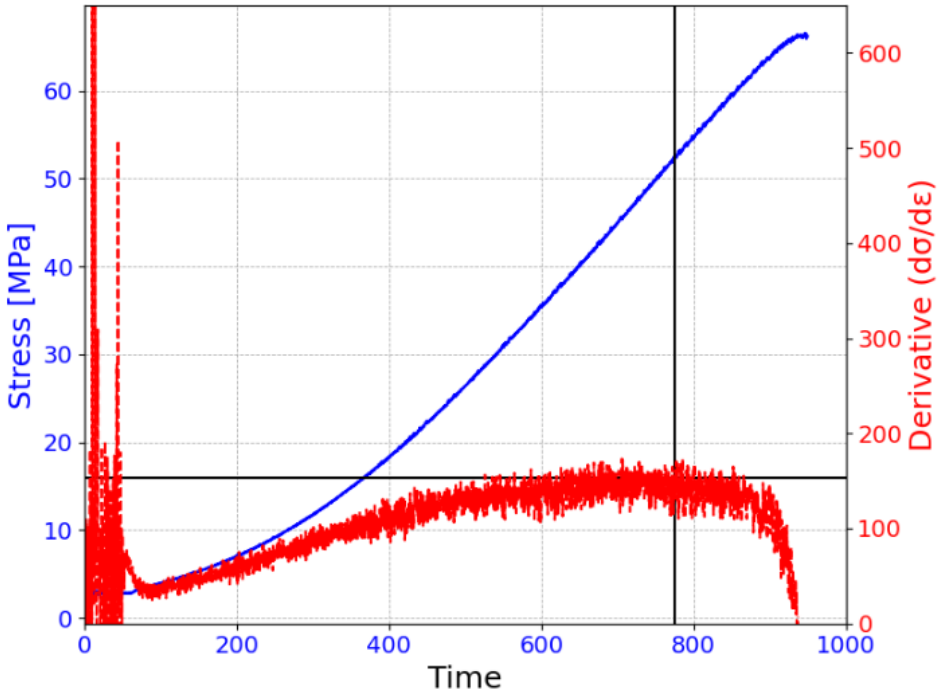

Figure 8: Time plotted versus stress in blue, stress/strain derivative plotted in red. When the derivative is not constant anymore, the sample starts to yield.

All the data presented in this report which comes from the UCS tests has been correct for the strain generated by the machine itself. 2.2.4 explains how this is done.

2.2.2 Triaxial test

A widely used rock mechanical test is the triaxial compression test. Unlike the name suggests, the test uses 2 equal stresses and one larger stress. ($\sigma_1 > \sigma_2 = \sigma_3 > 0$). This is because in this test cylindrical samples are used in which one cannot distinguish between σ_2 and σ_3. The vertical σ_1 is applied in the same way as the USC test. The sample will be surrounded by a tight impermeable sleeve, on the outside of the sleeve will be a pressurized fluid. σ_2 and σ_3 are here referred to as the confining stress, and σ_1 is referred to as the axial stress. [10] These tests will be done in drained conditions. During the test, active acoustics will also be measured.

From this test the Young's modulus can be calculated, in the same manner as for the UCS test. However, the Poisson's ratio cannot be calculated because the radial strain cannot be measured due to the sleeve around the sample. The yield point will also be calculated in the same manner as for the UCS test.

This test represents the stress conditions in the subsurface better than the USC test, since in the subsurface are also confining pressures present. However, σ_2 and σ_3 in the subsurface will likely not be equal.

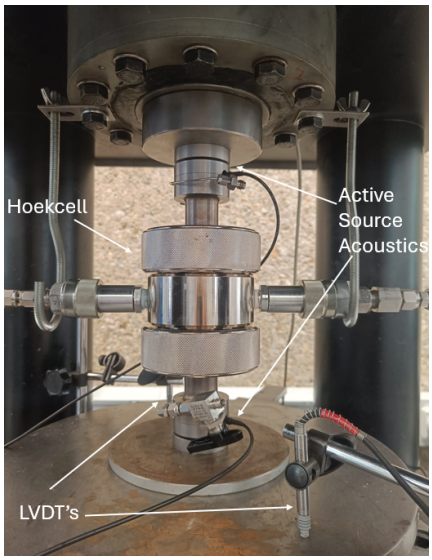

Figure 9: The set up of a triaxial test, the samples is present inside the Hoekcell.

The operation procedure for the sample is as follows:
The sample is placed in the Hoekcell with a confining pressure of 0.5 Mpa to hold the sample in place. The Hoekcell is placed in the press. While the confining pressure is increased to 5 Mpa gradually, the axial pressure is increased gradually as well. That is to prevent the acoustic piston to be pushed out by the sleeve which applies the confining pressure.
When the correct confining and axial pressure is reached, the first experiment starts. The axial pressure increases under a strain controlled mechanism, where the strain is $0.0005 mm/s$, while the confining pressure is constant. When the sample starts to yield, the test is stopped and the axial pressure is decreased to the current confining pressure plus 1 Mpa. Again, to prevent the confining pressure sleeve to push out the pistons. This process is repeated for 4 or 5 different confining pressures (5, 10, 20, 30, 40 Mpa). At the highest confining pressure, the test is run until after the yield point, until it breaks completely. 1 shows which sample was tested at which confining pressures, and if the samples were tested saturated or not. Table 1 shows which sample has been tested on which confining pressures and if the samples were saturated or not.

All the data presented in this report which comes from the triaxial tests has been correct for the strain generated by the machine itself, 2.2.4 explains how this is done.

Table 1: This table shows which sample was tested under which confining pressure. 'x' meaning it was tested at this confining pressure, '-' meaning it was not tested. It also says if the sample was saturated prior to testing.

ID	$\sigma_3 = 0.5$	$\sigma_3 = 5$	$\sigma_3 = 10$	$\sigma_3 = 20$	$\sigma_3 = 30$	$\sigma_3 = 40$	saturated?
C6-15-PT31	-	x	x	x	x	x	yes
C6-7-PT23	-	x	x	x	x	x	no
C7-3-PB10	-	x	x	x	x	-	yes
C7-5-PB12	-	x	x	x	x	-	yes
C2-11-PT79	-	x	x	x	x	-	no
C6-1-PB18	-	x	x	x	x	-	no
C5-3-PB44	-	x	x	x	x	-	yes
C6-17-PT33	-	x	x	x	x	-	yes
C6-13-PB30	-	x	x	x	x	-	yes
C6-21-PB38	-	x	-	-	-	-	yes
C2-3-PB72	-	x	-	-	-	-	no
C5-1-PB42	x	-	-	-	-	-	yes
C6-11-PT27	x	-	-	-	-	-	no

2.2.3 Brazilian Disc Test

In the Brazilian disc test, a 15 mm thick cilindrical sample is loaded with a uniform pressure. This pressure is radially applied at the top and bottom on a short strip of the specimen if seen from the side, until failure. A displacement control of 0.0005 mm/s was used. The sample is assumed to fail according to the Griffith criterion [11]. There are several assumptions to be made before determining the tensile strength from the Brazilian disc test. The rock should be regarded homogeneous, isotropic and linearly elastic before failure occurs according to [17]. The rock should split along the compressive strength, which is vertical in this case. Else the rock is exhibiting an invalid failure mode according to the International Society for Rock Mechanics [6].

Figure 10: Caption

The data from the Brazzilian disc test includes two measurements from two LVDT's, which measure the amount with which the sample is compressed. Also the Load is measured in kN. The International Society for Rock Mechanics suggests the following method to calculate the tensile strength from the load with formula 5. In which P is the load in kilo Newton, D is the diameter in meter, and t is the thickness in meter.

$$\sigma_t = \frac{2P}{\pi D t} \tag{5}$$

2.2.4 Machine strain correction

When doing the UCS test and the triaxial test, the LVDT's are placed on the metal plate shown in Figure 6. This means that the LVDT's measure the strain of the samples, but also of the metal parts in between, including the active sources acoustics. These parts also deform a little when pressure is applied. To get the strain of only the sample, a "machine strain correction" is done. For this a normal UCS/Triaxial test is performed using an aluminum sample of which the Young's modulus is known.

The strain of the aluminum sample can be calculated from the stress data and the known Young's modulus as follows:

$$\epsilon_{aluminium} = \frac{\sigma}{E_{aluminium}} \tag{6}$$

The following equation gives the strain of the machine itself:

$$\epsilon_{machine} = \epsilon_{total} - \epsilon_{aluminium} \tag{7}$$

Then using linear regression to the stress strain curve of only the machine, the Young's modulus of the machine is calculated.

Then the strain of a rock sample which is tested will be corrected for the machine strain as follows:

$$\epsilon_{sample} = \epsilon_{total} - \frac{\sigma}{E_{machine}} \tag{8}$$

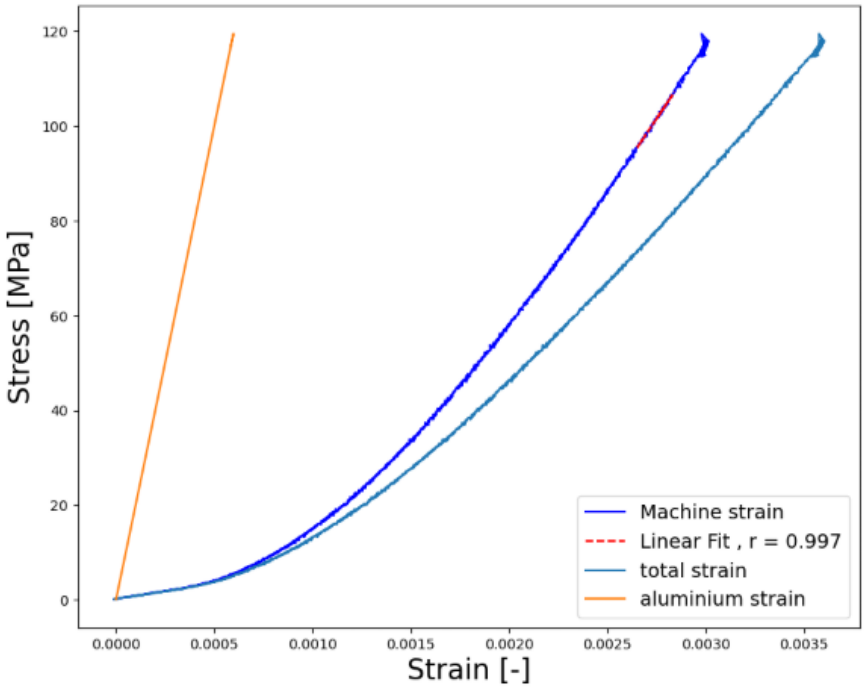

Figure 11: The light blue line is the measured total stress/strain curve. The orange line is the theoretically calculated line of the aluminum sample. The dark blue line is that of the machine, calculated by equation 7. The red dotted line is the linear fit to get the Young's modulus of the machine.

This test was done twice on the same aluminum sample. Two slightly different Young's moduli were attained. 62.500 GPa and 63.600 GPa, the average will be used to correct the samples which are tested. This strain correction was done both for the UCS test as well as the triaxial test since a different test set up was used. Note that all the data presented in this report has been corrected for the strain.

2.2.5 Active Acoustics

Active acoustics was applied during the UCS and triaxial tessts. Active acoustics refers to the technique to shoot every ten seconds, a P- and S-wave are through the sample, and record their arrival times. Figure 6 shows the UCS set up. Inside the two metal parts which are indicated by "Active Source Acoustics" are the acoustics transmitter and receiver.

The wave generator generated the wave which was amplified by the amplifier. The receiver received the signal after which it was sent to the oscilloscope. A computer is connected to the oscilloscope which saves the data.

The transmitter transmits a S-wave, and as a by-product a small P-wave is generated. Since the P-wave is faster, it is possible to pick that arrival time before the larger S-wave comes in. Both P- and S-wave travel through the metal part holding the sample before it travels through the sample, therefore when analysing the data, the travel time of these metal parts was subtracted. Figure 12 shows an example of the arrival of a P- and S-wave on a dummy sample.

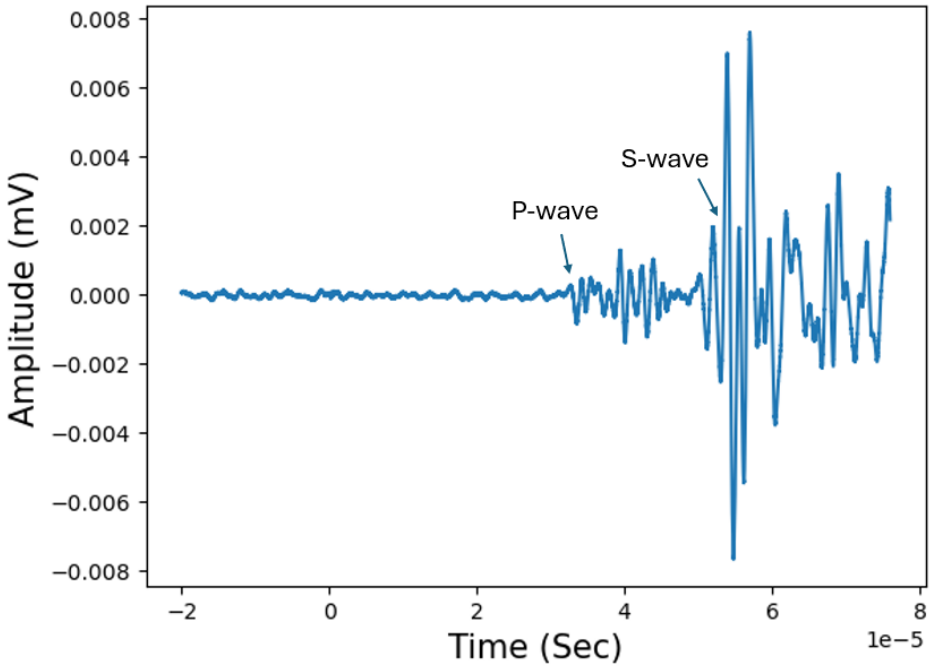

Figure 12: This figure shows the example of the generated data by the active acoustics. Every ten seconds, such a signal is sent through the sample, thus every ten seconds the P- and S-wave arrival times can be picked.

3 Results

This chapter will present and describe the results of the mechanical and acoustic tests in the Lab. First the results of the UCS test will be presented, then the traixial tests, then the Brazilian disc test and at last the acoustic tests.

3.1 UCS tests

The fifteen samples tested on the UCS test were from category one, three and four. The data parameters that are generated by the UCS test are shown in Table 2

Table 2: Results from the triaxial tests. "E" stands for the Young's modulus. "Yield point" is at 0.5 MPa confining pressure. "UCS" is the unconfined compressive strength.

ID	UCS [MPa]	Yield point [MPa]	E [GPa]	ν [-]
C2-5-PB74	32.35	24.09	12.51	0.05
C6-5-PT21	28.44	14.57	10.64	0.40
C6-19-PB36	66.53	55.59	17.01	0.41
C6-23-PT39	13.58	12.10	3.43	0.03
C7-5-PT11	32.58	23.99	9.22	0.11
C7-1-PB8	31.10	24.42	6.18	0.38
C6-3-PT19	64.92	46.39	20.05	0.05
C2-11-PB80	19.25	12.86	6.68	0.11
C2-9-PT77	56.38	45.87	18.49	0.09
C3-3-PT67	35.07	24.44	11.10	0.11
C4-3-PT53	65.56	51.04	20.13	0.16
C4-5-PT55	8.23	7.99	3.79	0.03
C4-7-PT57	33.39	23.60	10.85	0.09
C4-9-PB60	39.73	33.99	12.81	0.17
C4-11-PB62	57.32	45.71	18.57	0.10

Figure 13 shows the stress/strain plots for each sample tested in the UCS test. They are colored by their different categories, black being category four, the shales, orange is category one, the sands and brown is category two, sand with increasing gamma ray. At first, it was expected that the origins of these different categories would influence the peak strengths of the samples, but as one can see in Figure 13, this is not the case. From each category, there are samples which have both high and low peak strengths. That is why from now on, the samples will not be presented by their categories anymore, but mostly by their petrophysical data.

One can note here that in terms of the peak strength, the samples seem to group. There is a group of 5 samples that have a high peak strength, greater than 55 MPa. There is a medium group, which is between 30 and 40 MPa, and a group with a low peak strength, lower than 20 MPa.

An interesting fact is that there are no samples which have a peak strength in between these three different groups, in other words, the peak strengths seem to cluster together.

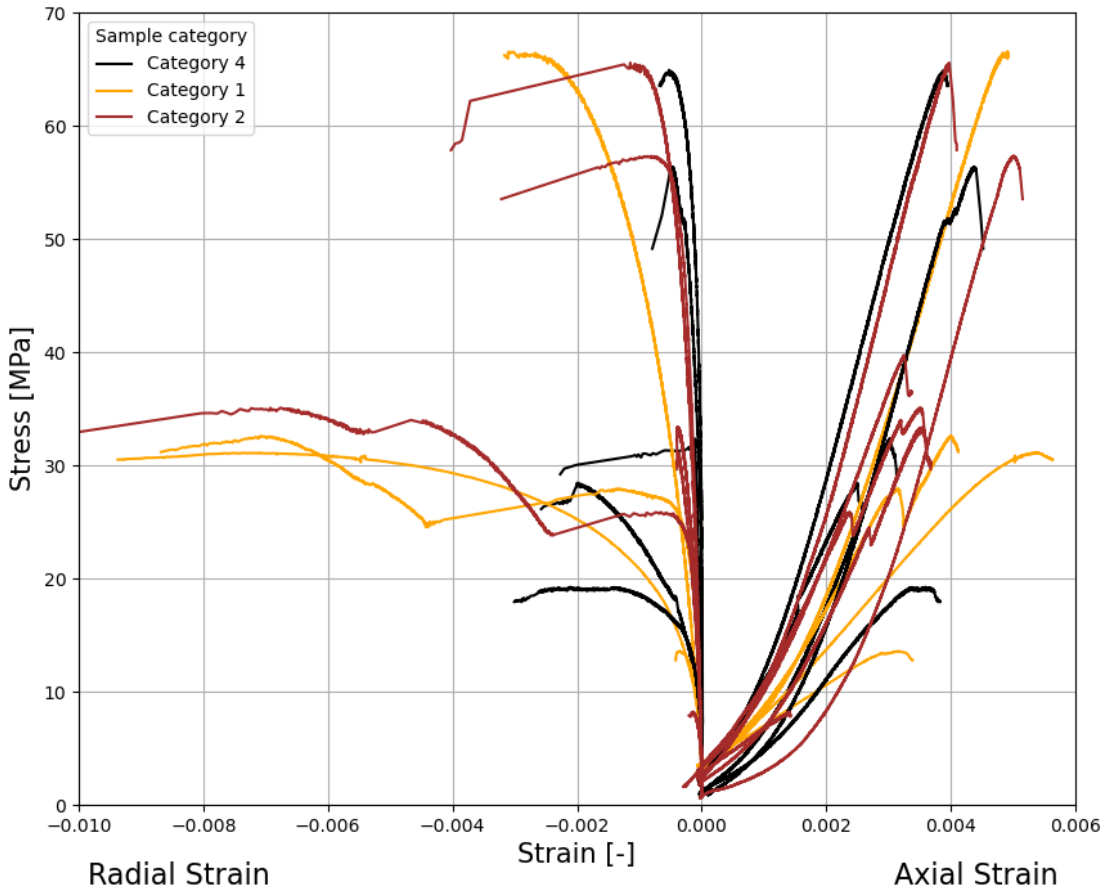

Figure 13: Stress / strain plots for all samples tested on the UCS test. The positive x axis shows the axial strain, the negative x asix shows the radial strain of the sample. Colored by its category.

From the data of the UCS tests the Poisson ratios, the Young's moduli and the yield points were calculated.

Figure 14 shows the peak stress (or UCS), Young's modulus, Poisson ratio and yield stress plotted versus the porosity and colored by the gamma ray. It is important to note that all the samples with a gamma ray value higher than 50 (shales) are colored the same, (deep purple). While the other samples are colored by their gamma ray according to the color bar on the right hand side of each figure.
One can note in the peak stress plot that the the shale samples have a peak strength between 20 and 70 MPa, which is comparable to the peak stress of the sands, which is between 8 and 70 MPa. The Young's modulus for the sands ranges from 3 to 20 GPa for the sands. For the shales it ranges from 6 to 20 MPa. The yield stress ranges in the sands between 8 and 60 MPa. The yield stress of the shales has a slightly lower range, between 10 and 50 MPa.

The two samples with the lowest UCS, appointed by the arrows in Figure 14a) did show some particularities which might explain their low UCS, yield stress and Young's modulus. Sample PT39 did not break completely through the middle as in the other samples. This is shown in the cross sections of the CT-scans of Figure 15. A correct test should break the sample through the middle; here only a side of the sample is broken off. This could have happened because the top and bottom surfaces of the samples maybe weren't parallel; however, it is not exactly certain why this happened and if the test really should be classified as an unsuccessful experiment. PT55 was a relatively short sample (56.5 mm), this could cause the sample to break earlier since the forces exerted on the sample do not have enough space. The International Society for Rock Mechanics recommends a length/diameter ratio of 2.5 to 3, which in this case was 1.9. A lower length/diameter ratio is expected to decrease the UCS [23].

What is apparent is that the Poisson ratios seem to group. The majority of the samples have a Poisson ratio between 0.03 and 0.2, while there is a group of 3 which have a Poisson ratio of around 0.4. This is because these samples exhibited a great amount of radial strain. These three samples did not visually show any particularities.

Unfortunately, with this number of samples, no real trend can be seen in any of these plots. One could say that if more samples are tested, a trend could become visible with porosity and the strength parameters. However, with this number of samples, that is not yet the case.

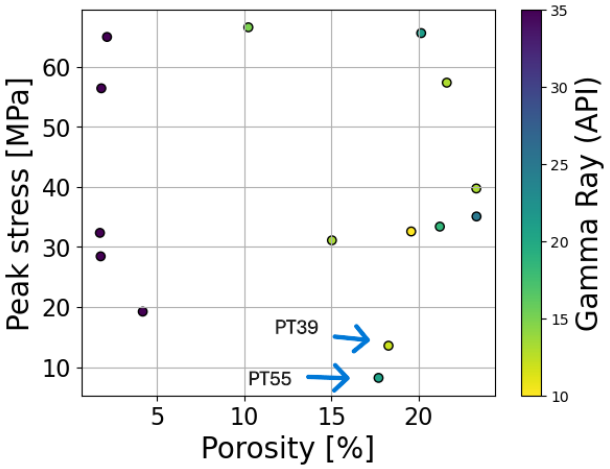

(a) Peak stress vs porosity colored by gamma ray.

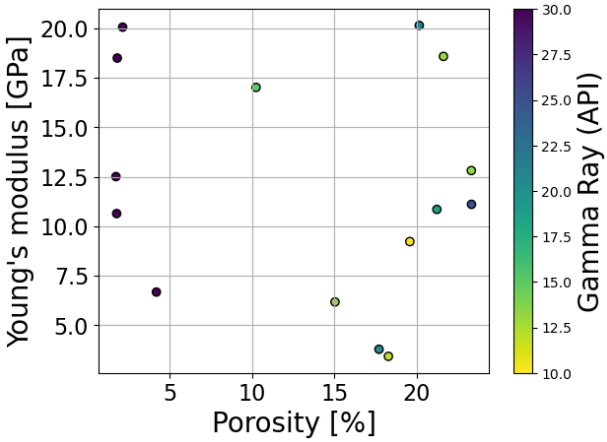

(b) Young's modulus vs porosity colored by gamma ray.

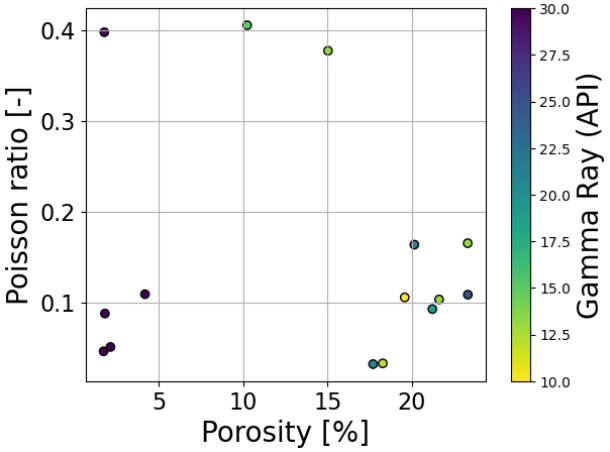

(c) Poisson ratio vs porosity colored by gamma ray

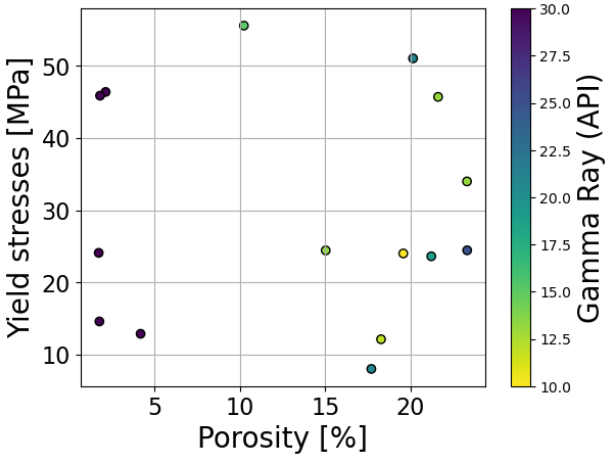

(d) Yield stress vs porosity colored by gamma ray

Figure 14: The peak stress, Young's modulus, Poisson ratio and yield stress plotted versus the porosity and colored by gamma ray. It is important to note that all the samples with a gamma ray value higher than 50 (shales) are colored the same, (deep purple). While the other samples are colored by their gamma ray according to the color bar on the right hand side of each figure.

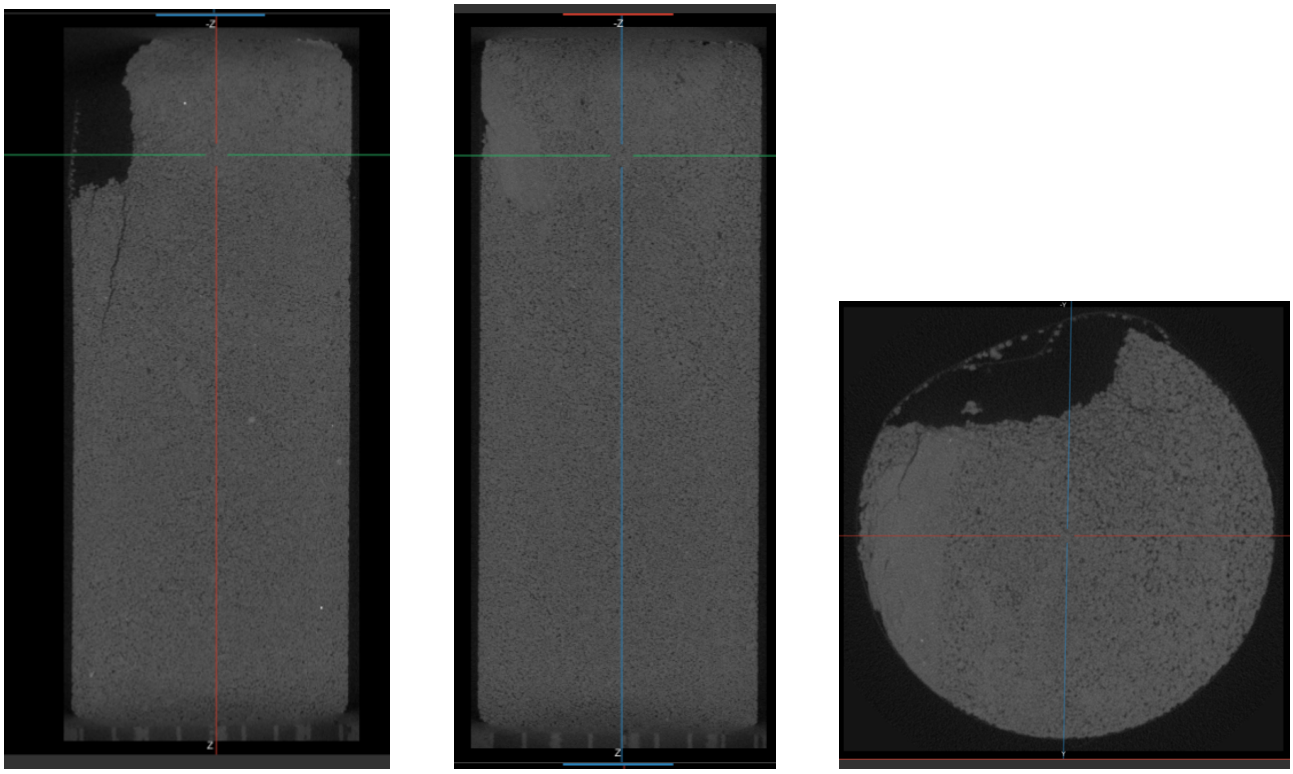

(a) vertical cross section 1 (b) vertical cross section 2 (c) horizontal cross section

Figure 15: Sample C6-23-PT39 After the UCS test.

One interesting sample to note is sample C6-19-PB36. (Note that the samples do not have the same orientation in the picture as in the scan.) In Figure 16a, a photo of the sample before the ucs tests is shown. One can clearly see black (which is expected to be organic) laminations. These laminations are not visible on the CT-scan (see Figure 16b). There one can see laminations, yet these are not the same. The laminations on the scan show a lighter color, meaning a heavier material, this is probably siderite. If organic laminations would be present in the sc scan, they would show up as dark colored. It is interesting to note that the sample did not break through the laminations, indicating that these laminations are not the weakest point.

(a) C6-19-PB36 Before

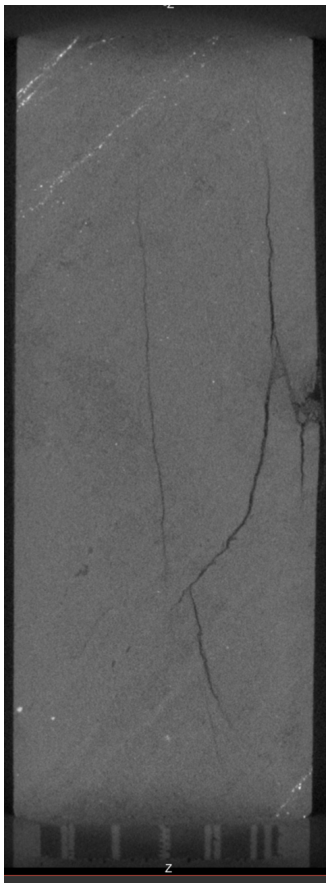

(b) Sample C6-19-PB36 After the UCS test.

Figure 16: Sample C6-19-PB36 shown in a picture (a) and as a CT-scan (b). Note that the orientation of the sample is not equal in figures

Figure 17 shows the yield stress, peak strength, and Young's modulus plotted versus each other. A nice trend with all three parameters can be seen. Which makes sense, a stiff rock is expected to have a higher peak strength and yield stress.

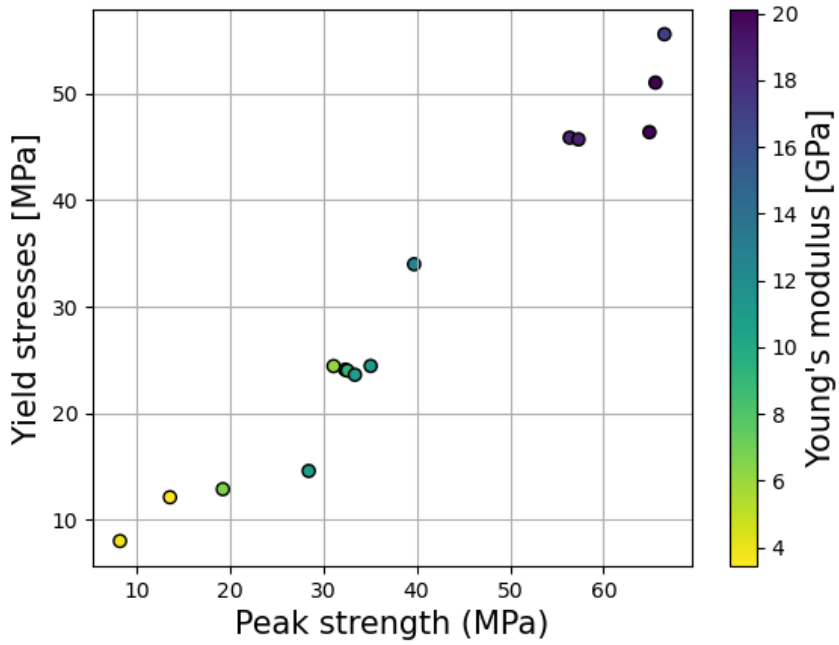

Figure 17: peak strength versus Yield stress colored by Young's modulus. One can see and upward trend within all three variables, which is as expected.

Figure 18 shows the peak strength, Young's modulus, Poisson ratio and yield stress plotted versus the P-wave velocity, colored by the gamma ray. It is important to note that all the samples with a gamma ray value higher than 50 (shales) are colored the same, (deep purple). While the other samples are colored by their gamma ray according to the color bar on the right hand side of each figure.
Within the low gamma ray values, which are light colored in this case, one can see a slight upward trend with the P-wave velocity and the Peak stress, Young's modulus and yield stress. This trend is indicated by the green arrow. Looking only at the high gamma ray samples, which are dark colored here, no real trend is visible in any of the four plots.

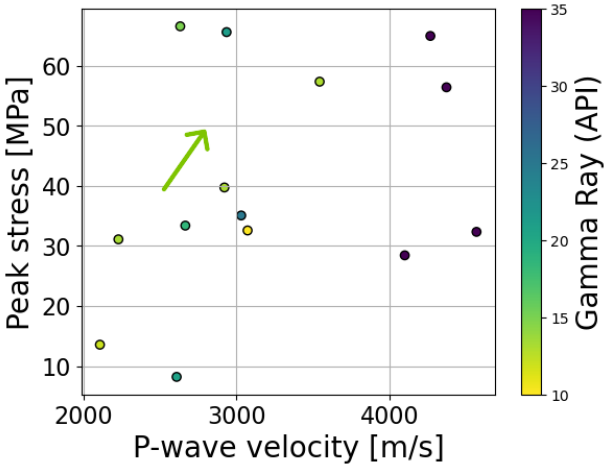

(a) Peak stress versus P-wave velocity colored by gamma ray.

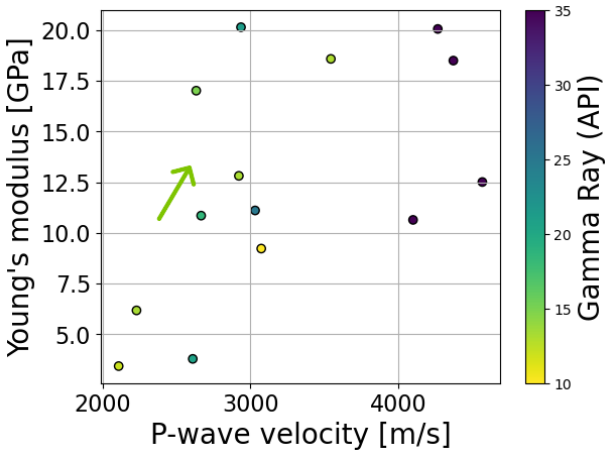

(b) Young's modulus versus P-wave velocity colored by gamma ray.

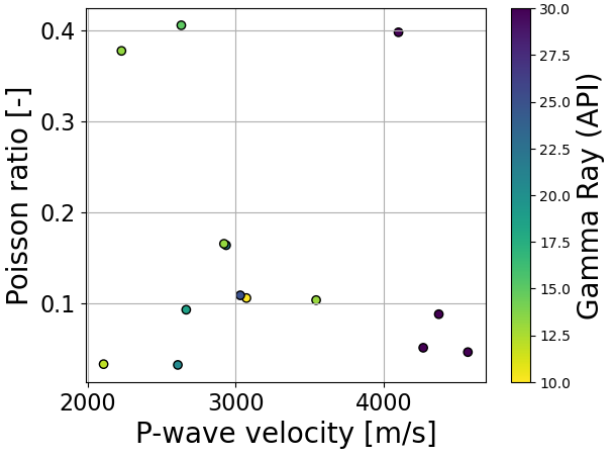

(c) Poisson ratio versus P-wave velocity colored by gamma ray.

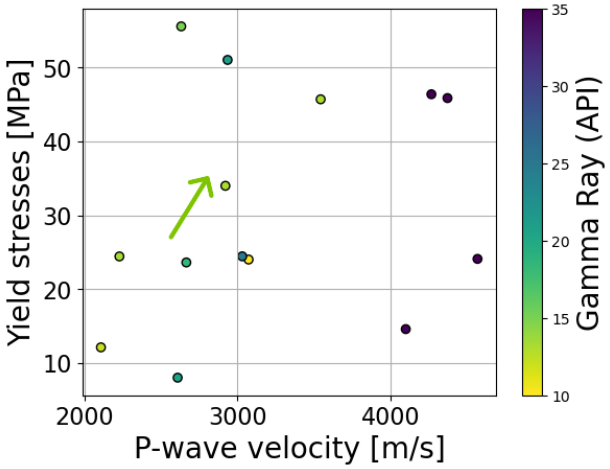

(d) Yield stress versus P-wave velocity colored by gamma ray.

Figure 18: These figures show the peak stress, Young's modulus, Poisson ratio and yield stress plotted versus the P-wave velocity, colored by the gamma ray.

Figure 19 shows the same plot as Figure 18 except that this one is plotted versus the s-wave velocity. One can see, except for the Poisson ratio, again a correlation within the sand samples, not within the shales. This is expected since there is a good correlation between the P-wave and S-wave velocities, see Figure 20.

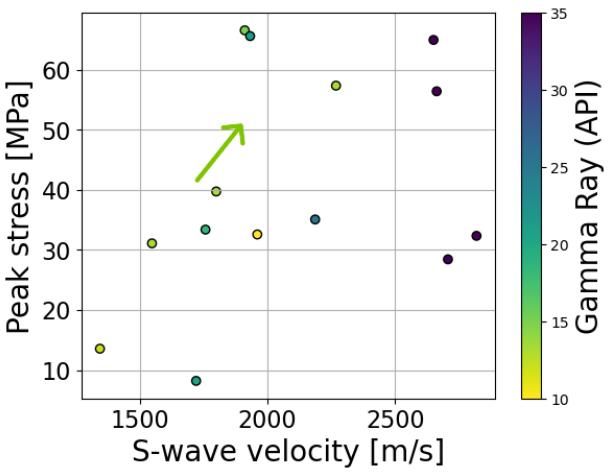

(a) Peak stress versus S-wave velocity colored by gamma ray.

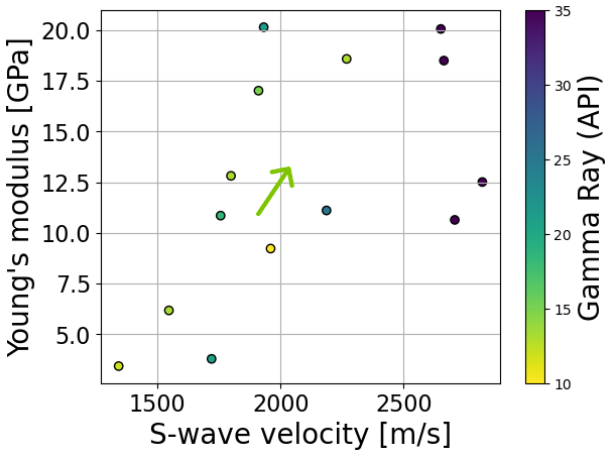

(b) Young's modulus versus S-wave velocity colored by gamma ray.

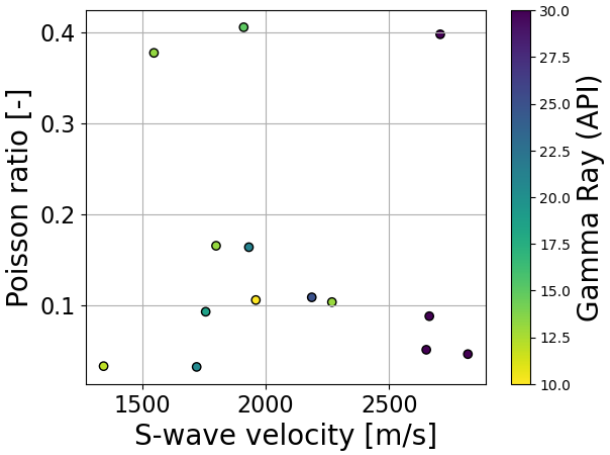

(c) Poisson ratio versus S-wave velocity colored by gamma ray.

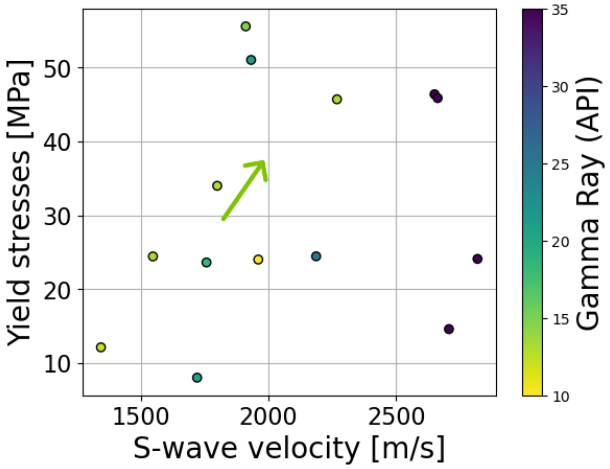

(d) Yield stress versus S-wave velocity colored by gamma ray.

Figure 19: These figures show the peak stress, Young's modulus, Poisson ratio and yield stress plotted versus the S-wave velocity, colored by gamma ray.

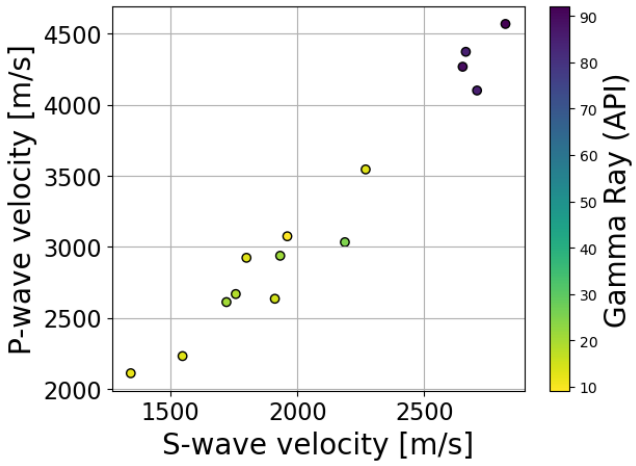

Figure 20: S-wave velocity versus the P-wave velocity, colored by Gamma ray, of all the samples which are tested on the UCS test.

Figure 21 shows again the peak stress, Young's modulus, Poisson ratio and yield stress plotted versus the bulk density and colored by the gamma ray. It is important to note that all the samples with a gamma ray value

higher than 50 (shales) are colored the same, (deep purple). While the other samples are colored by their gamma ray according to the color bar on the right hand side of each figure.
One can note that the bulk densities of the shale samples which have a high gamma ray are higher. No real correlation can be found between the bulk density and the parameters on the y-axes.

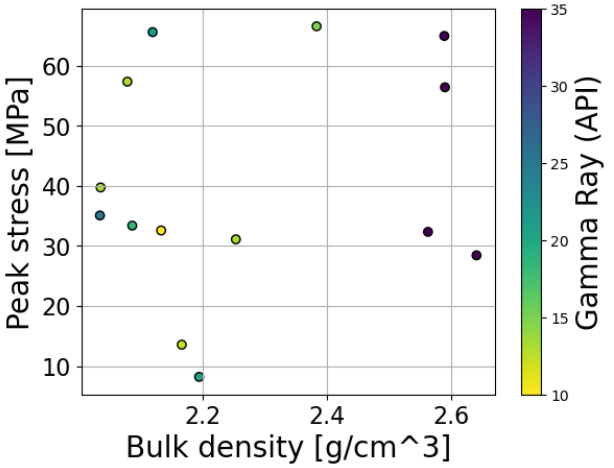

(a) Yield vs Confining Pressure colored by Porosity

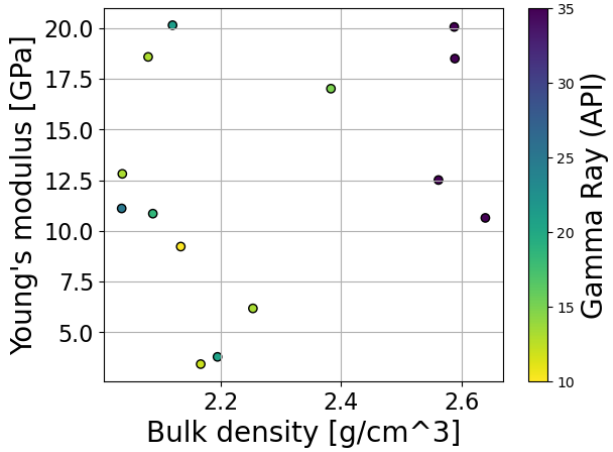

(b) Yield vs Confining Pressure colored by Gamma Ray

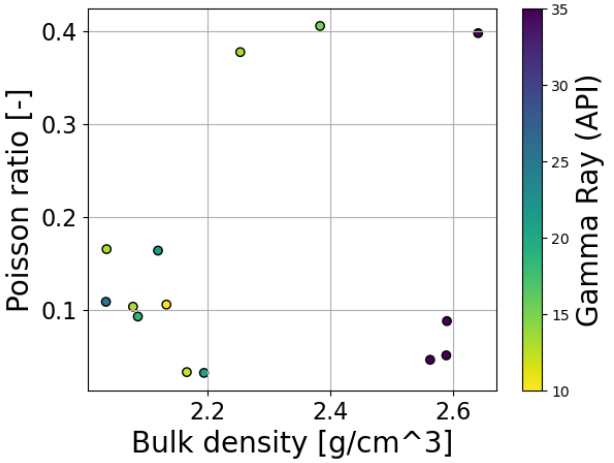

(c) Yield vs Confining Pressure colored by Vp

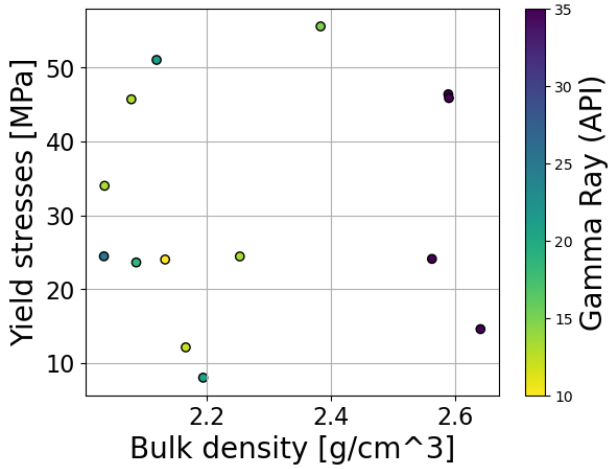

(d) Yield vs Confining Pressure colored by Vs

Figure 21: These figures show the peak stress, Young's modulus, Poisson ratio and yield stress plotted versus the bulk density of the samples, colored by gamma ray.

Figure 22 shows again the peak stress, Young's modulus, Poisson ratio and yield stress plotted versus the matrix density and colored by the gamma ray. It is important to note that all the samples with a gamma ray value higher than 50 (shales) are colored the same, (deep purple). While the other samples are colored by their gamma ray according to the color bar on the right hand side of each figure.
No real correlation can be found between the matrix density and the parameters on the y-axes.

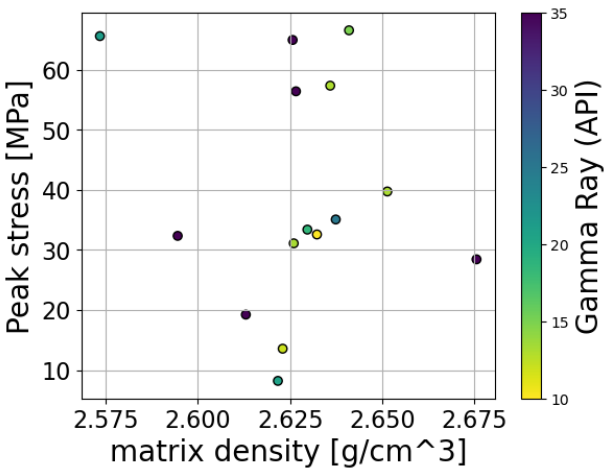

(a) Yield vs Confining Pressure colored by Porosity

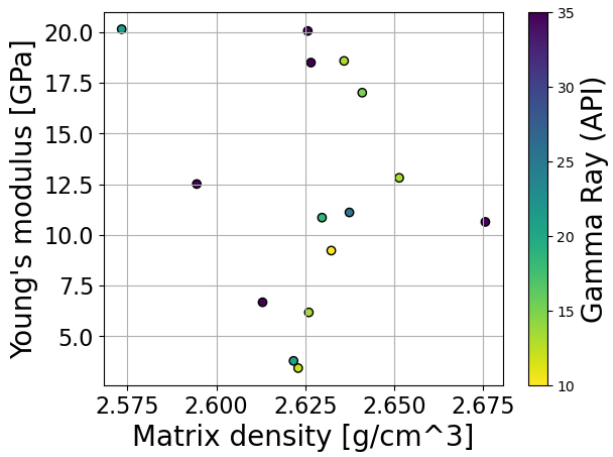

(b) Yield vs Confining Pressure colored by Gamma Ray

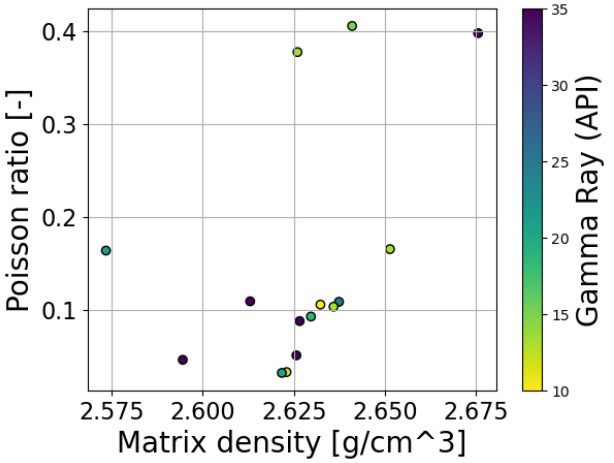

(c) Yield vs Confining Pressure colored by Vp

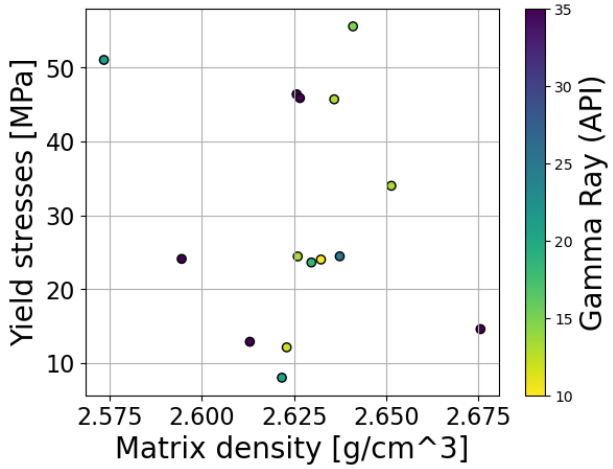

(d) Yield vs Confining Pressure colored by Vs

Figure 22: These figures show the peak stress, Young's modulus, Poisson ratio and yield stress plotted versus their matrix densities, colored by gamma ray.

The grain sizes of the tested sandstones were analyzed and plotted in Figure 59a. The three samples with the highest UCS seem to be finer grained samples. While the samples with a medium UCS (between 20 and 40 MPa) seem to be coarser grained. One sample here can be seen as an outlier to this trend, which is the sample with the lowest UCS (marked by the arrow). However, as said before, this sample is not fractured completely through the middle but only at the top. It could be that the top and bottom of this was not completely parallel, and thus that the test did not give a representation of the total strength of the sample. Therefore, there does seem to be a correlation with grain size and the unconfined compression strength of the DSSM: the finer the sandstone, the higher the unconfined compression strength.

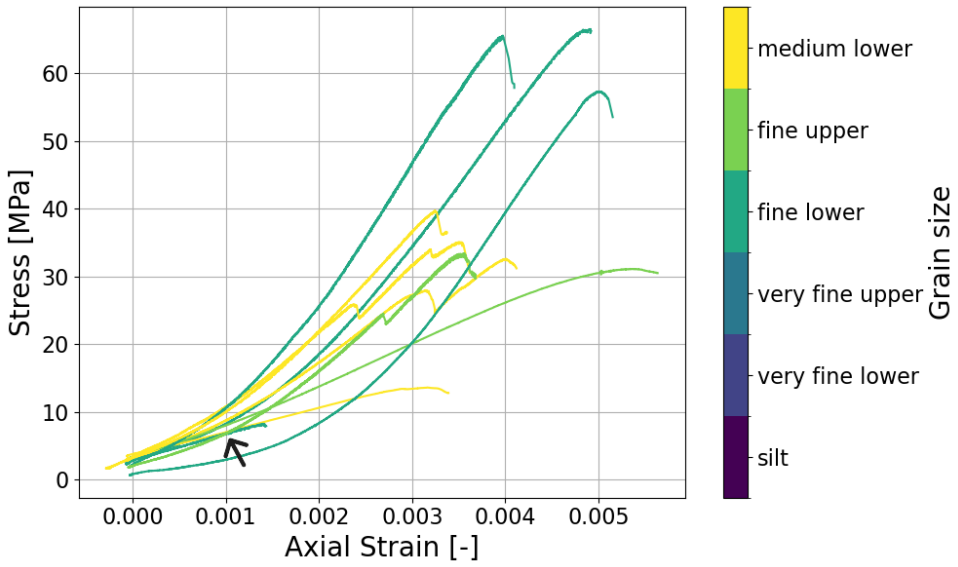

Figure 23: This plot shows the axial strain of the sandstone samples which were tested on the UCS, colored by their grain size.

Figure 59b shows the stress strain plots of the sand samples, the lines are colored by the appearance of the sample. The color of the lines do not refer to the actual color of the samples, but are linked to the legend, which has a description of the color of each sample. One can see that most of the samples which are light gray colored have a higher peak stress than the samples which are grey. These corresponds with the grain size: the finer grained samples are light grey colored and the coarser grain samples are grey.

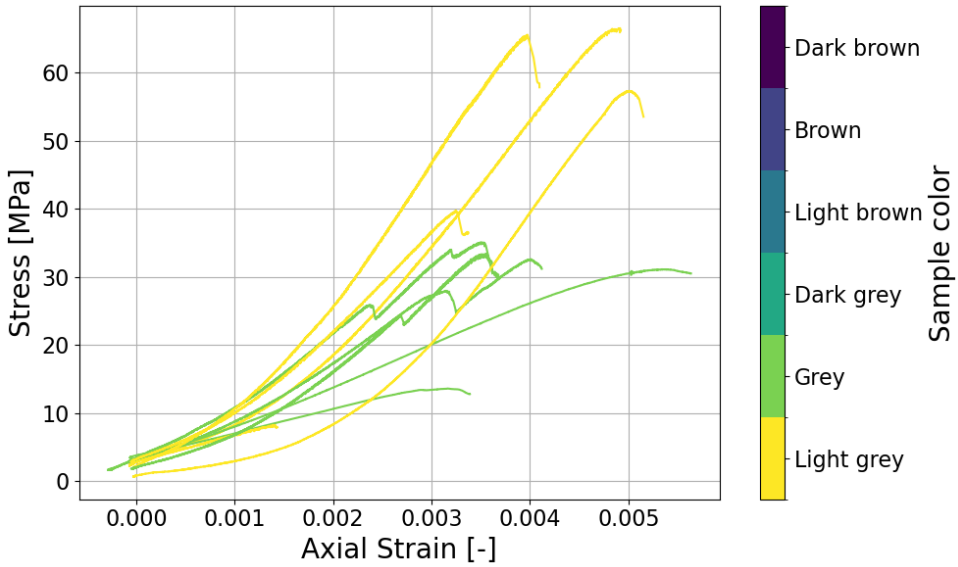

Figure 24: This figure shows the stress / strain curve for the samples tested on the UCS test, color-coded by the color of the sample. Note: line colors refer to descriptive color names, not actual appearance.

In the methodology, it is described how the samples are classified by their grain size, presence of organic material, and presence of laminations. This information for the UCS samples is plotted in Figure 25, the x axis has the categories of the grain sizes, on the y axis is the peak strength plotted, the shape of the sample describes the amount of organic matter, and the color says if the sample has laminations or not. One can notice that again that the fine sands are on average stronger than the medium sands. Other than that we cannot conclude that the samples with organic matter or laminations are weaker - due to insufficient sample size or lack of correlation.

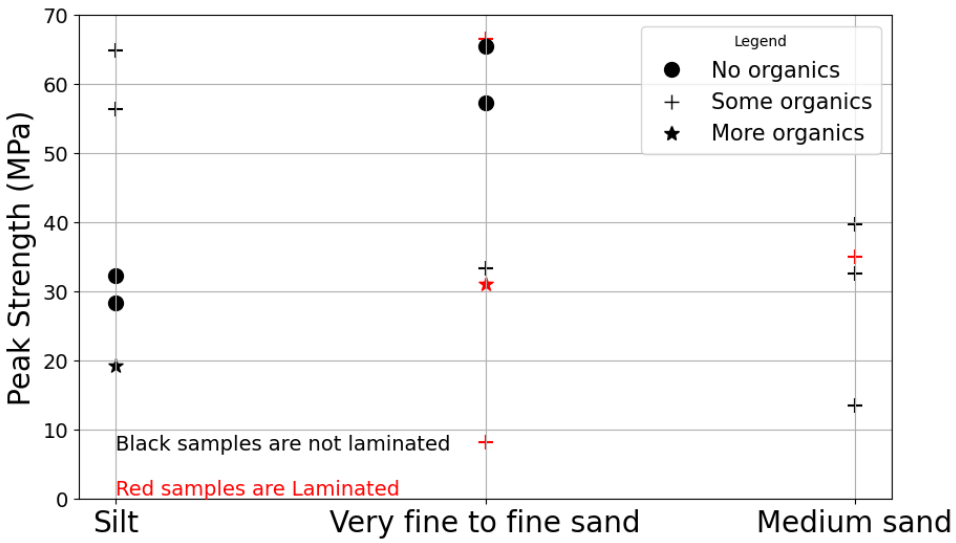

Figure 25: Grain size vs peak strength, the shape of the sample indicates how much organic matter is present in the sample, the color states if there are lamiantions present.

3.2 Triaxial tests

The direct results of the 13 samples tested triaxially are the stress/strain plots. Figure 26 shows the strain plotted vs the axial deviatoric stress of all the samples that were tested under different confining pressures. One sample is highlighted to be able to see the stress strain pattern. One can see for this sample that for each stress step, the slope, and thus the Young's modulus increases. One can note there is quite a range in the peak stresses in this plot.

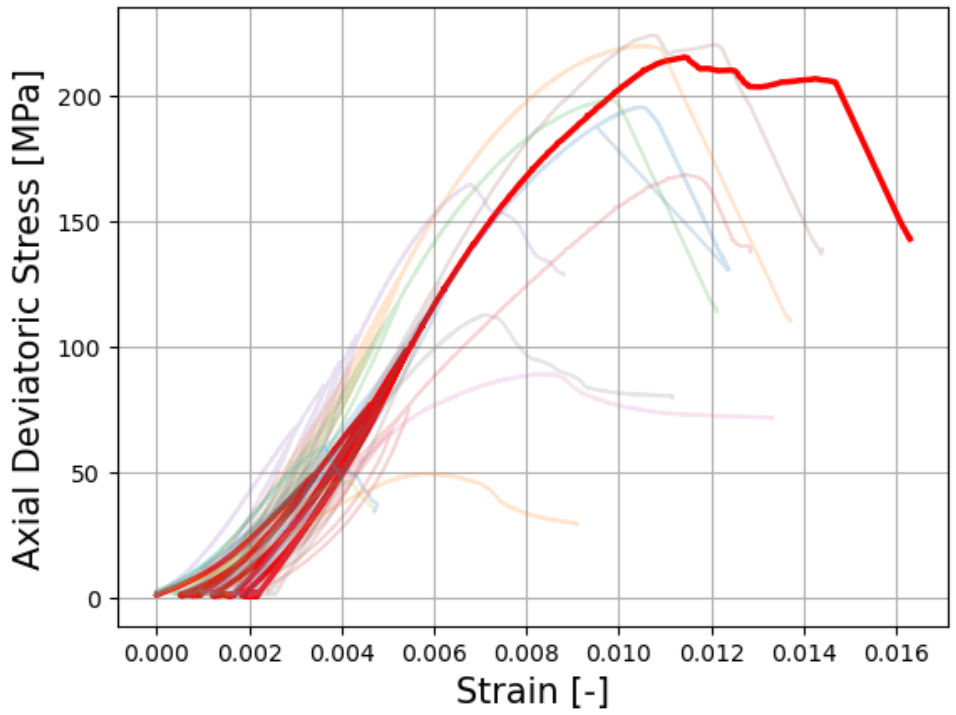

Figure 26: This figure shows the strain plotted versus the axial deviatoric stress for all the samples which were tested triaxially. One sample is highlighted to be able to see the stress strain pattern.

All the indirect results which were gathered from the triaxial test are shown here in Table 3. "E0.5" represents the Young's modulus [GPa] at confining pressure 0.5 MPa. "Y0.5" stands for the yield point at 0.5 MPa confining pressure. "Peak" stands for the peak strength at which the sample broke.

Table 3: Results from the triaxial tests. "E0.5" stands for the Young's modulus [GPa] at 0.5 MPa confining pressure. "Y0.5" stands for the yield point at 0.5 MPa confining pressure. "Peak" stands for the peak strength at which the sample broke.

ID	E0.5 GPa	E5 GPa	E10 GPa	E20 GPa	E30 GPa	E40 GPa	Y0.5 MPa	Y5 MPa	Y10 MPa	Y20 MPa	Y30 MPa	Y40 MPa	Peak MPa
C5-3-PB44	-	20.62	24.33	27.63	29.88	-	66.68	88.34	104.2	118	-	-	195.2
C6-17-PT33	-	19.29	24.49	29.84	33.5	-	45.33	64.53	95.76	109.39	-	-	215.1
C7-3-PB10	-	27.78	32.26	35.02	37.02	-	70.97	90.15	105	108.1	-	-	219.6
C7-5-PB12	-	27.78	32.14	34.94	37.75	-	65.07	81.79	93.81	108.7	-	-	197.9
C6-7-PT23	-	26.95	34.55	39.07	43.65	46.46	-	61.89	67.92	81.16	90.71	94.42	164.4
C6-11-PT27	21.4	-	-	-	-	-	-	42.04	-	-	-	-	55.4
C2-3-PB72	-	14.93	-	-	-	-	-	41.6	-	-	-	-	51.15
C6-15-PT31	-	19.69	25.97	31	34.8	36.87	-	57.08	82.98	95.9	104.5	125	223.8
C5-1-PB42	15.94	-	-	-	-	-	-	41.39	-	-	-	-	41.39
C6-13-PB30	-	15.43	21.26	23.31	25.1	-	-	49.1	56.73	67.79	74.36	-	168.26
C6-21-PB38	-	10.92	-	-	-	-	-	37.65	-	-	-	-	49.15
C2-11-PT79	-	12.53	19.53	22.81	27.32	-	-	25.45	30.24	34.21	26.15	-	89.04
C6-1-PB18	-	18.22	24.56	27.94	31.93	-	-	44.89	51.2	53.65	60.59	-	112.5

Figure 27 shows one test of sample C6-17-PT33, broken down into the four different stress-strain steps. Each step is done until the sample starts to yield, except for the last step which is done until failure. Figure a is the stress/strain step at 5 Mpa confining pressure. Figure b is at 10 Mpa confining pressure. Figure c is at 20 Mpa confining pressure. Figure d is at 30 Mpa confining pressure, this test was done until failure. One can note that the slope increases with increasing confining pressure, which is expected. From each step is the yield point attained by analyzing the stress derivative with time, and seeing where it's not linear anymore. Then, the slope of the linear part of the stress strain curve is attained by dividing the stress over the strain at the interval of 70 to 90 % of the yield stress. For the last step, where the sample broke, the peak stress is attained, which is the highest point at which the stress curve was.

Figure 28 shows the 4 steps combined. One can note here that the yield point increases with confining pressure and that the slope of the linear part of the stress-strain curves increases, meaning the sample becomes stiffer and has a higher Young's modulus. This all is as expected.

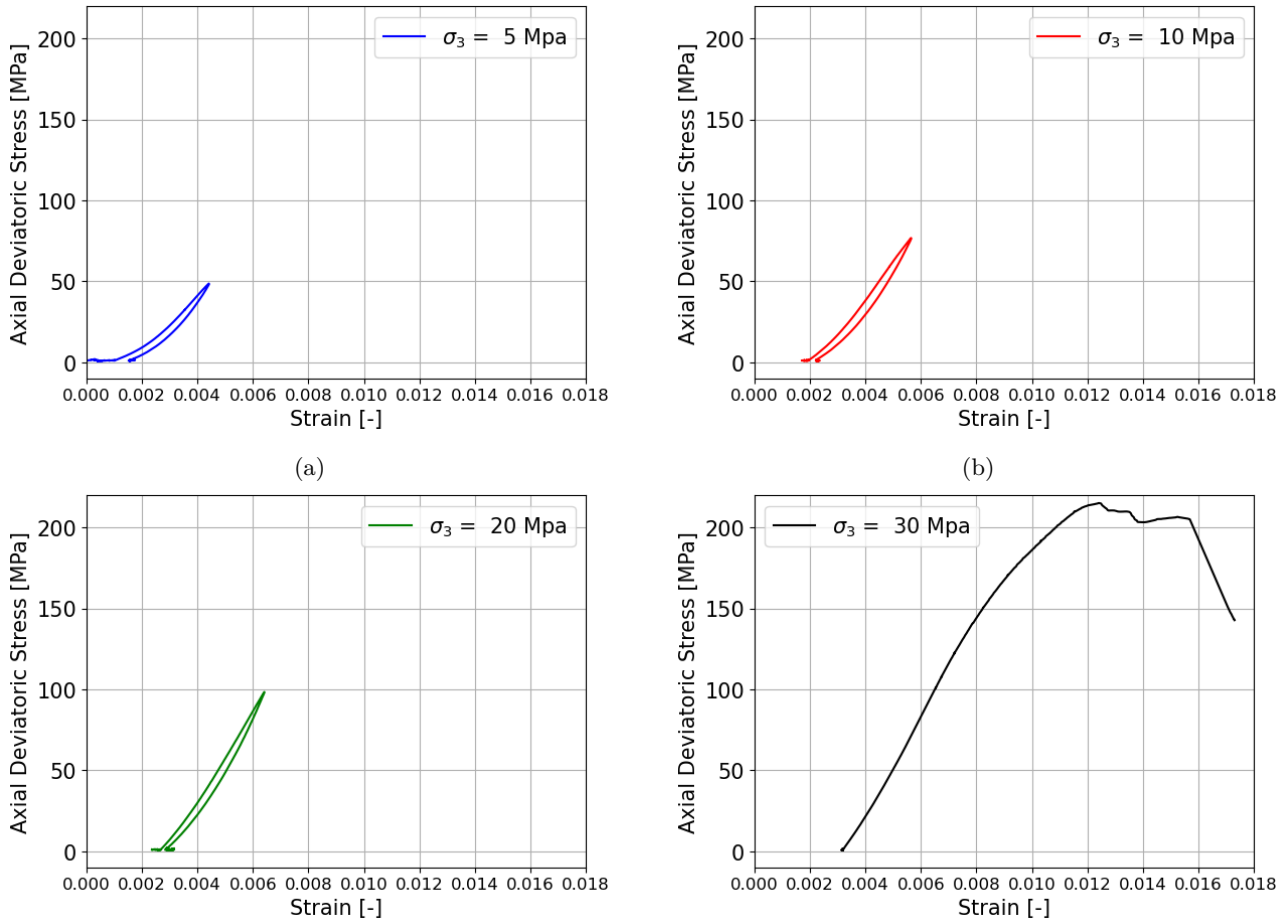

(a) (b) (c) (d)

Figure 27: The four different stress strain steps for the different confining pressures are shown here. Figure a is the stress/strain step at 5 Mpa confining pressure. Figure b is at 10 Mpa confining pressure. Figure c is at 20 Mpa confining pressure. Figure d is at 30 Mpa confining pressure, this test was done until failure, the others were done until the yield point. One can note that the slope increases with an increasing confining pressure, which is expected.

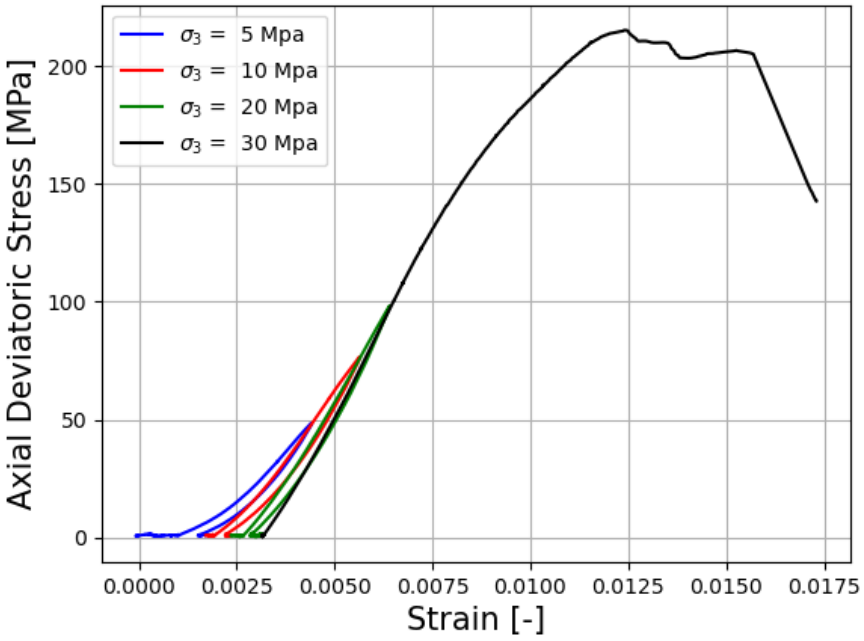

Figure 28: The four stress/strain steps of sample C6-17-PT33 combined.

Figure 29 shows four plots where the confining pressure is plotted versus the yield point, colored by different petrophysical parameters: The porosity, the gamma ray value, the P-wave velocity and the S-wave velocity. One should note that for the same sample, the yield points are connected to be able to follow a sample. The lines do not represent measured values. The values which are plotted as a circle represent sand samples, the ones plotted as crosses are shale samples.

For almost all samples, the yield points increase with an increasing confining pressures. Especially for the high porosity samples at low confining pressures there is a high increase in the yield points. The yield point seems to increase with increasing confining pressure in a convex way. This effect is less observed for the lower porosity samples. It is expected that with higher confining pressures, the yield points increase until a certain point where they plateau. Two samples were tested at higher confining pressure (40 MPa) to see if this effect was already visible. The sand sample does not seem to show this behavior yet, while the shale sample does.

For low confining pressures, the yield points are in between 35 and 72 MPa, at higher confining pressures, they range between 35 up to 125 MPa.

In Figure 29a one can note that the higher porosity samples have a higher yield point for each confining pressure. The high porosity samples also seem to converge more to the same result as the confining pressure increases, compared to the lower porosity samples. In general, it is not expected that samples with a higher porosity are stronger. However, here there is also a difference in mineralogy.

All samples were fairly easy to classify as sandstone or shales. However, one sample from the triaxial sample set stood out. That is the sample pointed out by the blue arrow in Figure 29a: $C6-13-PB30$, see Figure 32 for a picture. It has a porosity, P-wave and s-wave velocity compared to the other shales, but the gamma ray reading is like it is a sandstone. In the triaxial test it behaves more like a shale.

In general, one can note the following about Figure 29: The sand samples have a lot less spread in their yield points compared to the shales. The magnitude of yield points at different confining pressures is also higher for the sand samples compared to the shale samples. The yield points of the sand samples appear to be more predictable, especially at higher confining pressures, compared to the shale samples.

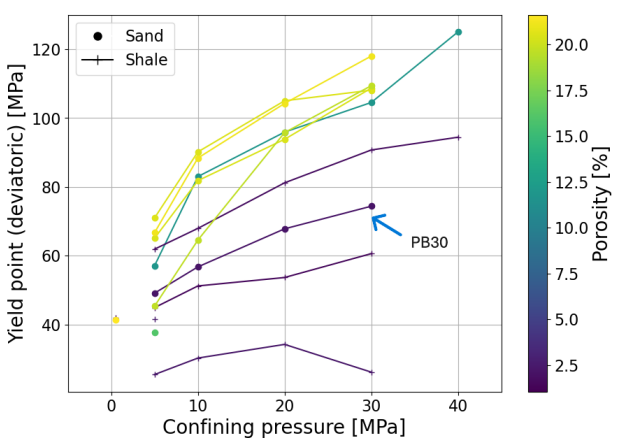

(a) Yield vs Confining Pressure colored by Porosity

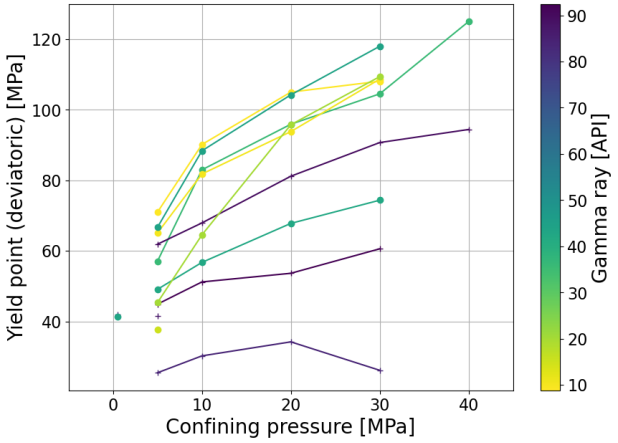

(b) Yield vs Confining Pressure colored by Gamma Ray

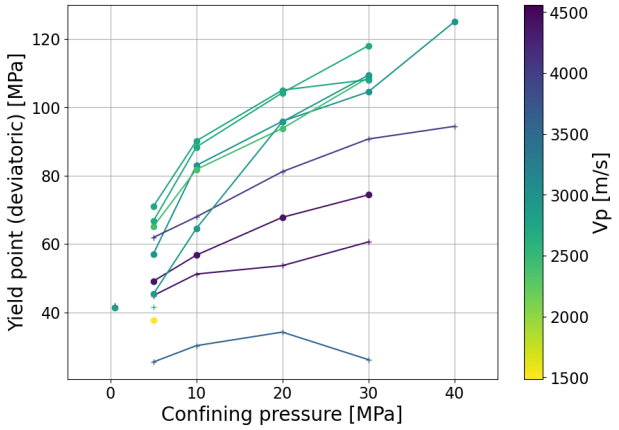

(c) Yield vs Confining Pressure colored by Vp

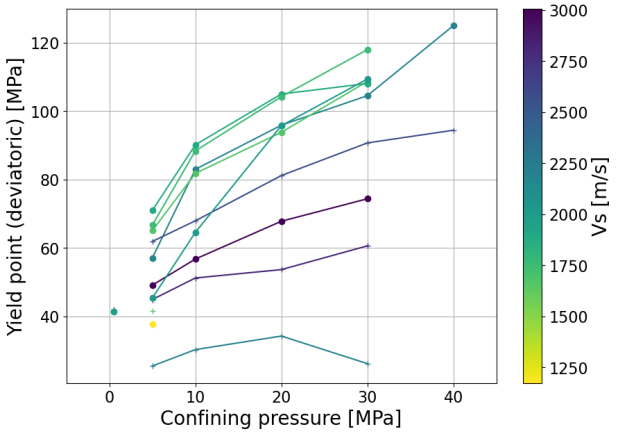

(d) Yield vs Confining Pressure colored by Vs

Figure 29: Comparison of yield points as a function of confining pressure and various petrophysical properties. One should note that for the same sample, the yield points are connected to be able to follow a sample. The lines do not represent measured values, that are just the points plotted. The values which are plotted as a circle represent sand samples, the ones plotted as crosses are shale samples.

As an addition Figure 30 and Figure 31 show the same plots but then colored by density and grain density, respectively. The same correlation as before can be seen in Figure 30; the samples with a lower density (which are the sands) have higher yield points. No real correlation can be seen for the grain density in Figure 31.

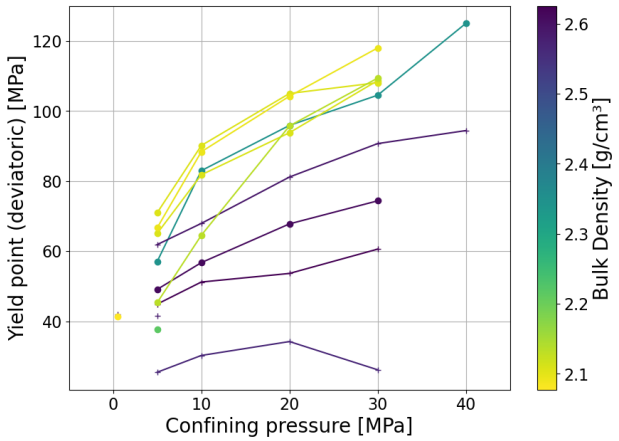

Figure 30: Yield point vs. confining pressure colored by bulk density.

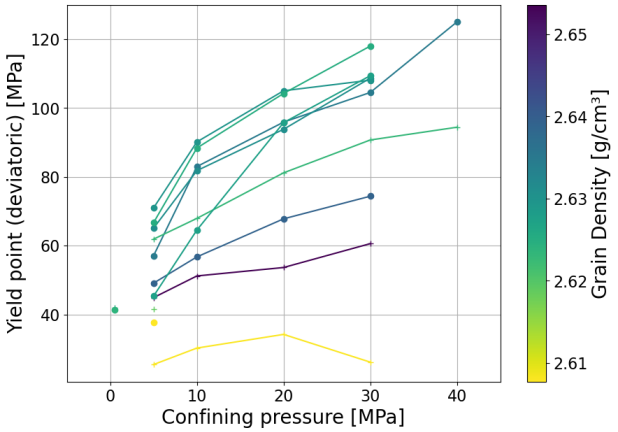

Figure 31: Yield point vs. confining pressure colored by grain (matrix) density.

Figure 32: Sample $C6 - 13 - PB30$, the sample that was more difficult to classify as sand or shale.

Figure 33 shows four plots where the confining pressure is plotted versus the Young's modulus, colored by different petrophysical parameters: The porosity, the gamma ray value, the P-wave velocity and the S-wave velocity. One should note that for the same sample, the Young's moduli are connected to be able to follow a sample. The lines do not represent measured values. The values which are plotted as a circle represent sand samples, the ones plotted as crosses are shale samples.

One can note for each sample, there is an increase in Young's modulus with an increasing confining pressure, which was expected. At lower confining pressure, the samples show a higher increase in Young's modulus. It is expected that with increasing confining pressure, at some point the Young's modulus starts to plateau. This is not yet seen for samples which were tested at a confing pressure of 40 MPa. For each petrophysical parameter, it is difficult to find trends. Both for the sands and the shales is a high spread in values visible, for each confining pressure. The spread seems to stay constant with confining pressure, it does not increase with increasing confining pressure like it did for the yield points.

Figure 34 and Figure 35 show the same plots but then colored by density and grain density, respectively. In these plots, no other correlation can be found.

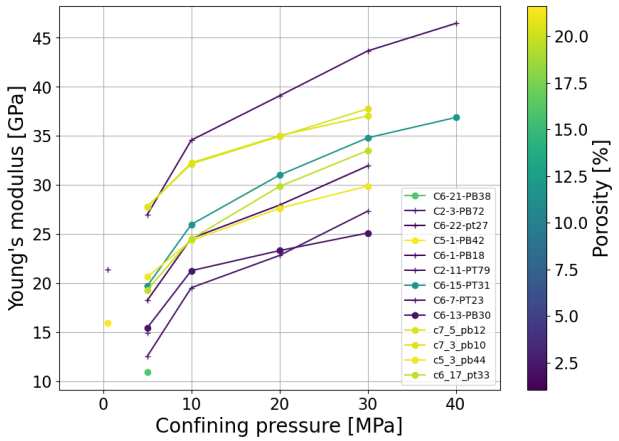

(a) Young's modulus vs Confining Pressure colored by Porosity

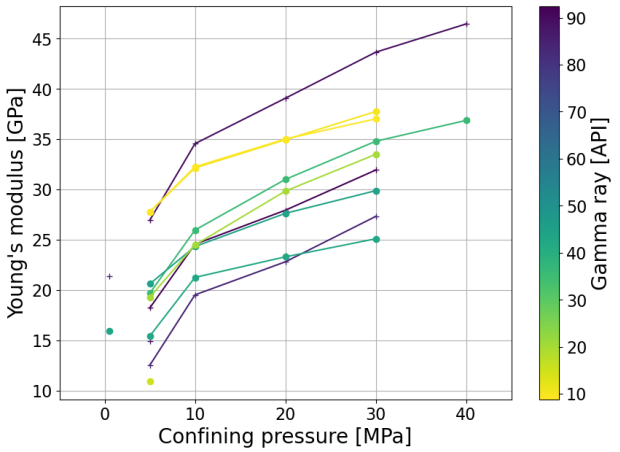

(b) Young's modulus vs Confining Pressure colored by Gamma Ray

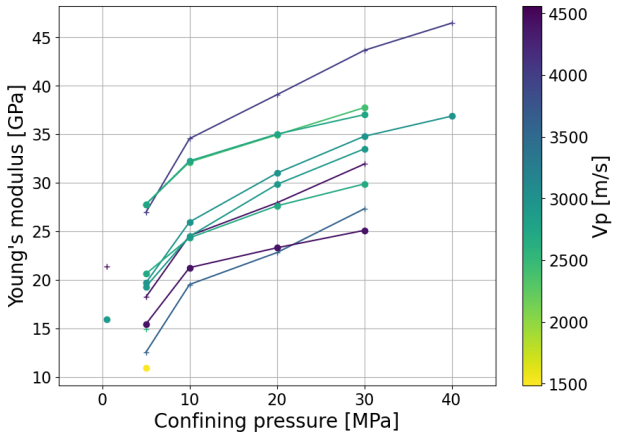

(c) Young's modulus vs Confining Pressure colored by Vp

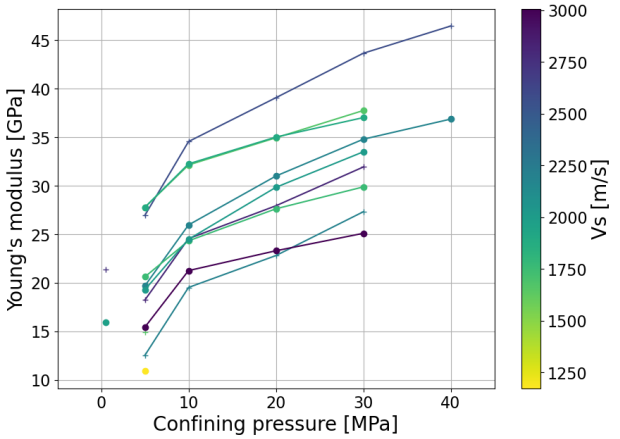

(d) Young's modulus vs Confining Pressure colored by Vs

Figure 33: Comparison of Young's moduli as a function of confining pressure and various petrophysical properties.

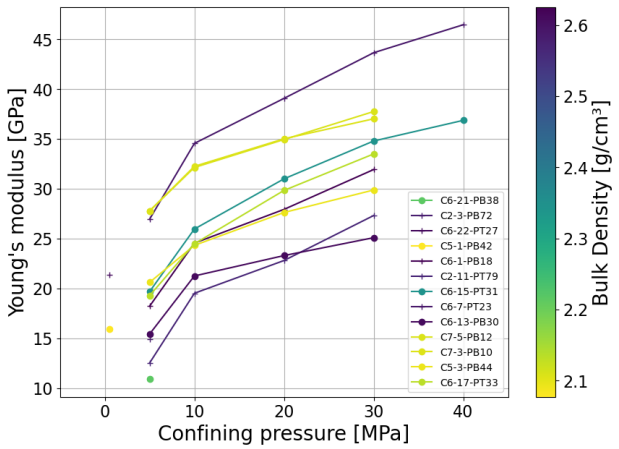

Figure 34: Young's modulus vs. confining pressure colored by bulk density.

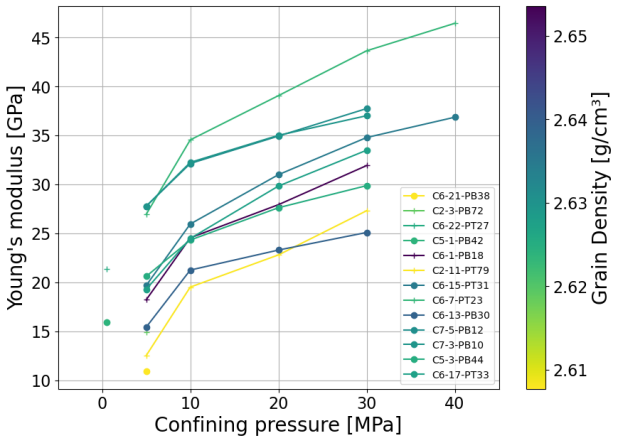

Figure 35: Young's modulus vs. confining pressure colored by grain (matrix) density.

For only the sand samples was the Young's modulus plotted versus the confining pressure and colored by the grain size of each sample, this is shown in Figure 36. It seems that the samples consisting of finer grained sand have lower Young's modulus than the courses grained samples. There is however one outlier to this correlation, which is the sample appointed by the arrow.

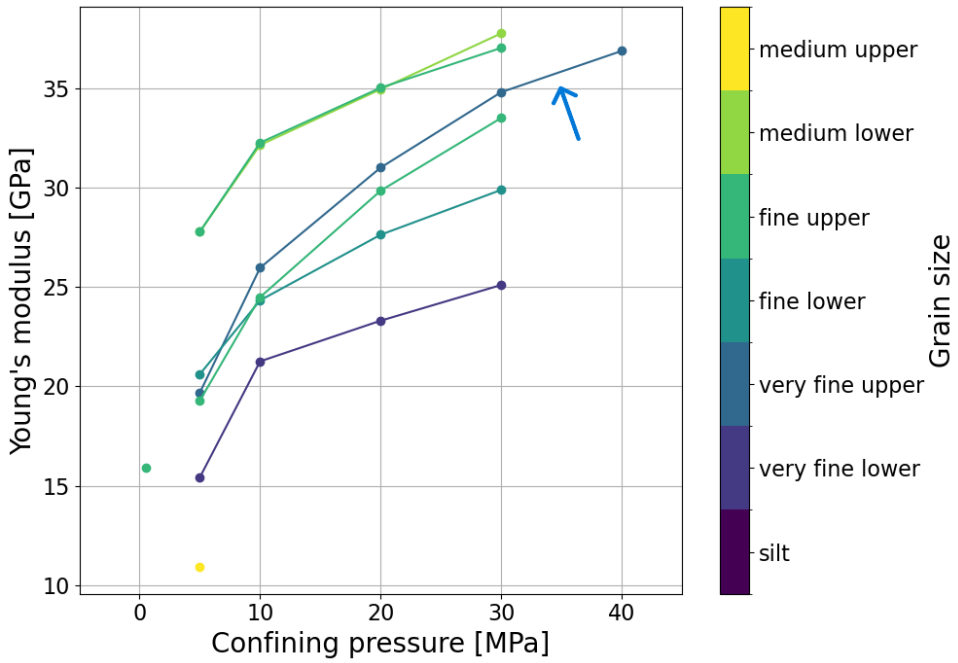

Figure 36: Young's modulus plotted versus confining pressure, colored by grain size. Here are only the sand samples plotted which were tested on the triaxial test, no shales. The sample appointed by the arrow is the sample which is an outlier to the trend with grain size and Young's modulus.

Figure 37 shows the peak stress each sample reached, right before it failed at the maximum confining pressures. The samples plotted with circles are tested until 30 MPa confining pressure. The samples which are plotted with a cross, are tested until 40 MPa confining pressure. One can note, that the shales have a lower maximum stress than the sand samples. One can also note that the samples which are tested at 40 MPa confing pressure, have a higher maximum stress than the others within the same lithology, which is expected.

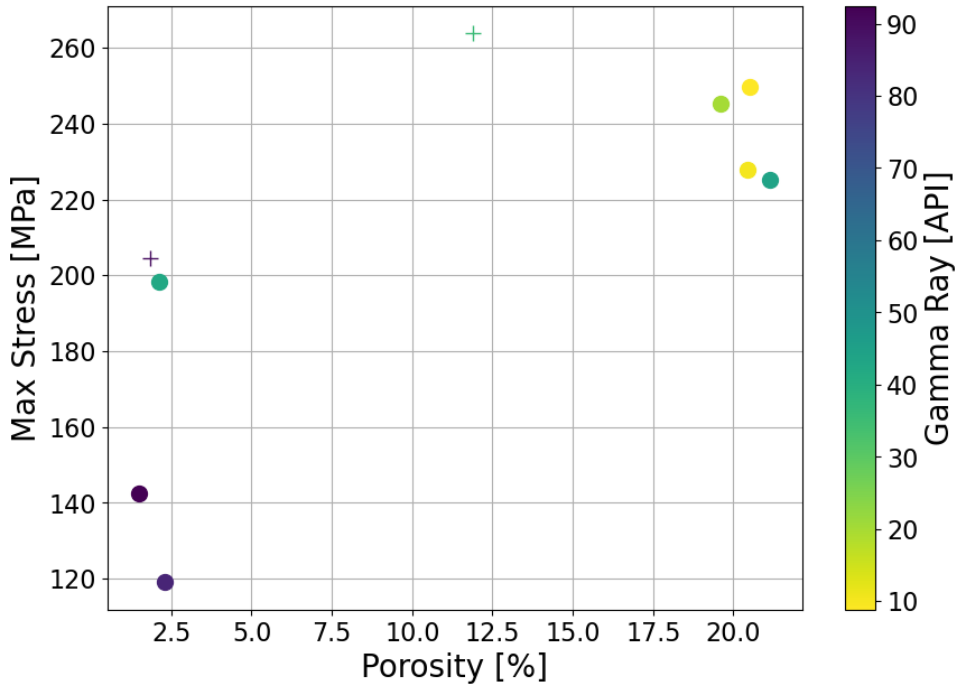

Figure 37: This shows the peak stress each sample reached right before it failed at the maximum confining pressures. The samples plotted with a cross failed at a confining pressure of 40 MPa, the others at 30.

Every sample that was tested on the triaxial test showed a nice fracture of roughly 60 °. There was one sample which seemed to have fractured horizontally, which could indicate an unsuccessful test. This was sample

C6-21-PB38, The CT-scans which were made after this sample was tested show however that the sample did completely break through the middle, See Figure 38. One can also see that the sample broke along a piece of lignite, indicating that these are weak points in the sample. The piece of lignite is indicated by a blue arrows.

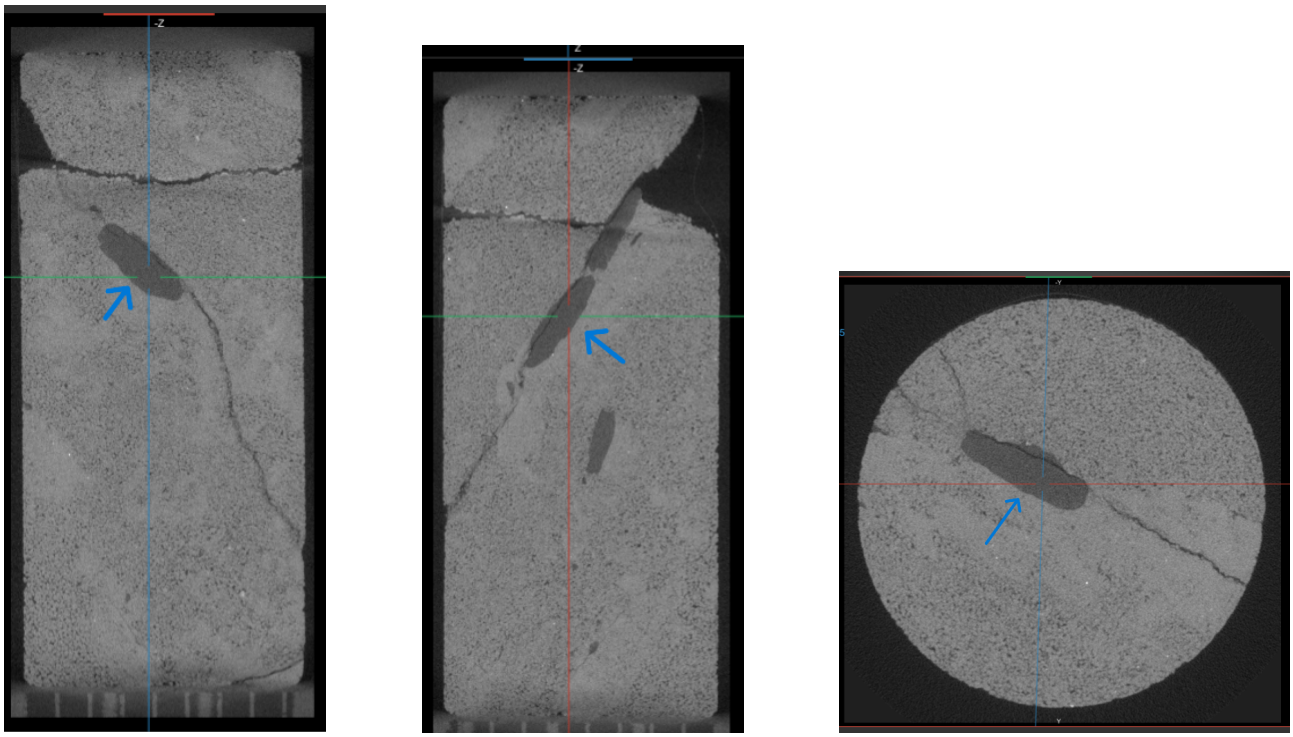

(a) vertical cross section 1 (b) vertical cross section 2 (c) horizontal cross section

Figure 38: Sample C6-21-PB38 after the triaxial test.

3.2.1 Inelastic Strain

If each sample behaved perfectly elastic, it would return exactly on the same stress-strain path as it took when the stress was increased. As one can see in Figure 27, the returning stress-strain path is not the same as the increasing stress-strain path. This means that the sample exhibited some inelastic strain. Figure 39 shows the first stress step of sample $C6-17-PT33$. The red point in the figure marks the start of the first stress step, the orange point marks the end. For each sample the amount of inelastic strain per stress step was calculated. Figure 40 shows the stress plotted versus measurement index of the experiment. The data was smoothed to be able to pick the minima, which represent the beginning and the end of each stress step. From this index the strain was calculated. Also, the index of the peak stress at the last cycle was attained, that point is represented by the green point in Figure 40.

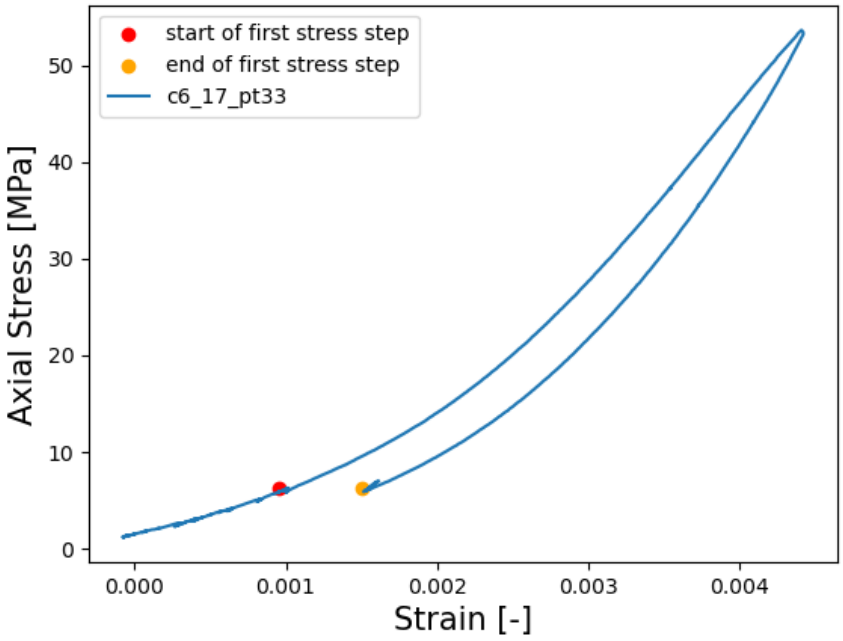

Figure 39: This shows the first stress step of sample $C6-17-PT33$. The red point in the figure marks the start of the first stress step, the orange point marks the end.

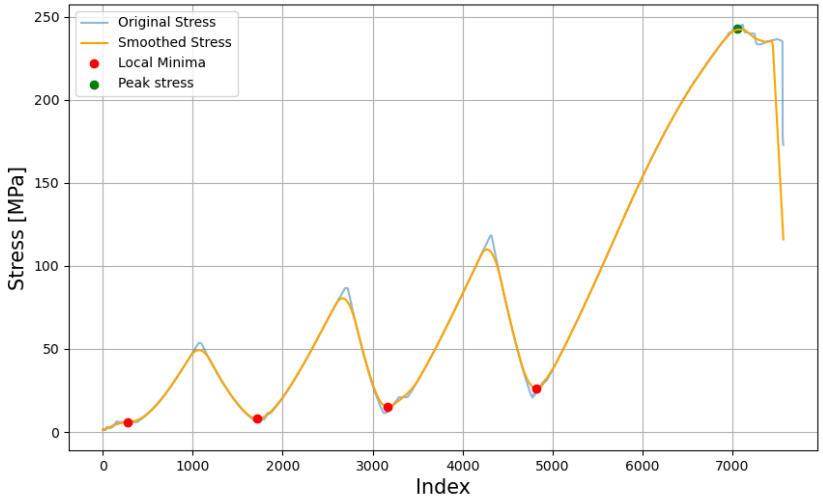

Figure 40: Index plotted versus stress. The data are smoothed to easily pick the minima points which mark the beginning and end of each stress step, pointed out by the red point. The green point marks the peak stress.

Figure 41 shows the inelastic strain for each stress step, indicated by the confining pressure of that stress step. The samples are colored by their porosity. One can note that for the first stress steps, the elastic strain was the highest, and it also has the highest variability between each sample. The second, third and fourth stress steps show similar amounts of inelastic strain, which is significantly lower than the first stress step. To be able to distinguish between sands and shales were the boxplots in Figure 42 made. The boxplots for the sands are brown colored and the shales are grey colored. In the first stress step, the shales have a higher amount of inelastic strain. At the other stress steps the sands and shales are behaving similar in terms of inelastic strain.

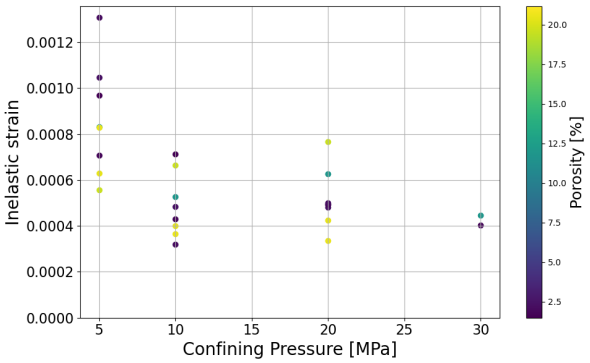

Figure 41: This figure shows the inelastic strain experienced by each sample per stress step, colored by porosity.

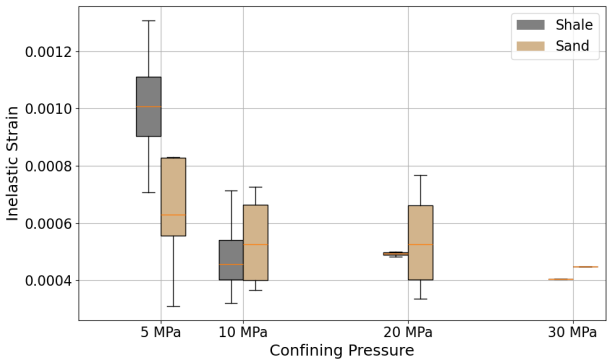

Figure 42: This shows the friction angle of each samples plotted versus its porosity and colored by its gamma ray value.

Figure 43 shows the amount of strain each sample experienced from the beginning until the last stress step when the sample failed under its peak stress. The two samples indicated by the two blue arrows are the only two tested in five stress steps, while the other samples only underwent four stress cycles. There is a clear with decreasing gamma ray value, the samples exhibit more strain before failure.

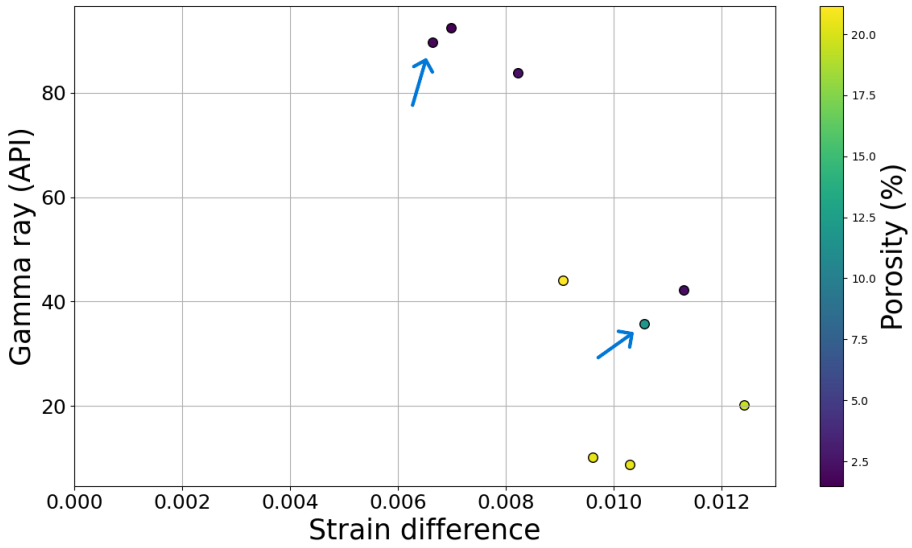

Figure 43: This plot shows the amount of strain the sample experienced from the start of the experiment until the last stress step at its peak stress. Each sample is tested until yielding at 5, 10 and 20 MPa and tested until failure at 30 MPa. The samples with an arrow are tested until failure at 40 MPa.

3.2.2 Mohr-Coulom Yield Criteria

Figure 44 shows an example of how, for each sample tested at different confining pressure, the Mohr-Coulomb yield criterion was found. The Mohr circles were drawn based on the yield point and its confining pressure. They were plotted, and a linear line was fitted to the circles, representing the Mohr-Coulomb yield criterion from which the cohesion value and friction again was attained. Table 4 shows the friction angle and cohesion value for each test.

Table 4: Friction angle and cohesion values for the samples

ID	fric	Coh
C5-3-PB44	31.01	18.01
C6-17-PT33	35.14	9.29
C7-3-PB10	25.52	21.75
C7-5-PB12	30.55	17.1
C6-7-PT23	19.71	20.86
C6-11-PT27	-	-
C2-3-PB72	-	-
C6-15-PT31	27.93	16.88
C5-1-PB42	-	-
C6-13-PB30	11.31	22.21
C6-21-PB38	-	-
C2-11-PT79	19.35	6.78
C6-1-PB18	12.91	17.22

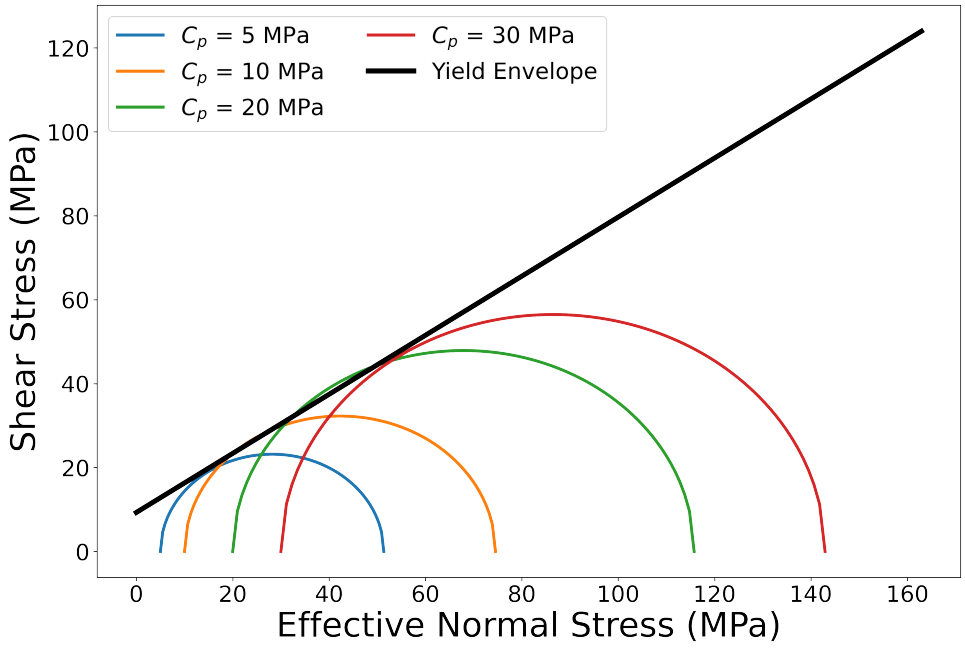

Figure 44: An example of how the Mohr-Coulomb Yield criterion is fitted to the data of a sample.

When for each sample the Mohr-Coulomb yield criteria are plotted, Figure 45 is attained. One can clearly see two groups: the lower porosity samples, which have a low friction angle, and the high porosity samples which have a higher friction angle. No clear trend can be seen in the cohesion values from this plot.

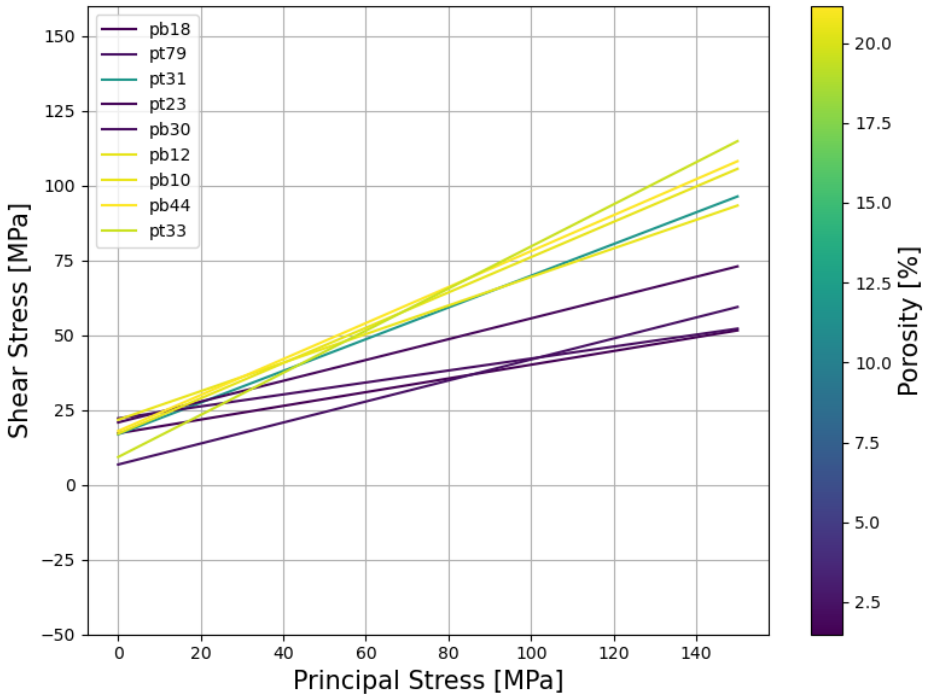

Figure 45: Mohr-coloumb yield criteria plotted, colored by porosity. The lower porosity samples seem to have a lower friction angle than the high porosity samples. From this figure no correlation can be found between the cohesion value and the porosity.

Figure 46 shows the cohesion value of each samples plotted versus its porosity and colored by its gamma ray value. No real correlation or trend can be found, for both the low and high porosity samples.

Figure 47 shows the friction angle plotted versus porosity, colored by a gamma ray. The friction angle seems to be lower for the low porosity samples, but a real trend with porosity might be difficult to classify because of the lack of samples with a medium porosity. This is also difficult because two different lithologies are combined. From this can be concluded that the sand samples have a higher friction angle than the shale samples.

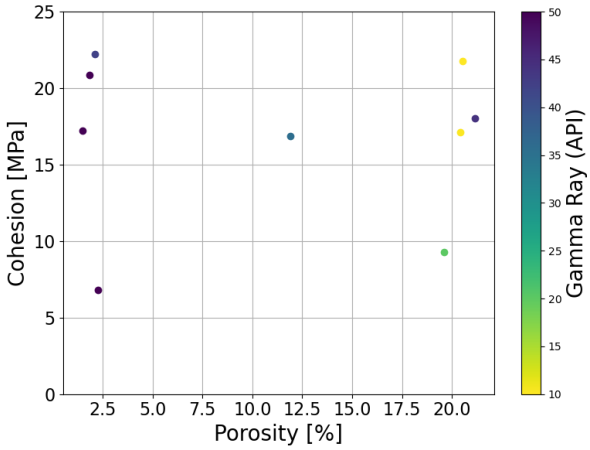

Figure 46: This shows the cohesion value of each samples plotted versus its porosity and colored by its gamma ray value.

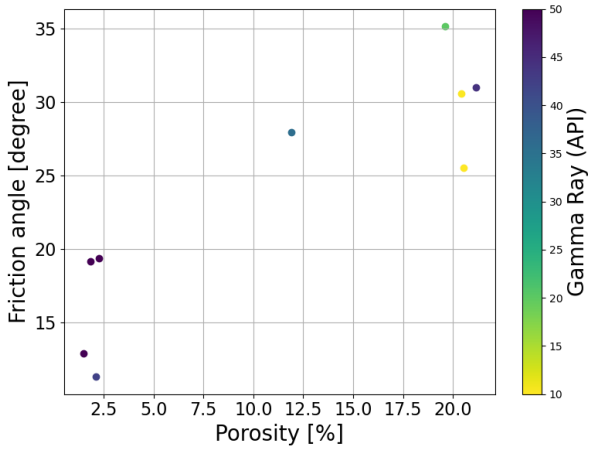

Figure 47: This shows the friction angle of each samples plotted versus its porosity and colored by its gamma ray value.

The cohesion value is plotted versus the friction angle in Figure 48. Within the sand samples one can see an inverse trend with cohesion and friction angle. Sand samples with a higher friction angle, have a lower cohesion value. However, there are not many samples to support this but the trend within these samples is visible.

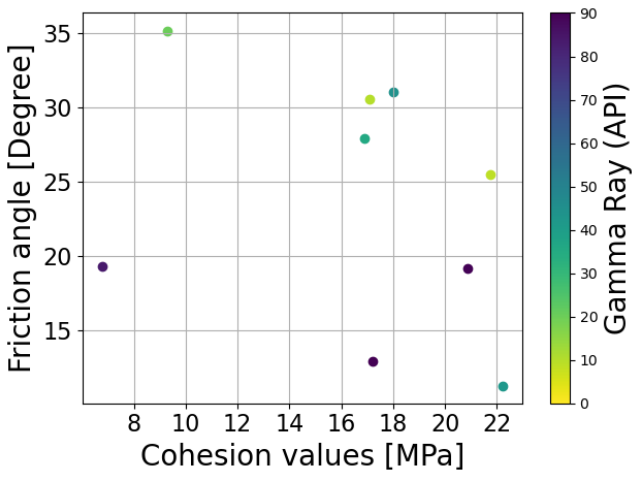

Figure 48: cohesion value versus friction angle, colored by gamma ray.

In addition are the cohesion values plotted versus the porosity and colored by the bulk density and the grain density, Figure 75 and Figure 53 respectively. No trends are visible.

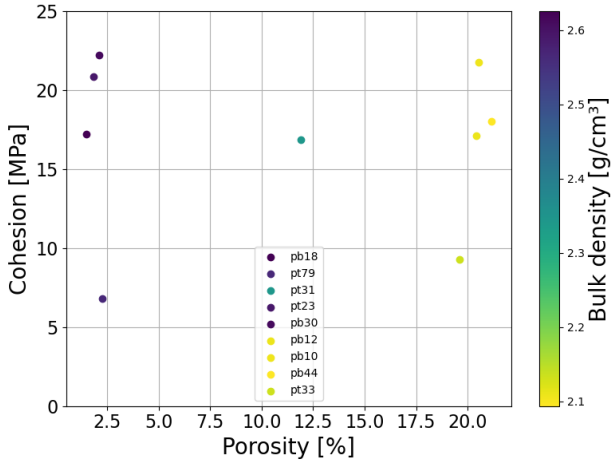

Figure 49: Friction angle plotted versus porosity colored by bulk density.

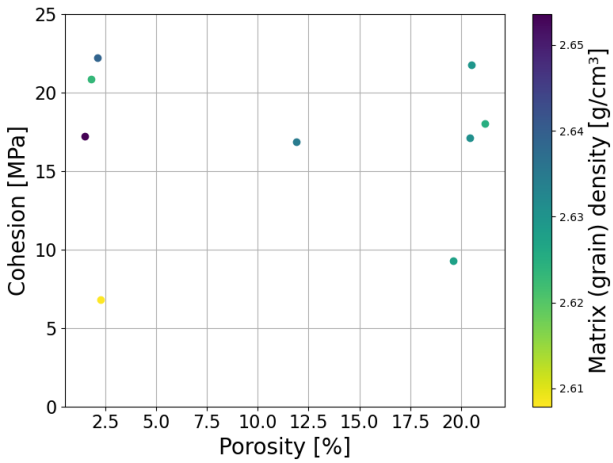

Figure 50: friction angle plotted versus porosity colored by grain density.

The friction angle is also plotted versus the porosity and colored by the bulk density and the matrix density in Figure 51 and Figure 52. Here the same trend as in Figure 47 is visible; the sands, which have a lower density have a friction angle.

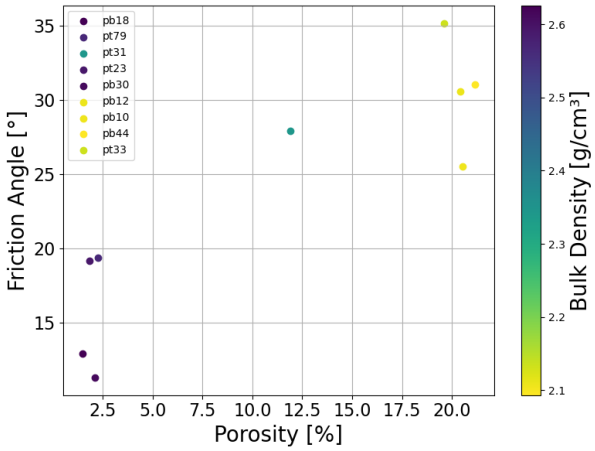

Figure 51: Friction angle plotted versus porosity colored by bulk density.

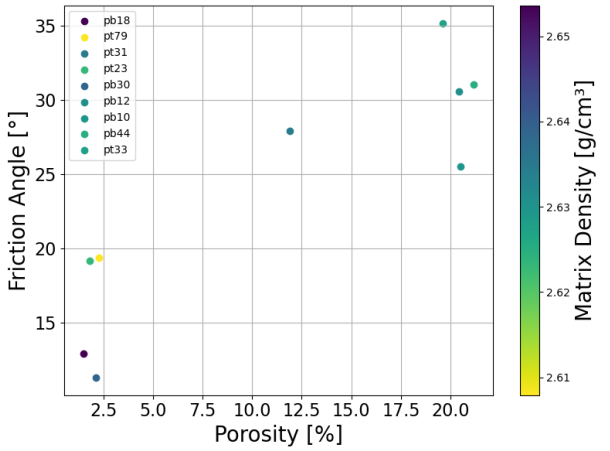

Figure 52: friction angle plotted versus porosity colored by grain (matrix) density.

When the porosity is plotted versus the cohesion value, which was attained from the Mohr-Coulomb Yield criteria, colored by the grain size, Figure 53 is generated. No real correlation can be found with the grain size. Figure 54 shows the porosity plotted versus the friction angle, colored by grain size. One can see again that the shales, which are fine grained have a lower friction angle than the sands, which are courser grained. Within the sands no real correlation can be found.

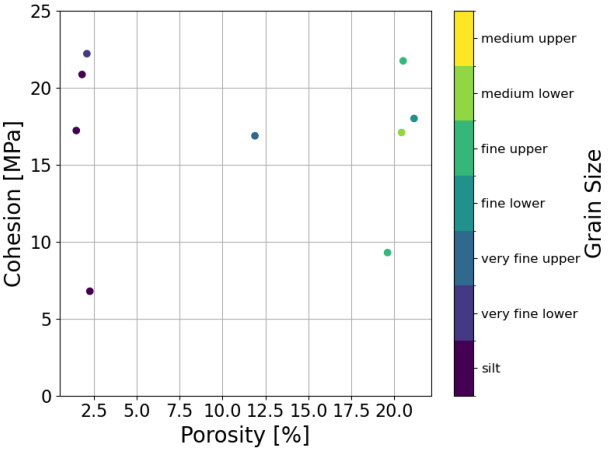

Figure 53: Porosity plotted versus the cohesion values attained from the Mohr-Coulomb Yield criteria, colored by grain size.

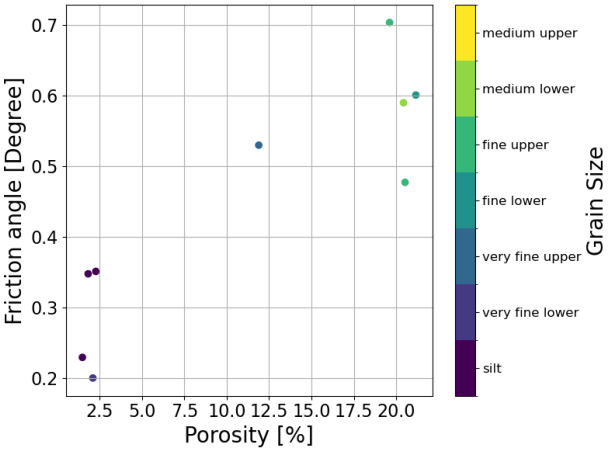

Figure 54: Porosity plotted versus the friction angles attained from the Mohr-Coulomb Yield criteria, colored by grain size.

3.3 Brazilian disc tests

Figure 55 shows the stress-strain plot for each sample which was tested using a Brazilian disc test. One curve that stands out is $C4-1-PB52$. Upon examination of the sample after the test it became clear that the sample did not break straight through the middle, which can be seen as an invalid test according to [6]. Therefore, this sample will be disregarded.

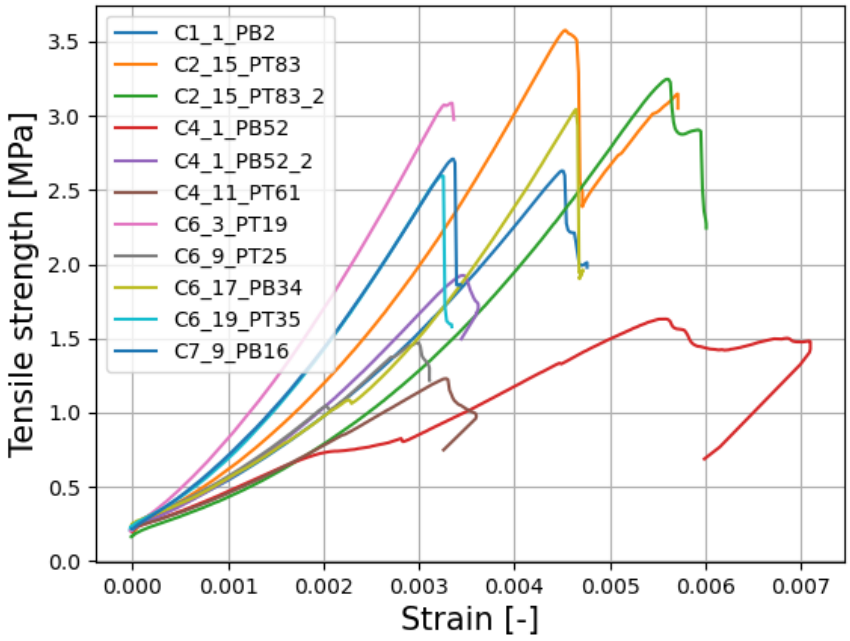

Figure 55: This figure shows the stress/strain plot for each sample. Sample $C4-1-PB52$ was an invalid test and can be thus disregarded.

Figure 56 shows the tensile strength of each sample calculated using equation 5. The samples are colored by lithology. Grey being shales (category 4), orange being sand (category 1, 2 and 3). The samples indicated by crosses are Brazilian discs taken from the same plug. If these samples are completely intact without any cracks induced by the drilling or sawing of the samples, one can expect similar results. The tensile strength of the two samples are similar, but not very close, which could be due to microcracks or other small sedimentological features.
When looking only at the orange, sand samples, one can see a trend with porosity; the tensile strength is decreasing with increasing porosity. The trend is indicated by the orange arrow. This trend is visible already, but this is not a large number of samples to really prove this trend.

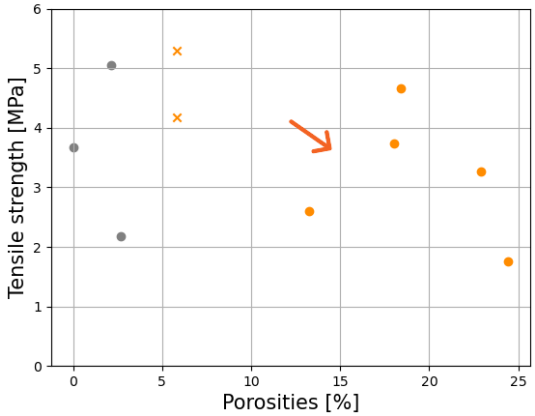

Figure 56: Tensile strength which is calculated from the peak strength and its dimensions per sample plotted vs the porosity. The samples indicated by crosses are two samples from the same plug. The orange arrow is there to highlight the trend within the sand samples.

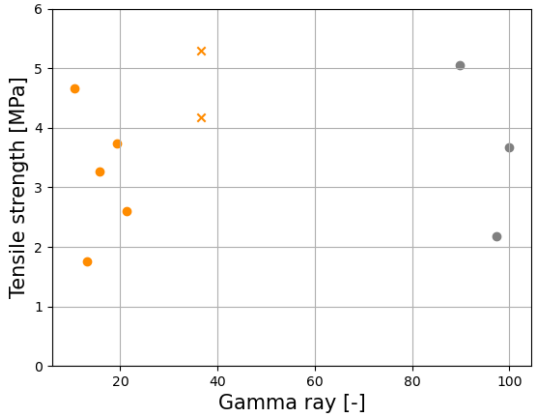

Figure 57: Tensile strength plotted versus the gamma ray of each sample. The samples indicated by crosses and squares are two samples from the same plug. It is not really possible to detect a trend from this data.

3.4 Acoustic Data

During all UCS and triaxial Experiments were acoustic data measured every ten seconds. However, only at eight of the fifteen samples in the UCS test were the acoustic data correctly saved. Unfortunately, in the Triaxial test, no acoustic data were correctly saved.

Every 10 seconds a compressional (P) wave and shear (S) wave was propagated through the pistons and the sample themselves. Every P-wave and S-wave arrival was picked with the use of python. Since the sample undergoes axial strain during the test, the calculation of the speed of the P- and S-wave must be compensated for the shortening of the sample. The travel time of the P-wave ($9\mu s$) and S-wave ($15\mu s$) through the piston was subtracted from the measured arrival time before the velocities were calculated.

Figure 58 shows for two samples the P-wave (in orange) and S-wave (in blue) velocities during the UCS test. In the background is the stress versus time plotted to see at what stage the experiment is. At these plots are spikes and discontinuities visible in the P-wave velocities. This is because it is quite difficult to pick the P-wave velocity consistently. The transducers in the set up are made to send out an S-wave, and as a byproduct a P-wave is sent out. Because of this, the S-wave is much easier to pick because the amplitude is much higher, as seen in Figure 12. Since the P- and S-wave velocities do follow a similar trend, it is best to look at the S-wave velocities for the interpretation of these figures. In each figure, two single points are plotted. These represent the P- and S-wave velocities which were measured statically for each sample. The gray dotted line in the two figures represents the stress on the sample during the test.

The velocity is increasing as the sample can the sample is compressed in Figure 58a. One can see this especially in the P-wave velocity during the linear elastic stress region, which is expected. Unfortunately the data stopped recording before this test was finished due to unknown reasons. Figure 58b shows unexpected results. The velocity did not increase in the linear elastic stress region and when the sample broke the first time (indicated by the stress drop) at t = 220 s, no effect can be seen in the acoustic data. One would expect a velocity drop after the yield point is reached, which is not found here. Due to incomplete data collection during the experiments and the unexpected results, is this method considered as not reliable. It was the first time working with a new acoustic system. Therefore no conclusions will be drawn from the acoustic data in this research.

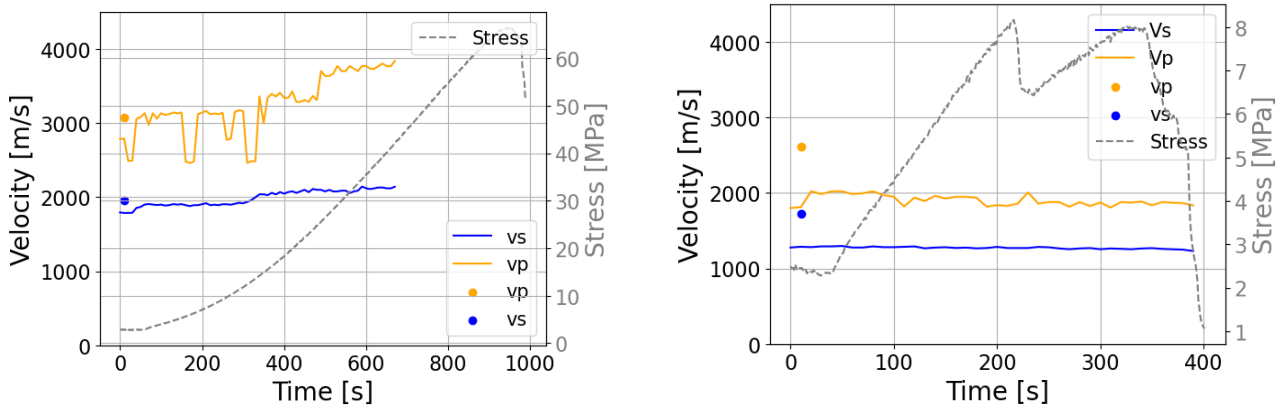

(a) C7-5-PT11

(b) C4-5-PT55

Figure 58: Vp (blue line) and Vs (orange line) during the experiments of two samples. The blue and orange dots are the p-wave and s-wave velocities measured statically before the experiment. The grey dotted line in the background is the stress plotted versus time.

4 Discussion

This chapter discusses the results, it compares the results to other data and discusses the engineering applications.

4.1 UCS discussion

Typically the unconfined compression strength increases as the porosity decreases. Since this trend is not immediately visible from Figure 14a, another parameter must be governing the unconfined compression strength in these samples. The first variable that can be considered is the lithology / mineralogy. It is good to separate the clays from sands, because it is expected that the mineralogy has an influence on the UCS. Within the low gamma ray samples in Figure 14a, there appears to be a negative trend between the UCS and porosity. Yet, this trend is not definitive and should be interpreted with caution, since the range of porosity values is not that big and because there are not enough data points here. Within the sands and shales a difference in minarology could also cause differences in strengths of the samples. No detailed mineralogical study has been done on these samples and therefore this effect could not yet be studied. However, it is recommended to do so to see the effect of different minerals, within each lithology.

Like shown in the results section (59a and 59b) it seems like the finer grained samples, which are usually light grey colored, are stronger than the courser grained samples, which are a bit darker grey. Figure 60 shows a close up picture of the samples $C6-19-PB36$ (left) and $C3-3-PT67$ (Right). $C6-19-PB36$ had an UCS 67 MPa, $C3-3-PT67$ had an UCS of 35 MPa. Sample PT67 on the right is generally more grey, this is because this sample has more black spots. Not because the majority of the actual grains are greyer. All quartz grains have similar color in both samples. It also seems that the sample on the left has some whiter material in between the grains, which could be dolomite cementation. These black spots are expected to be organic material. These pictures also show that PB36 is finer grained than PT67.

Literature shows that there is a negative relationship between the mean grain size and the UCS of sandstones [2], [8]. Yet, grain size alone is seen as a good indication of the unconfined compressive strength of sandstones. No literature study was found which investigated the effect of the amount of organic material in sandstone on the UCS. It is however expected that more organic material will decrease the strength of sandstone, since organic matter is softer than quartz grains.

As explained in the introduction are coarser grained samples expected to be weaker [19]. Samples with more organic material are also expected to be weaker. It can not be concluded that these coarse grain samples, which also have more organic material, are less strong because of the grain size, the organic material or both.

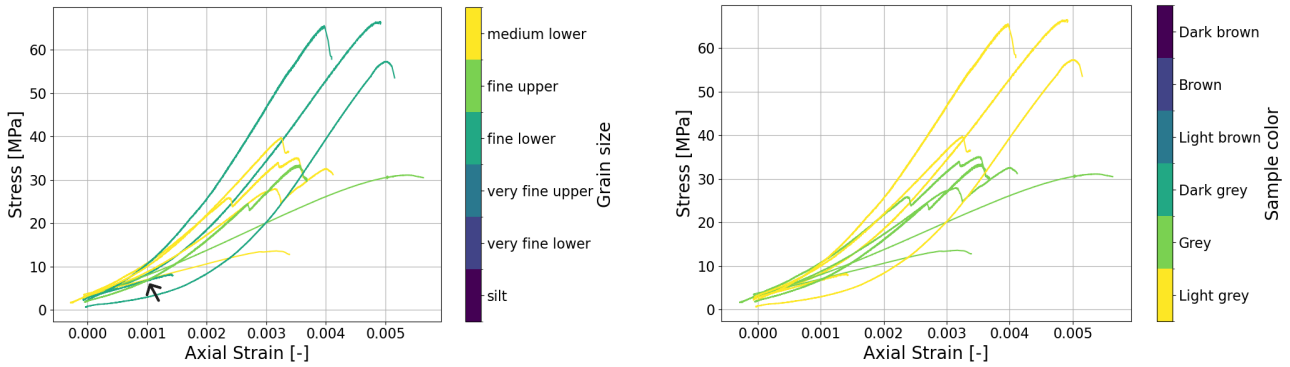

(a) Axial strain of the sandstone samples tested in UCS, colored by grain size.

(b) Stress–strain curves from UCS tests, color-coded by descriptive sample color.

Figure 59: Comparison of sandstone samples based on grain size (left) and sample color (right).

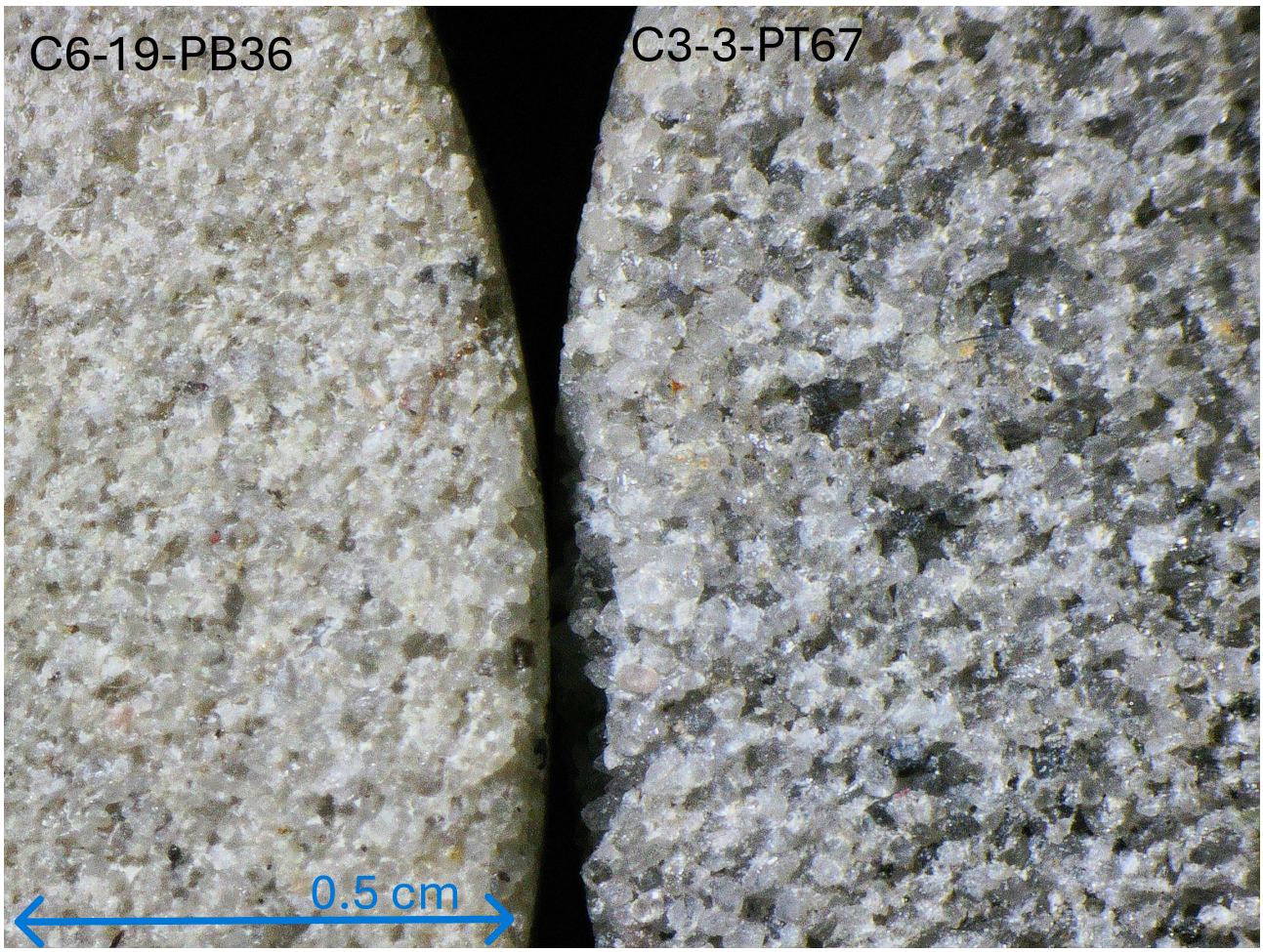

Figure 60: Close up pictures of $C6-19-PB36$ (left) and $C3-3-PT67$ (Right)

Another factor which could control the UCS here are heterogeneities within the samples. To assess this, the internal structure of the samples could be studied, before and after the sample was tested, using the CT-scans that were made. Other diagenetic factors could play a role in governing the strength of each samples. Cementation could strengthen the rock, since it is known to effect the mechanical behavior of sandstone in a triaxial test [21]. A way to investigate this would be to take thin sections of the samples and plot the amount of cement versus the UCS. Pressure dissolution, which is known to be present in the delft sandstone [[1]], could also have an effect on the strength of the samples.

The expectation was that there would have been a correlation between the Young's modulus, yield point and peak strength and porosity for the sand samples, like many other sandstones. This correlation is not visible within this amount of samples which were tested on the UCS test (see Figure 14). It is still expected that this correlation will occur if more samples with a higher variety of porosities are tested. Therefore it is advised to look for sand samples within the Delft Sandstone which have low porosity ($5-16\%$) to test on the UCS test.

4.2 Triaxial

A more clear division between the geomechanical behavior of the sands and shales was present in the data from the triaxial tests compared to the UCS tests. There is a clear division in yield behavior and a clear division in the friction angle between the sands and the shales. There is really no clear division within the stiffness of the samples. An interesting thing to note is that at the lowest confining pressure, the shales showed the most inelastic strain, which can be seen in Figure 41. However, the total strain (which is a combination of elastic and inelastic strain) before the samples broke is larger for the sand samples.

No matter what the outcome of these triaxial tests would have been, it would not have been possible to identify a clear trend with porosity, due to the limited and uneven distribution of porosity values among the tested samples. Four of the tested samples had a porosity of approximately 20%, one had a porosity of 12%, and the shale samples all had porosities below 2.5%. Even if there was a perfect correlation between porosity and yield behavior, it would be difficult to observe, as porosity values are nearly uniform within both the sand and shale

groups. If a more definitive trend with porosity is desired, additional samples should be tested. Nonetheless, the current dataset already offers valuable insight: the sand samples show a low variability in yield point at high confining pressures. At 5 MPa confing pressure there is 30 MPa range in yield point, at a confining pressure of 30, there is a range of 15 MPa in the yield point. This effect is clearly visible when the yield point data per confining pressure is plotted for the sands and shales separately using box plots (see Figure 61).

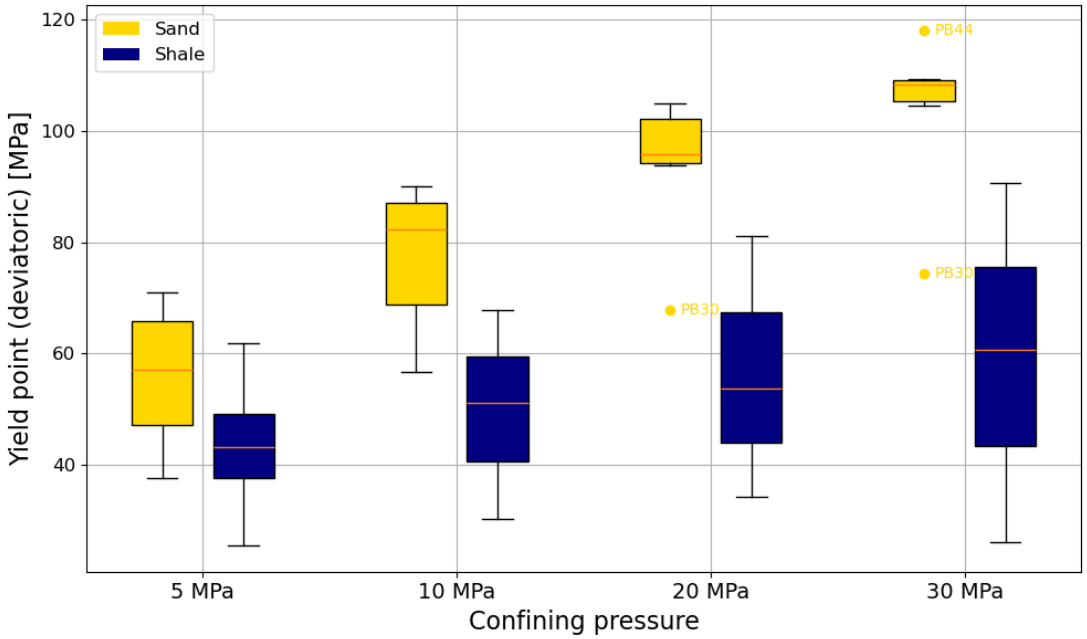

Figure 61: Box plots of the yield points per confining pressure. This really shows the effect that the spread in yield point decreases for the sands at higher confining pressures.

In subsection 3.1 it was found that the finer grained samples had a higher unconfined compressional strength. It is interesting to note that in subsection 3.2 it was found that the finer grained samples had a lower Young's modulus.
It is expected generally that samples with a high UCS have a high Young's modulus. This is also observed from the data of the UCS tests in Figure 17. Therefore, it is expected that the samples with finer grains, which are found to be stronger in the UCS test, also have a higher Young's modulus in the triaxial test. However, these observations indicate otherwise.

This formation in the subsurface is saturated with reservoir brine. Therefore, to simulate the reservoir conditions as good as possible should the samples be saturated. It should be noted that the sand samples which were tested were saturated with brine and the shales were tested dry. Ideally the shales would have been tested saturated as well, however the samples broke when they were saturated, therefore they were tested dry. Other experimental evidence shows that the effect of saturation is more pronounced under high confining pressure. The sandstones which are saturated usually have a lower cohesion value, friction angle and Young's modulus [12]. This should be taken into account when comparing the sands to the shales.

4.3 Static verus Dynamic Young's Modulus

The dynamic Young's modulus is calculated as follows [16]:

$$E = \frac{\rho v_s^2 (3v_p^2 - 4v_s^2)}{v_p^2 - v_s^2} [Pa] \tag{9}$$

The dynamic Young's modulus is first calculated with the v_p, v_s and ρ, which were measured in the lab. The dynamic Young's modulus is plotted versus the static Young's modulus (see Figure 62). On the x-axis is the dynamic Young's modulus, on the y-axis is the static Young's modulus. The samples are colored by their gamma ray. Within the sand samples, a clear trend is visible. An increasing dynamic Young's modulus means an increasing static Young's modulus. The grey dotted line represents the ideal relationship, any point on that line has the same dynamic as static Young's modulus. It is plotted here as a reference to compare the samples. Within the sand samples (low gamma ray), a clear trend is visible, which is quite close to the ideal line. The

red line is fitted to all data points with a gamma ray lower than 40 API (the sands), using a linear least-squares regression. The fit created by this regression is as follows.

$$E_{static} = 0.968 * E_{dynamic} - 4.296 \tag{10}$$

This fit is moderately good, it has an R^2 of 0.51.

In general, for the sand samples, the dynamic Young's modulus seems to overestimate the static Young's modulus a bit. The shale samples (high gamma ray) show no real correlation between the static and dynamic Young's modulus. They are also quite far away from the ideal line. The dynamic Young's modulus is overestimates the static Young's modulus a lot for the shales.

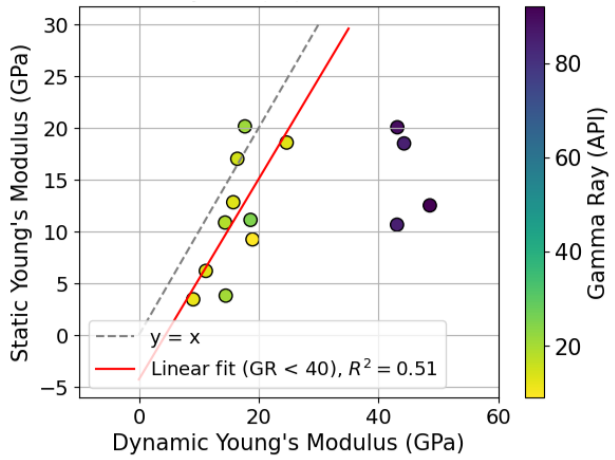

Figure 62: Dynamic Young's modulus calculated from measurements in the **lab** plotted versus the static Young's modulus, colored by gamma ray. The blue line represents the ideal relation between the static and dynamic Young's modulus. For any value on that line, the dynamic Young's modulus is equal to the static Young's modulus. It is plotted here as a reference.

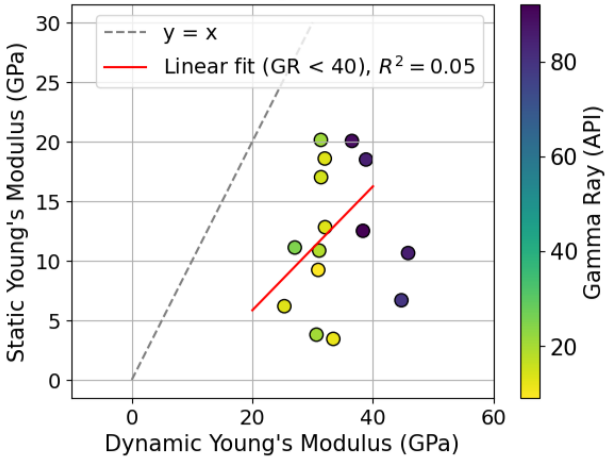

Figure 63: Dynamic Young's modulus calculated from measurements from the **logs** plotted versus the static Young's modulus, colored by gamma ray. The blue line represents the ideal relation between the static and dynamic Young's modulus. For any value on that line, the dynamic Young's modulus is equal to the static Young's modulus. It is plotted here as a reference.

To be able to answer one of the research questions: "How can the constitutive behavior be linked to the well-log data of the injection and production well?", the static Young's modulus must be compared with the dynamic Young's modulus calculated from the v_p, v_s and ρ measured in the logs. The results are plotted in Figure 63. The red line is fitted to all data points with a gamma ray lower than 40 API (the sands), using a linear least-squares regression, just like in Figure 62. No correlation can be found between the dynamic and static Young's modulus.

Now the question arises why the static Young's modulus can be moderately good correlated to the dynamic Young's modulus, attained by measurements in the lab, for the samples with a low gamma ray, while no good correlation can be found for the same sands, using the dynamic Young's modulus calculated from the logs.

When the velocity and density measurements on the samples are plotted versus the v_p, v_s and ρ measurements from the logs, Figure 64 is attained. Figure 64 shows the velocity and density measurements where the lab measurements are on the x-axes and the log measurements are on the y-axes. The first column (figures a, c and e) show all the samples, the second column (figures b, d and f) show only the sand samples. Especially for the P-wave velocity and the density, there is quite a good correlation between the lab and the log measurements for all samples, compared to just the sands. Because of these differences in measurements from the lab and from the logs, there is a difference in the dynamic Young's modulus calculated from the lab and from the log.

There is a good correlation between the static and dynamic Young's modulus calculated from the lab measurements. However, there is a bad correlation between the static and dynamic Young's modulus calculated from the log measurements. Therefore, to still be able to predict the static Young's modulus from the log data, the log data was converted to lab data. From this synthetic lab data will the dynamic Young's modulus be calculated, which will be plotted versus the static Young's modulus. Between these two variables a relationship will be found, which can be used to calculate the static Young's modulus from the log data.

Since this model tries to predict the static Young's modulus for only sand samples, the relation between log and lab data must be taken only from the sand samples. That is why to convert the log data into synthetic lab data are the following relationships found from the linear lines in Figure 64b, Figure 64d and Figure 64f. The following relations are attained:

$$v_s(lab) = 5.073 * v_s(log) - 10108.344[m/s] \tag{11}$$

$$v_p(lab) = 4.855 * v_p(log) - 16748.377[m/s] \tag{12}$$

$$\rho(lab) = 3.375 * \rho(log) - 5.761[g/cm^3] \tag{13}$$

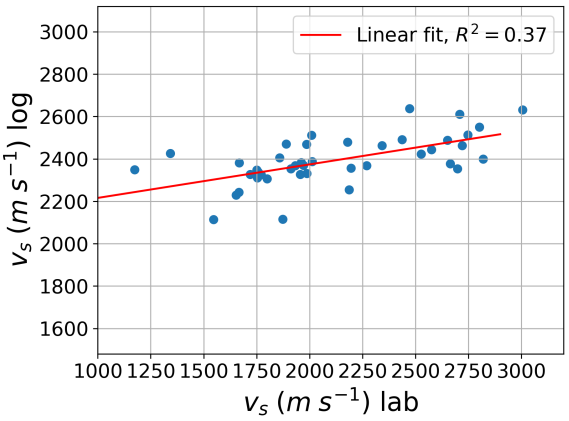

(a) S-wave velocity measured in the lab on the x-axis, from the on the y-axis. For all samples.

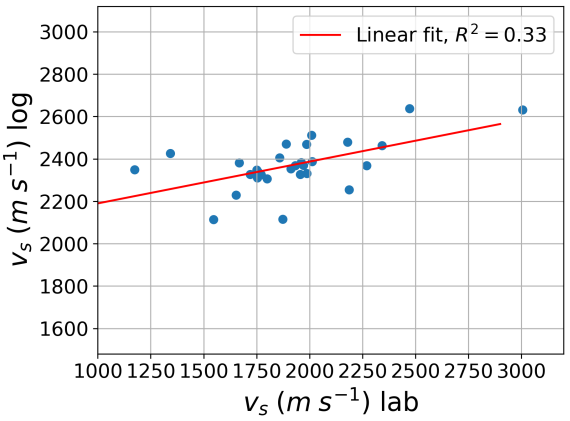

(b) S-wave velocity measured in the lab on the x-axis, from the on the y-axis. For only the sands.

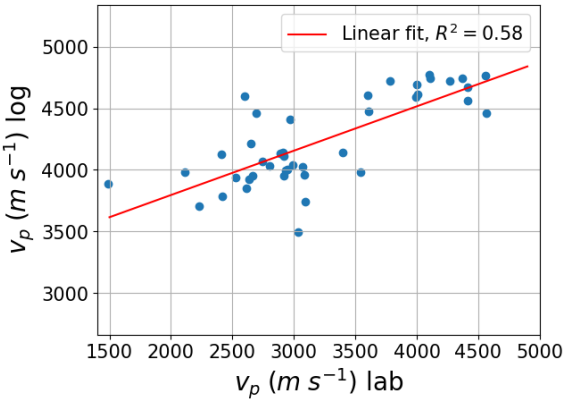

(c) P-wave velocity measured in the lab on the x-axis, from the on the y-axis. For all samples.

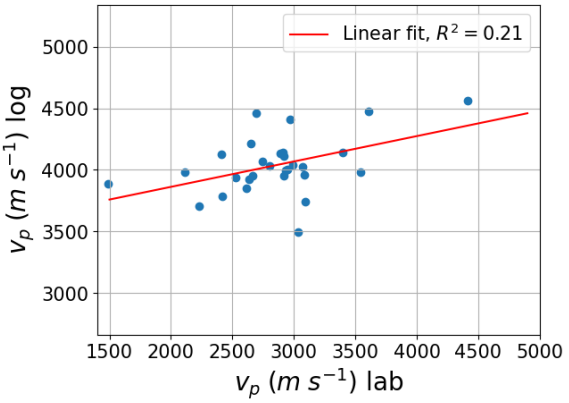

(d) P-wave velocity measured in the lab on the x-axis, from the on the y-axis. For only the sands.

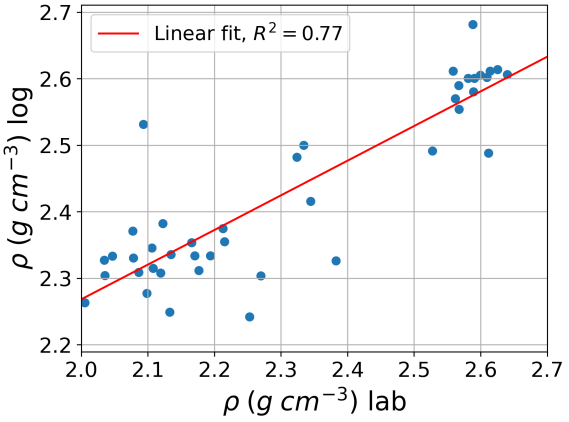

(e) Density measured in the lab on the x-axis, from the on the y-axis. For all samples.

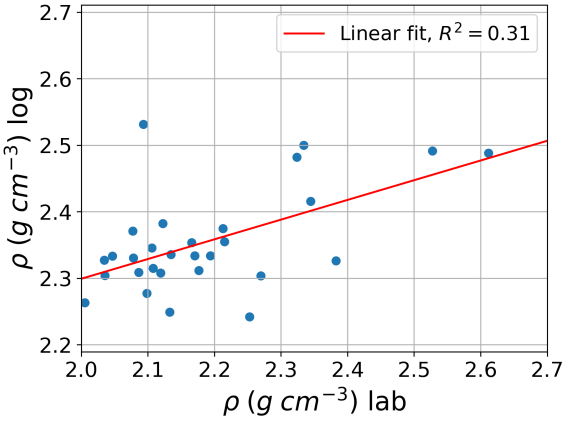

(f) Density measured in the lab on the x-axis, from the on the y-axis. For only the sands

Figure 64: Lab measurements of the P- and S-wave velocities and density versus the measurements from the log. The first column shows the measurements of all samples, the second column shows the measurements of only the sands.

When in turn these synthetically lab generated lab data are used to calculate the dynamic Young's modulus and plotted against the static Young's modulus, the following result is obtained:

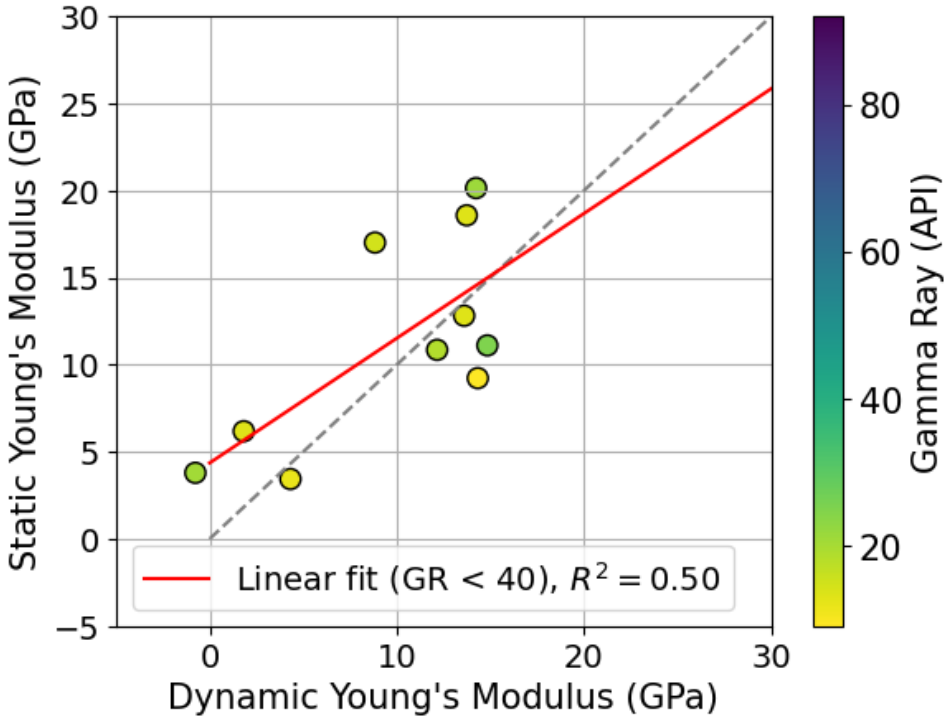

Figure 65: Dynamic Young's modulus calculated from the synthetic lab data, plotted versus the static Young's modulus.

The relation between the dynamic Young's modulus (calculated using the synthetic v_p, v_s and ρ data) and the static Young's modulus is as follows:

$$E_{static} = 0.716 * E_{dynamic} + 4.357 \tag{14}$$

The R^2 from for this linear fit is 0.50, which is moderately good. For the relatively high Young's moduli, the dynamic Young's modulus really overestimates the Young's modulus, which should be taken into account. To make this fit and thus this model better, more sand samples should be tested on the UCS machine, to get the static Young's modulus. Also, to improve this model, the discrepancy between the log data and the lab data must be reduced. If the log data would give exactly the same data as the lab data, this fit would be a lot better, and the conversion of log to lab data would not be necessary. This would reduce the error.

When converting the log data to lab data an erros is introduced. When this synthetic lab data are then used to calculate the dynamic Young's modulus on which a line is fitted, another error is introduced, because this fit is also not perfect.

The relationship almost as good as the relationship found between the static and dynamic Young's modulus calculated from the actual lab data. They have a similar R^2.

All these mathematical steps could be put in one equation, however this equation would become very long and thus prone to errors. Therefore a step by step succession is given to be able to use this model:

1. Convert the velocity log data to m/s and density log data to g/cm^3.
2. Convert this to lab data using Equation 11, Equation 12 and Equation 13.
3. Calculate from that the dynamic Young's modulus using Equation 9
4. Convert that dynamic Young's modulus to the static Young's modulus with Equation 14

A common way to evaluate the performance of a statistical model is to divide the dataset into a training set, a validation set, and a test set. These datasets will then be used to fit the model, to tune the model and to test the model, respectively. However, in this case, the model was based on only ten data points — a very limited sample size, especially when split into separate subsets.
An alternative technique that is more suitable for small datasets is Leave-One-Out Cross-Validation (LOOCV),

where the model is trained on all but one data point and validated on the remaining point. This technique generated ten slightly different models. Each model was made without one data point. The data point which was left out was then used to validate the model. The error between the model and the data point was calculated for each model. An example of one of the models is shown in Figure 66. The model uses the nine data points from the sand samples, on this was the linear model fitted. Then the difference between the excluded data point and the linear line is the error, which is visualized by the black dotted line.

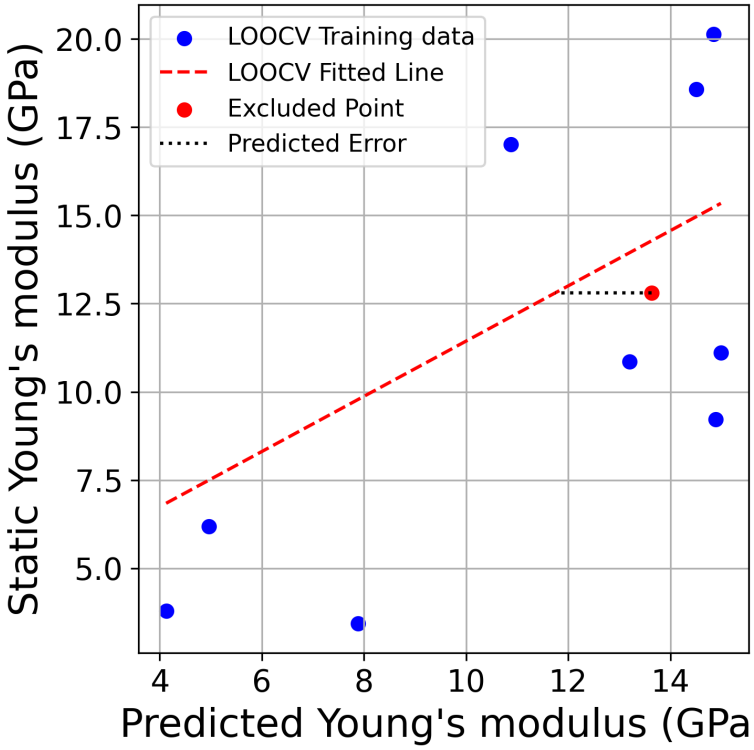

Figure 66: One of the models predicting the static Young's modulus using the LOOCV technique. The red dotted line is the linear eventual model. The predicted error for the excluded datapoint is given by the dotted black line.

The errors are shown in a histogram in Figure 67. The errors shown in the The average absolute error this model created was 2.6 GPa. The average absolute error of the model was 2.6 GPa, while the average measured static Young's modulus was 11.3 GPa, with a standard deviation of 5.6 GPa. These results suggest that the model performs reasonably well in predicting static Young's modulus based only on log data. To reduce the error of the model further, more samples need to be tested using the UCS test. With an expanded dataset, the model can be trained more robustly and potentially achieve greater accuracy.

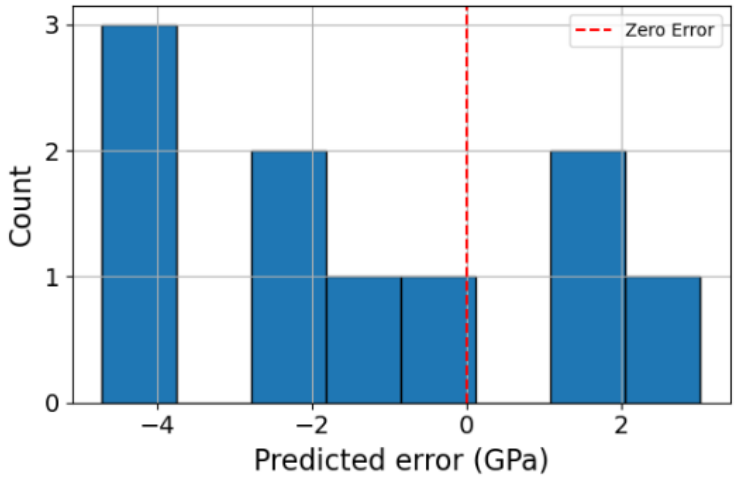

Figure 67: Predicted errors from the statistical model displayed by a histogram.

Figure 68 shows the well log of DEL-GT-01. The samples tested on the UCS test are shown at their corresponding depths. vp_{lab}, vs_{lab}, and rho_{lab} represent the P-wave velocity, S-wave velocity, and density, respectively, calculated using the relationships between laboratory and log measurements (Equation 12, Equation 11, Equation 13). The adjacent column shows the Young's modulus measured in the lab (black bars). The "Theoretical Static E" shows the Young's modulus calculated according with the method described above. This is only calculated for part of the log where the gamma ray is lower than 40 API, since this method is only applicable there. The measured Young's modulus fits the theoretically calculated Young's modulus reasonably well, which is expected from Figure 65 which has an R^2 of 0.50. In the end this model is thus reasonably good in predicting the static Young's modulus of the Upper Delft Sandstone Member using only log data. If the geomechanical behavior of the Delft Sandstone is laterally homogeneous, is this method possible to predict the static Young's modulus of sand parts of the Delft Sandstone at other locations than DEL-GT-01.

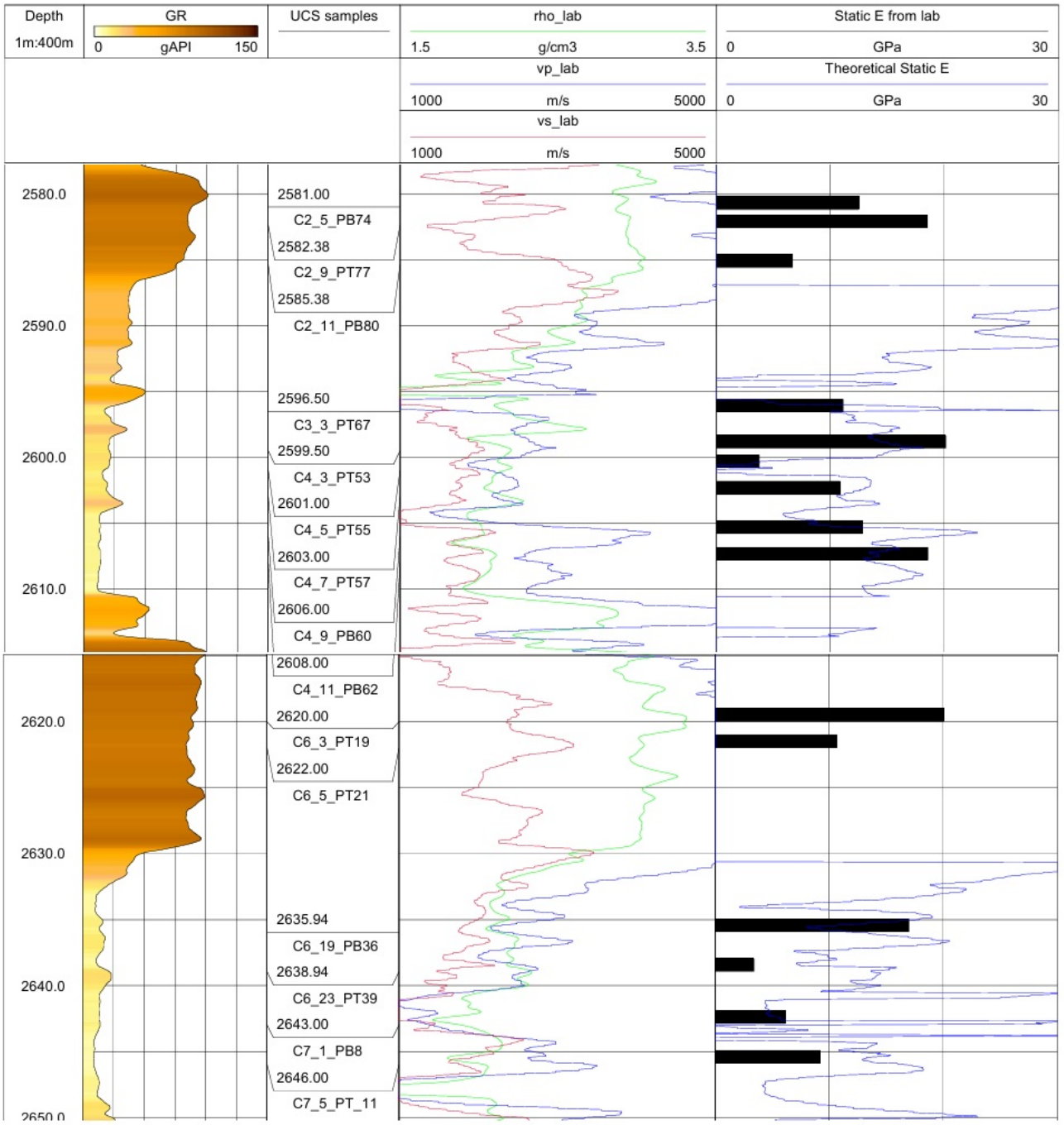

Figure 68: Well log of DEL-GT-01 The samples tested on the UCS test are shown at their corresponding depths. vp_{lab}, vs_{lab}, and rho_{lab} represent the P-wave velocity, S-wave velocity, and density, respectively, calculated using the relationships between laboratory and log measurements (Equation 12, Equation 11, Equation 13). The adjacent column shows the Young's modulus measured in the lab (black bars). Where shown, the log-derived "Theoretical Static E" represents the static Young's modulus calculated according to the methods described in this section.

4.4 Static verus Dynamic Poisson's ratio

The dynamic Poisson's ratio is calculated as follows [16]:

$$\nu = \frac{v_p^2 - 2v_s^2}{2(v_p^2 - v_s^2)}[-] \tag{15}$$

The dynamic Poisson's ratios calculated from the acoustic lab data are plotted versus the static Poisson's ratio, which is attained from the UCS experiments, in Figure 69. It is colored by the gamma ray. The majority of the samples is around the dotted line, which indicates equal dynamic and static Poisson's ratios. For four samples,

the dynamic Poisson's ratio is underestimated compared to the static Poisson's ratio, which is not correlatable with the gamma ray.

Figure 70 shows the dynamic Poisson ratio calculated from the sonic log data, it is plotted versus the static Poisson's ratio which was calculated from the UCS tests. One can note similar results as in Figure 69, except that the majority of the samples has a higher dynamic Young's modulus in this case. This is due to the difference in P- and S-wave velocities between the lab and log data, as discussed in subsection 4.3. A method like discussed in subsection 4.3 to convert the lab data to log data, could be used here as well. Yet, since the original comparison between dynamic (from the lab data) and static Poisson ratio is not that good, this method is not applied.

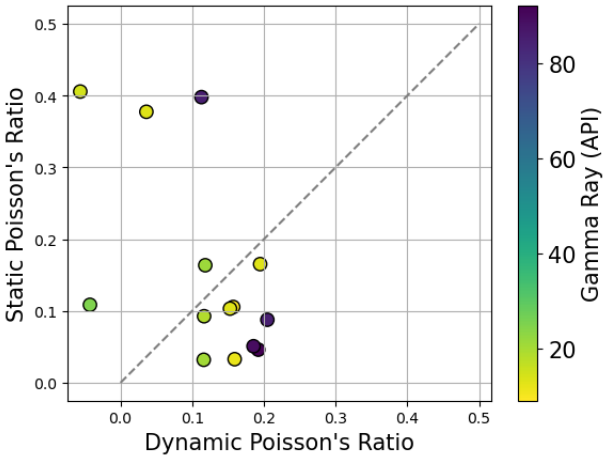

Figure 69: Dynamic Poisson ratio calculated from the **lab** data, plotted versus the static Poisson ratio, colored by gamma ray. The grey dotted line respresents the ideal relation between the static and dynamic Poisson ratio. For any value on that line, the dynamic Poisson ratio is equal to the static Young's modulus. It is plotted here as a reference.

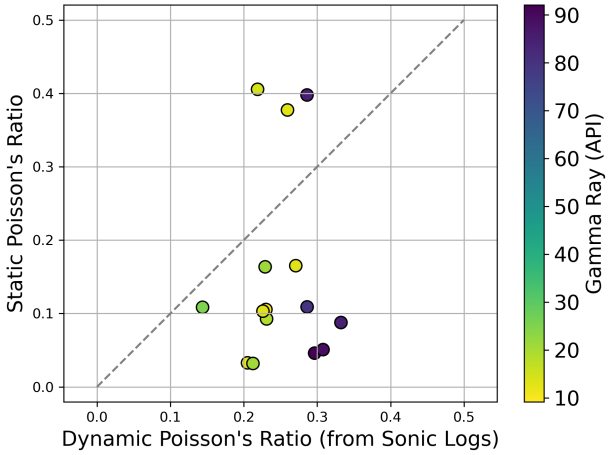

Figure 70: Dynamic Poisson ratio caluclated from the **logs**, plotted versus the static Poisson ratio, colored by gamma ray. The grey dotted line respresents the ideal relation between the static and dynamic Poisson ratio. For any value on that line, the dynamic Poisson ratio is equal to the static Young's modulus. It is plotted here as a reference.

4.5 Comparison to other data

Only two other samples of the "Delft Sandstone" were ever tested before this research. Vincent Soustelle et al [20] tested two samples from the Delft Sandstone / IJsselmonde formation. The authors state this sandstone is the Delft Sandstone but it is more likely that it is actually the IJsselmonde Sandstone. The IJsselmonde Sandstone is comparable with the Delft Sandstone. The IJsselmonde formation has been deposited around the same time, in the same basin and has the same burial depth history as the Delft Sandstone. The IJsselmonde is deposited in a more shallow marine environment, indicated by the marine shells present. Since this is the most comparable geomechanical research available, the data from this research will be compared to it. Vincent Soustelle et al. tested two samples on a triaxial test at different temperatures. This triaxial test was also able to measure the radial deformation and thus it was also possible to measure the Poisson ratio. Only the samples closest to room temperature from the authors research are comparable to the samples tested in this research. The results of the autors are shown in Figure 71. The dark blue dots in Figure 71 are the samples which were tested at similar temperatures as the samples in this research.

The Young's modulus at their lowest confining pressure of 1 MPa ranged between 2.4 and 5.4 GPa. This is quite a bit lower than the Young's modulus which was measured in this research. The samples tested at the lowest confining pressure were tested at 0.5 MPa, which is closest to their 1 MPa. This sand sample had a Young's modulus of 16 GPa. At their highest confining pressure of 20 MPa the Young's moduslus ranged between 11 and 13.5 GPa. While the sand samples which were tested for this research ranged between 23 and 35 GPa at 20 MPa confining pressure.

Figure 71 also shows similar convex behavior of the Young's modulus with increasing confing pressure as found in this research, which can be seen in Figure 72.

Vincent Soustelle et al. also measured the Poisson ratio at different confining pressures (see Figure 71). However, they are not directly comparable, because to the Poisson ratios of this research. Due to the fact that the Poisson ratios of this research are measured without a confining pressure. This confining pressure is expected to influence

the Poisson ratio a lot.

The data of this research are not directly comparable to [20], because it is likely a slightly different formation, and the tests were performed slightly different. Nevertheless, they represent the most comparable dataset available for this study.

The reason Young's moduli are quite a bit lower in [20] could be because they tested samples that have a porosity which is quite a lot higher than the samples tested in this research. Another reason could be that the IJsselmonde formation is younger than the Delft Sandstone. It is also buried less deep, 1.6 km compared to the Delft's 2.2 km. This could mean there is less pressure dissolution and thus that the samples are less stiff. It is likely that it is a combination of both factors.

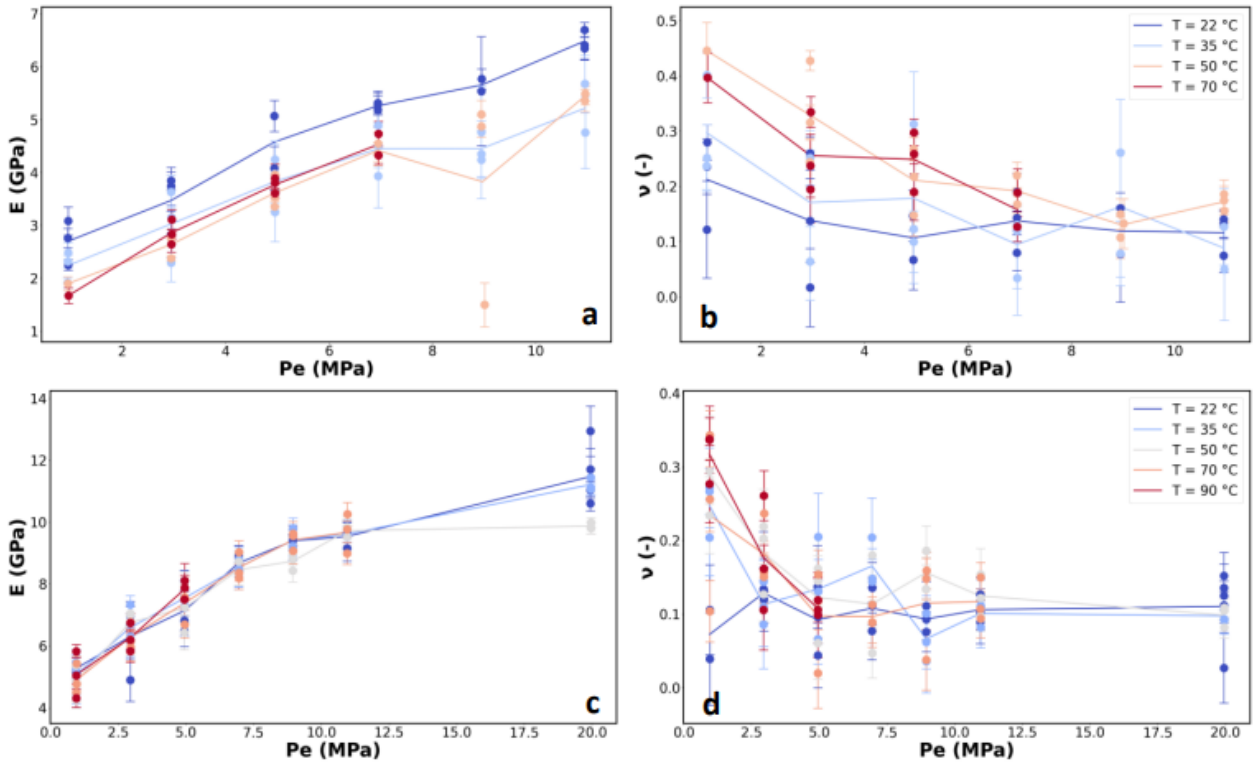

Figure 71: Result from the geomechanical test of the IJsselmonode formation, [20].

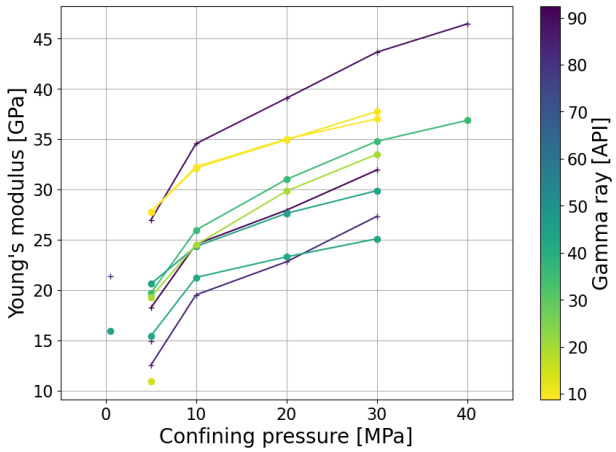

Figure 72: Young's modulus versus confining pressure, colored by gamma ray.

Wadsworth [25] used a database containing UCS data for different types of sandstones, these data were publicly available. The red dots represent the unconfined compressive strength of the Delft Sandstone, that was measured for this research. One can see that the UCS of the Delft Sandstone is in the same area as the other data

points. The Delft sandstone, according to the Geological Society Group Working Party [22], is considered to be moderately weak to strong, ranging from 8.2 MPa to 66.5 MPa unconfined compression strength. Figure 79 shows all the strength catagories.

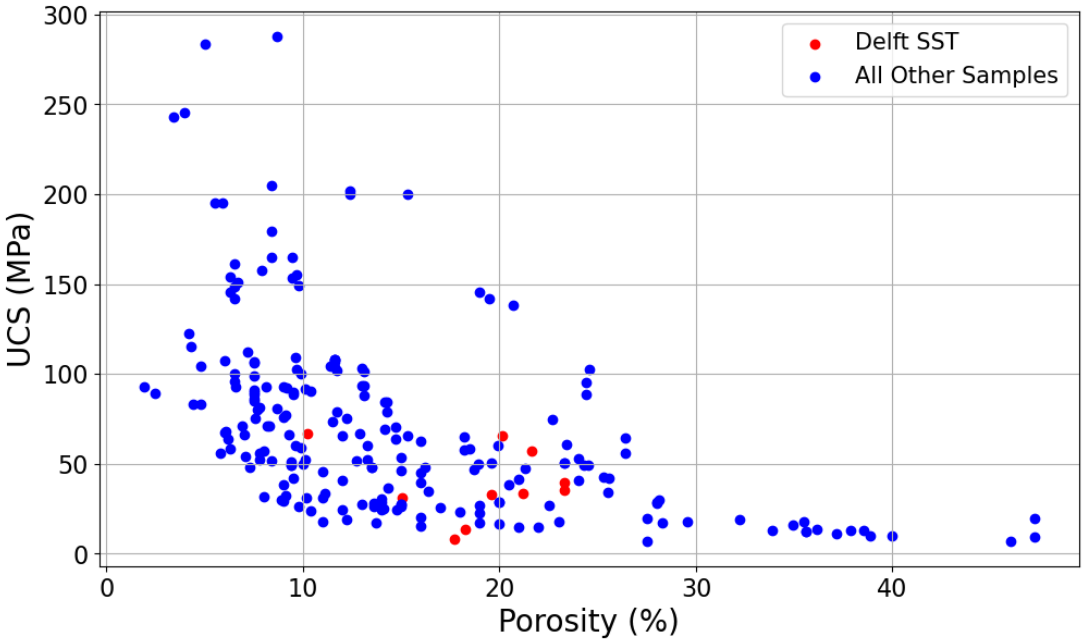

Figure 73: UCS of Delft Sandstone compared to UCS values of other sandstones [25]

4.6 Impact and Outlook

Since the Delft Sandstone becomes more and more targeted for geothermal energy, it is good that insights are generated about the geomechanical behavior of this formation. If now models need to be made to predict for example induced seismicity, the ranges of static moduli which have been measured in this research can be used. If it is desired to predict really well what exactly the static moduli at places are in the reservoir, more samples need to be tested and better trends need to be found. Now that there is a foundation for the geomechanics of the Delft sandstone, it would be a good option to also test the geomechanical behavior of the Rodenrijs Claystone to be able to predict the maximum injection pressure that can be used when reinjecting the reservoir brine during operations.

To see which results of this research can be best compared to the in situ Delft Sandstone in the subsurface can the horizontal stress calculated. The horizontal stress in the subsurface can be roughly estimated by the following relation:

$$S_{horizontal} = \frac{\nu}{1-\nu} * S_{vertical} \tag{16}$$

Where ν is the Poisson ratio of the formation and $S_{vertical}$ is the vertical stress which can be approximated by $\rho * g * TVD$, where rho is the bulk density of the overlying formation, g is the gravitational constant and TVD is the true vertical depth. If this is calculated for the Delft sandstone formation at the targeted depth and using a Poisson ratio of 0.1 (average Poisson ratio from the results of the UCS test, without the outliers), the horizontal stress becomes $\approx$ 7 MPa. Using this calculation, the vertical stress is roughly 53 MPa. When this is compared to Figure 14d, one can see that the at a confining pressure of 7 MPa, the lowest yield point is 30 MPa, which is lower than the vertical stress. Which could mean that because of the vertical stress in the reservoir, some of the weak in situ sediments are already yielding. However, most samples seem to yield at a higher vertical stress at a confining pressure of 7 MPa. Therefore, most of the reservoir will be expected to be intact.

Predicting the UCS of the Delft Sandstone in other locations in this well or other wells in the area remains a challenge. This is primarily due to the weak correlation between the UCS and the petrophysical data. Although a relationship between the UCS and the velocity measurements from the lab is present, the correlation with wave velocities from the laboratory and logs is poor, as discussed earlier. Additionally, the UCS showed some correlation with grain size and/or color of the sandstone. However, using this parameter in practice to determine

the UCS while drilling is unreliable, as cuttings in the borehole are often mixed, and grain size and color can change rapidly in the geology, compared to the drilling rate.

This study focused on the Upper Delft Sandstone from which a limited amount of samples was available to test in the laboratory. The samples were cored in a regular interval from the cores. However, due to several reasons, not all samples were still in tact by the time this geomechanical research was done. For example, some samples already broke during the drilling of the sample from the core, some samples were damaged during transport or during cleaning or some samples were not long enough to test on the UCS or triaxial test. Because of these reasons there was a limitation in how each test had a representable set of samples of the Upper Delft Sandstone. If one looks for example in Figure 3 where the samples are listed in the well log on which test they were tested. One can see that no sample in the interval of 2595 and 2610 m was tested on the triaxial test, because there were not enough samples available in this depth range. In the same way there are samples missing on certain depth intervals in the UCS and Brazilian disc tests. This had a limitation on this research.

The question also arises how well these 39 samples captured the essence of the upper Delft Sandstone Member. It is likely that the number of plugs was insufficient to fully capture the formation's heterogeneity. There are most likely heterogeneities which influence the geomechanical behavior of this formation on a bigger scale than these plugs. Therefore, the sizes of the samples probably do not represent the Representative Elemantary Volume (REV).

Since it is desired to test more samples with a medium porosity and since low porosity zones are more localized than the resolution of the porosity log, an idea is to take samples of the cores that have been slabbed. In this way the cores can first be visually inspected, and low porosity zones might be identified. From these zones cores could be taken and tested geomechanically. Nevertheless, there is much more core available from which many more samples can be drilled. It is highly recommended to do so to make the dataset generated by this master thesis more complete.

5 Conclusion

This was the first extensive geomechanical research on the Delft Sandstone Member, which thereby made a contribution to scientific geothermal research in The Netherlands. The goal was to quantify the geomechanical behavior of the upper Delft Sandstone Member, and to see how heterogeneous this behavior is. The main research question was as follows:

For the purpose of geothermal energy extraction: what is the constitutive behavior and what are the static moduli of the upper Delft Sandstone?

The answer to this question can be characterized by the following points:

- The upper Delft Sandstone Member based on the samples which were tested can be classified as moderately weak to strong.
- The Young's modulus found in this research using the UCS test of the upper Delft Sandstone Member ranged from 3 to 20.1 GPa. The Poisson ratio clusters between 0.04 and 0.16 and has some high outliers.
- There was a good correlation between the strength parameters from the UCS test: a sample with a higher UCS has a higher yield point and a higher Young's modulus.
- The Young's modulus of the Delft Sandstone Member was compared to that of the IJsselmonde formation, which is a similar formation. The Young's modulus of the Delft sandstone Member is higher than that of the IJsselmonde formation. This could be due to the high porosity and shallower burial depth of the IJsselmonde formation.
- The Yield points found in every stress step in the triaxial test are predictable for the sandstones, especially at higher confining pressure the shales show a lot of spread. No correlation was found between the Young's modulus from the triaxial tests and any petrophysical property. It would have been nearly impossible to find a correlation with any results of the triaxial test and the porosity of the samples. The cause of this is the uneven distribution of porosity values among the tested samples.
- The peak stress experienced on the samples in the triaxial test for the sands was significantly higher than that for the shales. Additionally, the sandstones exhibited less variability in peak stress. This indicates a more predictable mechanical response under confining pressure for the sands compared to the shales. However, the range of porosities of the tested sandstones was limited. Therefore it remains uncertain if this statement is true for sand samples with a lower porosity.
- The friction angle of the sand samples was significantly higher than that of the shale samples. The cohesion values were similar.
- Within the sand samples there is a trend visible between the tensile strength of the samples and the porosity: if the porosity increases, the tensile strength decreases. No correlation was found with the tensile strength for the shale samples, due to the limited amount of shale samples tested on the BDT.
- The sands and shales have a similar range in strength in an unconfined environment. Under confining stress, the sands are stronger than the shales.

What correlations exist between the petrophysical and geomechanical properties of the Upper Delft Sandstone Member?

- The expected link with the UCS of sandstones and porosity was not immediately visible. When comparing the UCS of the upper Delft Sandstone with that of other sandstones, one can see that the UCS of the upper Delft Sandstone follows the general trend with porosity but that on it's own this trend is not visible. Therefore the correlation with UCS and porosity is not denied, nor confirmed by this research. It is expected that this link with porosity is actually there, but that the amount of samples tested is not enough to see this link. Therefore it is advised to test more samples with a medium porosity to make a correlation visible.
- There was however a link between the UCS and the wave velocities of the sand samples. The faster the P- and S-waves traveled through the samples, the stronger the sample. This was not observed for the shales.
- It is apparent now that it is not that easy to link these samples of the upper Delft Sandstone to petrophysical properties. This could be partly due to lack of data, and maybe party due to non-existent correlations.

Are there sedimentological features that contribute to the heterogeneity in the constitutive behavior of the upper Delft Sandstone Member and how?

- The grain size or the color of the sand samples showed a correlation with strength. The coarser grained samples, which were more gray due to black grains (expected to be organic material), were weaker. It is not certain whether they are weaker because of the coarser grains, the organic material or both.
- A good other recommendation is to test the mineralogy of the samples that were tested and to take thin sections to see the effect of cementation. This would be good to potentially link these parameters to the strength of the samples.
- One sample showed that lignite pieces which are present in the Delft Sandstone Member form weak spots within the samples, since that sample broke along this piece of lignite.
- It was not possible to link the presence of laminations to the strength of the sample. No other links with sedimentological features were found.

To what extent can predictions of the static elastic moduli be made in the well logs?

- If the dynamic Young's modulus is calculated with the lab measurements, there is a good link between the dynamic and static Young's modulus for the sand samples. When the dynamic Young's modulus is calculated using the log data, no correlation is observed. This is because there is a bad correlation between the log data and the lab data. The log data can be converted to synthetic lab data, which can be used to predict the static Young's modulus in the well log. This model has an R^2 of 0.50, which is reasonably good. The quantification of the error of this model was done using a Leave-One-Out Cross-Validation which showed an average absolute error of 2.6 GPa. This is reasonably good. More samples should be tested on the UCS test to reduce the uncertainty of this model. This model is thus reasonably good in predicting the static Young's modulus of the Upper Delft Sandstone Member using only log data.

This study shows the importance of extensive geomechanical data collection since the geomechanical behavior is not that easily explained. All heterogneities should be captured in order to have a full idea of the geomechancial behavior of such a formation. If in the future models need to be made to predict for example induced seismicity, the ranges of static moduli which have been measured in this research can be used. A reasonably well prediction of the static Young's modulus, using only log data can now also be used. Now that a foundation for the geomechanics of the Delft Sandstone Member has been established, it would be a good option to also test the geomechanical behavior of the Rodenrijs Claystone. This enables us to predict the maximum injection pressure that can be used when reinjecting the reservoir brine during operations.

]

References

[1] Ibrahim Abdulkarim. “Initial description of the sandstone petrography of the Delft Sandstone Member in the DEL-GT-01 well”. Bachelor’s thesis. The Netherlands: Delft University of Technology, 2025.

[2] Hadi Atapour and Ali Mortazavi. “The influence of mean grain size on unconfined compressive strength of weakly consolidated reservoir sandstones”. In: *Journal of Petroleum Science and Engineering* 171 (2018), pp. 63–70. ISSN: 0920-4105. DOI: https://doi.org/10.1016/j.petrol.2018.07.029. URL: https://www.sciencedirect.com/science/article/pii/S0920410518306041.

[3] Juliette Kristin Bruining. “Sedimentological analysis of the well-logs, cores, plugs, and sidewall cores of the DEL-GT wells”. MA thesis. Delft, the Netherlands: Delft Univeristy of Technology, 2024.

[4] Loes Buijze et al. *Review of induced seismicity in geothermal systems worldwide and implications for geothermal systems in the Netherlands*. 2020. DOI: 10.1017/njg.2019.6.

[5] Chandong Chang, Mark D. Zoback, and Abbas Khaksar. “Empirical relations between rock strength and physical properties in sedimentary rocks”. In: *Journal of Petroleum Science and Engineering* 51.3 (2006), pp. 223–237. ISSN: 0920-4105. DOI: https://doi.org/10.1016/j.petrol.2006.01.003. URL: https://www.sciencedirect.com/science/article/pii/S0920410506000167.

[6] PSB Colback. “An analysis of brittle fracture initiation and propagation in the Brazilian test”. In: *1st ISRM Congress*. OnePetro. 1966.

[7] D G Den and Hartog Jager. *Fluviomarine sequences in the Lower Cretaceous of the West Netherlands Basin: correlation and seismic expression*. 1996.

[8] Erik Eberhardt, B. Stimpson, and D. Stead. “Effects of grain size on the initiation and propagation thresholds of stress-induced brittle fractures”. In: *Rock Mechanics and Rock Engineering* 32.2 (1999). Cited by: 359, pp. 81–99. DOI: 10.1007/s006030050026. URL: https://www.scopus.com/inward/record.uri?eid=2-s2.0-0033249208&doi=10.1007%2fs006030050026&partnerID=40&md5=50b6f16cf2772c9f67d4e2da928b2835.

[9] van Esser et al. “End-of-Well Science Programme Report DEL-GT-01 and DEL-GT-02”. In: (). DOI: 10.4233/uuid:6ce07471-6986-434e-aa24-ad6e1f6714d9. URL: https://doi.org/10.4233/uuid:6ce07471-6986-434e-aa24-ad6e1f6714d9.

[10] R.W. Zimmerman J.C. Jaeger N.G.W. COOK. *Jaeger Cook Fundamentals of Rock Mechanics, fourth edition*. Blackwell Publishing Ltd, 2007. ISBN: 978-0-632-05759-7.

[11] Diyuan Li and Louis Ngai Yuen Wong. “The Brazilian disc test for rock mechanics applications: Review and new insights”. In: *Rock Mechanics and Rock Engineering* 46 (2 Mar. 2013), pp. 269–287. ISSN: 07232632. DOI: 10.1007/s00603-012-0257-7.

[12] Diyuan Li et al. “Triaxial Loading and Unloading Tests on Dry and Saturated Sandstone Specimens”. In: *Applied Sciences* 9.8 (2019). ISSN: 2076-3417. DOI: 10.3390/app9081689. URL: https://www.mdpi.com/2076-3417/9/8/1689.

[13] Melanie P. Lutz and Robert W. Zimmerman. “The effect of pore shape on the Poisson ratio of porous materials”. In: *Mathematics and Mechanics of Solids* 26.8 (2021), pp. 1191–1203. DOI: 10.1177/10812865211023535. eprint: https://doi.org/10.1177/10812865211023535. URL: https://doi.org/10.1177/10812865211023535.

[14] Hossein Masoumi, James Horne, and Wendy Timms. “Establishing Empirical Relationships for the Effects of Water Content on the Mechanical Behavior of Gosford Sandstone”. In: *Rock Mechanics and Rock Engineering* 50 (May 2017), pp. 1–8. DOI: 10.1007/s00603-017-1243-x.

[15] *Masterplan Aardwarmte in Nederland Een brede basis voor een duurzame warmtevoorziening*. 2018. URL: www.geothermie.nl.

[16] Gary. Mavko, Tapan. Mukerji, and Jack. Dvorkin. *The rock physics handbook : tools for seismic analysis in porous media*. Cambridge University Press, 1998, p. 329. ISBN: 0521620686.

[17] Malcolm Mellor and Ivor Hawkes. “Measurement of tensile strength by diametral compression of discs and annuli”. In: *Engineering Geology* 5.3 (1971), pp. 173–225.

[18] Landbouw en Innovatie Ministerie van Economische Zaken. *Climate policy*. Jan. 2020. URL: https://www.government.nl/topics/climate-change/climate-policy.

[19] Yu Qi et al. "The effect of grain size, porosity and mineralogy on the compressive strength of tight sandstones: A case study from the eastern Ordos Basin, China". In: *Journal of Petroleum Science and Engineering* 208 (2022), p. 109461. ISSN: 0920-4105. DOI: https://doi.org/10.1016/j.petrol.2021.109461. URL: https://www.sciencedirect.com/science/article/pii/S0920410521011049.

[20] Vincent Soustelle et al. *Thermomechanical Parameters of Geothermal Analogue Reservoir Sandstones in the West Netherlands Basin*. Tech. rep. WarmingUP Consortium, 2022. URL: https://www.warmingup.info/documenten/thermomechanical-parameters-of-geothermal.pdf.

[21] A. M. Al-Tahini, C. H. Sondergeld, and C. S. Rai. "The Effect of Cementation on the Mechanical Properties of Sandstones". In: *SPE Reservoir Evaluation Engineering* 9.04 (Aug. 2006), pp. 308–316. ISSN: 1094-6470. DOI: 10.2118/89069-PA. eprint: https://onepetro.org/REE/article-pdf/9/04/308/2567989/spe-89069-pa.pdf. URL: https://doi.org/10.2118/89069-PA.

[22] "The description of rock masses for engineering purposes: Report by the Geological Society Engineering Group Working Party". In: *Quarterly Journal of Engineering Geology and Hydrogeology* 10.4 (Nov. 1977), pp. 355–388. ISSN: 1470-9236. DOI: 10.1144/GSL.QJEG.1977.010.04.01. eprint: https://pubs.geoscienceworld.org/gsl/qjegh/article-pdf/10/4/355/2864618/qjegh_010_004_0355.pdf. URL: https://doi.org/10.1144/GSL.QJEG.1977.010.04.01.

[23] Ergün Tuncay and Nilsun Hasancebi. "The effect of length to diameter ratio of test specimens on the uniaxial compressive strength of rock". In: *Bulletin of Engineering Geology and the Environment* 68 (Nov. 2009), pp. 491–497. DOI: 10.1007/s10064-009-0227-9.

[24] A. G. Vondrak, M. E. Donselaar, and D. K. Munsterman. "Reservoir architecture model of the Nieuwerkerk Formation (Early Cretaceous, West Netherlands Basin): Diachronous development of sand-prone fluvial deposits". In: vol. 469. Geological Society of London, 2018, pp. 423–434. DOI: 10.1144/SP469.18.

[25] Fabian B. Wadsworth, Jérémie Vasseur, and Michael J. Heap. "An analytical form of the pore-emanating crack model in 3-D with implications for the uniaxial compressive strength of sandstone". In: *Geophysical Journal International* 241.1 (2025), pp. 495–510.

Appendix

Appendix A

Table 5: Sample Data for UCS Test.

ID	**MD [m]**	ϕ **[%]**	**GR [API]**	**Vp [m/s]**	**Vs [m/s]**	**H [mm]**	**D [mm]**	**Density [g/cm^3]**	**fix?**
Cat 1									
C7-5-PT11	2646	19.6	8.98	3073	1960	67.92	29.74	2.13	-
C6-19-PB36	2636	10.2	15.0	2634	1911	74.53	29.78	2.38	-
C6-23-PT39	2639	18.3	12.0	2109	1343	74.67	29.82	2.17	-
C7-1-PB8	2643	15.0	13.3	2230	1547	74.26	29.78	2.25	-
Cat 2									
C3-3-PT67	2597	23.3	25.0	3032	2187	74.58	29.76	2.03	-
C4-3-PT53	2597	20.1	21.1	2936	1932	74.58	29.77	2.12	-
C4-5-PT55	2601	17.7	20.6	2610	1720	56.51	29.78	2.19	-
C4-7-PT57	2603	21.2	18.6	2667	1757	74.67	29.36	2.09	-
C4-9-PB60	2606	23.3	13.2	2922	1799	60.63	29.56	2.04	-
C4-11-PB62	2608	21.6	13.1	3544	2269	74.42	29.68	2.08	-
Cat 4									
C6-3-PT19	2620	2.14	89.2	4267	2651	74.28	29.77	2.59	Gypsum
C2-5-PB74	2581	1.74	92.2	4568	2820	71.2	29.79	2.56	-
C6-5-PT21	2622	1.78	85.0	4099	2708	74.2	29.76	2.64	-
C2-9-PT77	2582	1.82	84.6	4372	2664	74.04	29.77	2.59	Gypsum
C2-11-PB80	2585	4.19	79.41	-	-	70.12	29.95	-	Gypsum

Table 6: Sample Data for triaxial test. For sedimentological description see Appendix XXX.

ID	MD [m]	ϕ [%]	GR [API]	Vp [m/s]	Vs [m/s]	Height [mm]	Diameter [mm]	Density [g/cm^3]	Notes
Cat 1									
C7-3-PB10	2645	20.5	8.83	2742	1890	74.85	29.74	2.11	-
C7-5-PB12	2647	20.4	10.2	2409	1668	74.21	29.76	2.11	-
C6-21-PB38	2638	16.1	15.2	1486	1173	66.88	29.78	2.22	Gypsum
Cat 3									
C5-3-PB44	2614	21.2	44.1	2693	1754	68.4	29.77	2.09	-
C6-17-PT33	2633	19.6	20.1	2912	2010	74.16	29.86	2.13	-
C6-15-PT31	2632	11.9	35.7	2970	2180	74.11	29.79	2.34	-
C5-1-PB42	2612	21.6	43.4	2888	1971	74.81	29.78	2.08	-
C6-13-PB30	2631	2.11	42.2	4411	3006	74.1	29.79	2.61	-
Cat 4									
C6-7-PT23	2624	1.83	89.6	3998	2575	74.51	29.76	2.59	Gypsum
C6-11-PT27	2628	1.04	83.9	4561	2747	74.57	29.77	2.61	-
C2-3-PB72	2579	2.45	87.2	2598	1666	74.3	29.52	2.58	Gypsum
C2-11-PT79	2584	2.28	83.9	3599	2195	74.86	29.74	2.57	Gypsum
C6-1-PB18	2619	1.49	92.5	4411	2802	68.83	29.77	2.63	Gypsum

Table 7: This table shows all the samples that have been tested in the Brazilian Disc Test. Sample from category 1, 2 and 3 were saturated before testing. Sample *C6-17-PB34* was not straightly cut, therefore there was a range in the thickness of that sample, the average of the thickness was taken when the tensile strength was calculated.

Sample Name	**MD [m]**	ϕ **[%]**	**GR [API]**	**Vp [m/s]**	**Vs [m/s]**	**Thickness [mm]**	**Diameter [mm]**	**Density [g/cm^3]**
Cat 4								
C6-9-PT25	2625.81	2.68	98.0	4008	2699	14.42	29.82	2.61
C1-1-PB2	2512.5	-	-	-	-	15.3	29.8	
C6-3-PT19	2620	2.14	89.2	4267	2651	13.1	29.69	2.59
Cat 3								
C2-15-PT83	2588.38	5.85	36.2	3610	2473	14.43	29.81	2.53
C2-15-PT83-2	2588.38	5.85	36.2	3610	2473	16.57	29.85	2.53
Cat 2								
C4-1-PB52-2	2598.5	13.2	34.7	3082	1956	16.89	29.79	2.33
C4-1-PB52	2598.5	13.2	34.7	3082	1956	15.0	29.85	2.33
C4-11-PT61	2607	24.4	12.8	2647	1771	15.02	29.54	2.01
Cat 1								
C7-9-PB16	2651	18.0	24.5	2993	1986	15.45	29.83	2.18
C6-19-PT35	2634.94	22.9	10.6	2800	1858	16.96	29.83	2.05
C6-17-PB34	2633.94	18.4	10.7	2947	2013	14.40–13.47	29.8	2.17

Appendix B

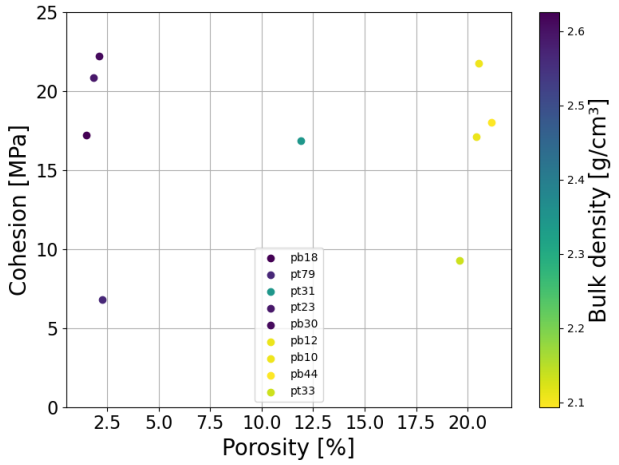

Figure 74: Cohesion plotted versus porosity colored by bulk density.

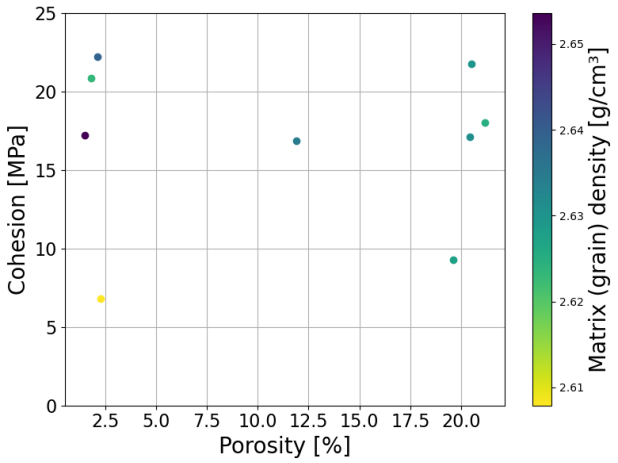

Figure 75: Cohesion plotted versus porosity colored by grain (matrix) density.

TABLE 2.1.1. Relationships among elastic constants in an isotropic material (after Birch, 1961).

K	E	λ	ν	M	μ
$\lambda + 2\mu/3$	$\mu\dfrac{3\lambda+2\mu}{\lambda+\mu}$	—	$\dfrac{\lambda}{2(\lambda+\mu)}$	$\lambda+2\mu$	—
—	$9K\dfrac{K-\lambda}{3K-\lambda}$	—	$\dfrac{\lambda}{3K-\lambda}$	$3K-2\lambda$	$3(K-\lambda)/2$
—	$\dfrac{9K\mu}{3K+\mu}$	$K-2\mu/3$	$\dfrac{3K-2\mu}{2(3K+\mu)}$	$K+4\mu/3$	—
$\dfrac{E\mu}{3(3\mu-E)}$	—	$\mu\dfrac{E-2\mu}{(3\mu-E)}$	$E/(2\mu)-1$	$\mu\dfrac{4\mu-E}{3\mu-E}$	—
—	—	$3K\dfrac{3K-E}{9K-E}$	$\dfrac{3K-E}{6K}$	$3K\dfrac{3K+E}{9K-E}$	$\dfrac{3KE}{9K-E}$
$\lambda\dfrac{1+\nu}{3\nu}$	$\lambda\dfrac{(1+\nu)(1-2\nu)}{\nu}$	—	—	$\lambda\dfrac{1-\nu}{\nu}$	$\lambda\dfrac{1-2\nu}{2\nu}$
$\mu\dfrac{2(1+\nu)}{3(1-2\nu)}$	$2\mu(1+\nu)$	$\mu\dfrac{2\nu}{1-2\nu}$	—	$\mu\dfrac{2-2\nu}{1-2\nu}$	—
—	$3K(1-2\nu)$	$3K\dfrac{\nu}{1+\nu}$	—	$3K\dfrac{1-\nu}{1+\nu}$	$3K\dfrac{1-2\nu}{2+2\nu}$
$\dfrac{E}{3(1-2\nu)}$	—	$\dfrac{E\nu}{(1+\nu)(1-2\nu)}$	—	$\dfrac{E(1-\nu)}{(1+\nu)(1-2\nu)}$	$\dfrac{E}{2+2\nu}$

Figure 76: Elastic relationships [16]

Appendix C

(a) C2-5-PB74 Before

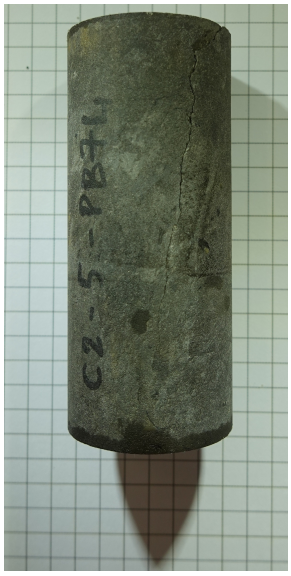

(b) C2-5-PB74 After

(c) C2-9-PT77 Before

(d) C2-9-PT77 After

(e) C2-11-PB80 Before

(f) C2-11-PB80 After

Figure 77: Samples that were tested on the UCS test, before and after.

(g) C3-3-PT67 Before

(h) C3-3-PT67 After

(i) C4-3-PT53 Before

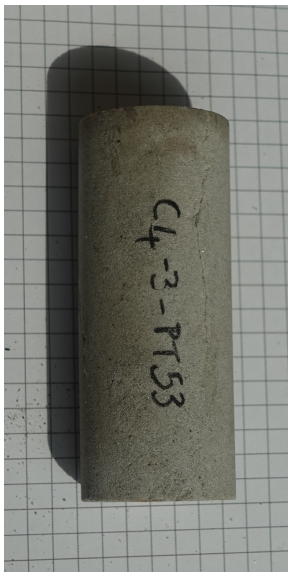

(j) C4-3-PT53 After

(k) C4-5-PT55 Before

(l) C4-5-PT55 After

(m) C4-5-PT55 After

Figure 77: Samples that were tested on the UCS test, before and after.

(n) C4-7-PT57 Before

(o) C4-7-PT57 After

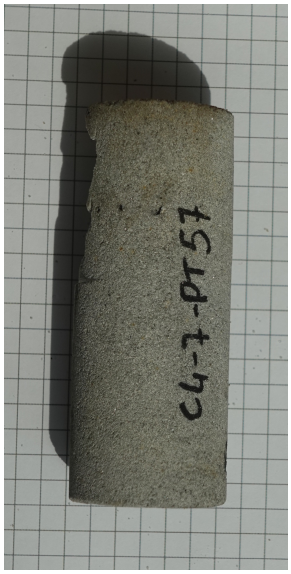

(p) C4-7-PT57 After

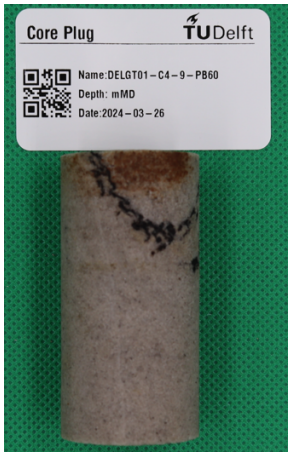

(q) C4-9-PB60 Before

(r) C4-9-PB60 After

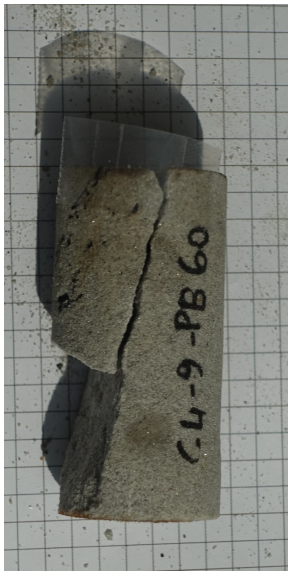

(s) C4-9-PB60 After

(t) C4-11-PB62 Before

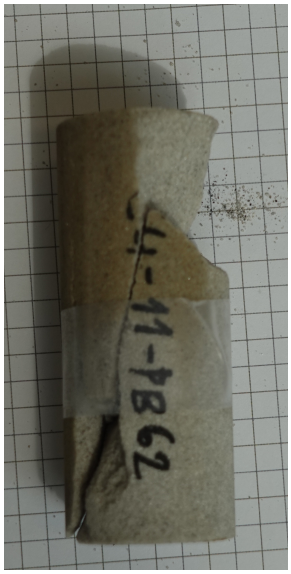

(u) C4-11-PB62 After

Figure 77: Samples that were tested on the UCS test, before and after.

(v) C6-3-PT19 Before

(w) C6-3-PT19 After

(x) C6-5-PT21 Before

(y) C6-5-PT21 After

(z) C6-19-PB36 Before

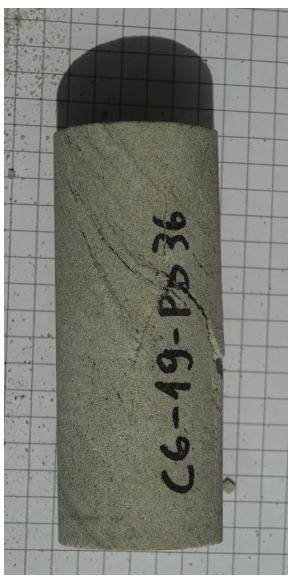

() C6-19-PB36 After

Figure 77: Samples that were tested on the UCS test, before and after.

() C6-23-PT39 Before

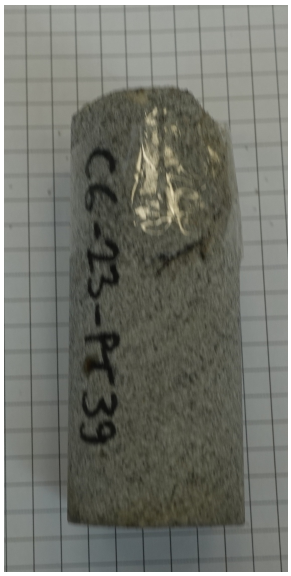

() C6-23-PT39 After

() C7-1-PB8 Before

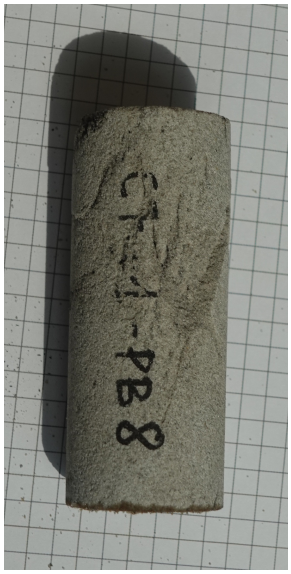

() C7-1-PB8 After

() C7-5-PT11 Before

() C7-5-PT11 After

Figure 77: Samples that were tested on the UCS test, before and after.

(a) C2-3-PB72 Before

(b) C2-3-PB72 After

(c) C2-11-PT79 Before

(d) C2-11-PT79 After

(e) C5-1-PB42 Before

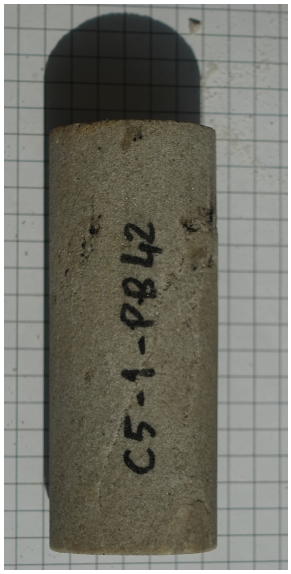

(f) C5-1-PB42 After

Figure 78: Samples that were tested on the triaxial test, before and after.

(g) C5-3-PB44 Before

(h) C5-3-PB44 After

(i) C6-1-PB18 Before

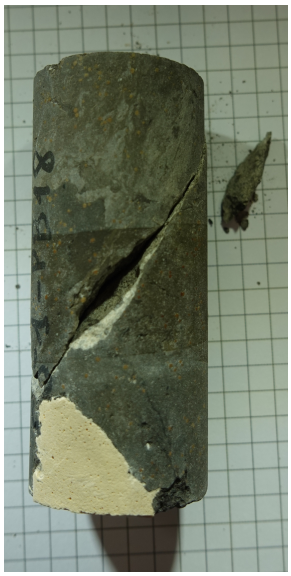

(j) C6-1-PB18 After

(k) C6-7-PT23 Before

(l) C6-7-PT23 After

Figure 78: Samples that were tested on the triaxial test, before and after.

(m) C6-11-PT27 Before

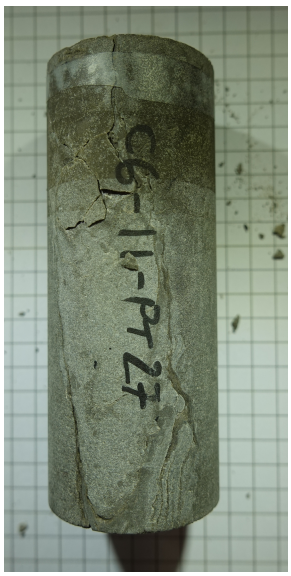

(n) C6-11-PT27 After

(o) C6-13-PB30 Before

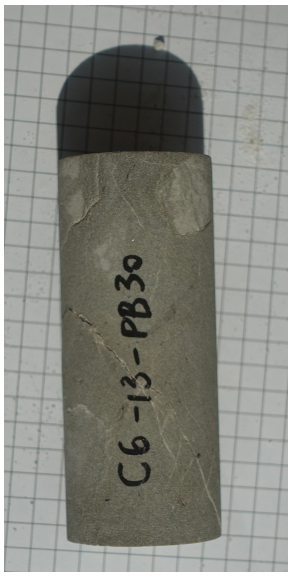

(p) C6-13-PB30 After

Figure 78: Samples that were tested on the triaxial test, before and after.

(q) C6-17-PT33 Before

(r) C6-17-PT33 Before

(s) C6-17-PT33 After

(t) C6-21-PB38 Before

(u) C6-21-PB38 After

(v) C7-3-PB10 Before

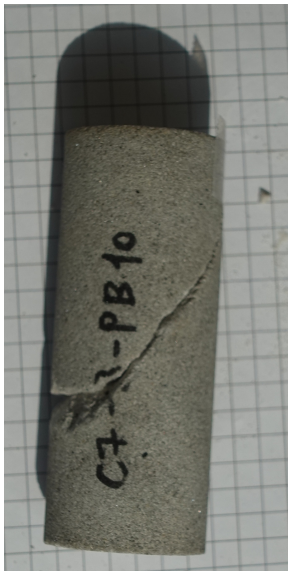

(w) C7-3-PB10 After

Figure 78: Samples that were tested on the triaxial test, before and after.

(x) C7-5-PB12 Before

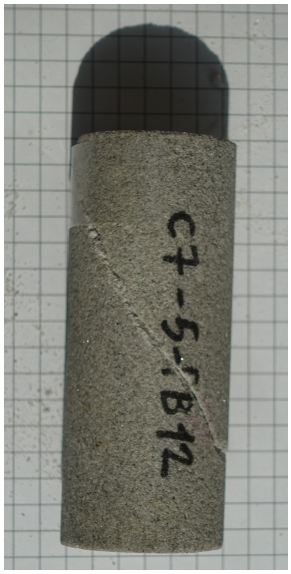

(y) C7-5-PB12 After

Figure 78: Samples that were tested on the triaxial test, before and after.

TABLE 4: *Rock material strength*

Term	Unconfined compressive strength MN/m² (MPa)	Field estimation of hardness
Very strong	>100	Very hard rock—more than one blow of geological hammer required to break specimen.
Strong	50–100	Hard rock—hand held specimen can be broken with single blow of geological hammer.
Moderately strong	12.5–50	Soft rock—5 mm indentations with sharp end of pick.
Moderately weak	5.0–12.5	Too hard to cut by hand into a triaxial specimen.
Weak	1.25–5.0	Very soft rock—material crumbles under firm blows with the sharp end of a geological pick.
Very weak rock or hard soil	0.60–1.25	Brittle or tough, may be broken in the hand with difficulty.
Very stiff	0.30–0.60*	Soil can be indented by the finger nail.
Stiff	0.15–0.30	Soil cannot be moulded in fingers.
Firm	0.08–0.15	Soil can be moulded only by strong pressure of fingers.
Soft	0.04–0.08	Soil easily moulded with fingers.
Very soft	<0.04	Soil exudes between fingers when squeezed in the hand.

* The compressive strengths for soils given above are double the unconfined shear strengths.

Figure 79: Classification of strenght of sedimentary samples by [22]